Alma Mater Studiorum
Università degli studi di Bologna

SCUOLA DI SCIENZE
Dipartimento di Fisica e Astronomia
Corso di Laurea Magistrale in Astrofisica e Cosmologia

Tesi di Laurea Magistrale

Joint temperature and polarisation analyses of the lack of power anomaly in the CMB anisotropy pattern

Presentata da:
Matteo Billi

Relatore:
Chiar.mo Prof.
Lauro Moscardini

Correlatore:
Dott. Alessandro Gruppuso
Prof. Nazzareno Mandolesi

Sessione I
Anno Accademico 2017-2018

Ai miei nonni.

Fino ai confini dell'Universo...

Abstract

La Radiazione Cosmica di Fondo (CMB) è la radiazione emessa nell'Universo primordiale dopo la ricombinazione di elettroni e protoni in idrogeno neutro. Le osservazioni della CMB negli ultimi 30 anni hanno fortemente contribuito alla nascita della cosmologia di precisione, e all'affermazione di un modello cosmologico standard, denonimato ΛCDM, i cui parametri sono stimati con un'incertezza dell'ordine del percento o addirittura inferiore. Ciò nonostante ci sono caratteristiche non ben comprese osservate alle grandi scali angolari della mappa in temperatura di CMB, note come anomalie. Una di queste, la mancanza di potenza rispetto a quanto previsto nel modello ΛCDM, potrebbe indicare l'esistenza di una nuova fase cosmologica antecedente all'epoca inflazionaria. Tale anomalia, osservata in modo consistente sia da WMAP che da Planck, non possiede però la significatività statistica necessaria per affermare l'esistenza di tale nuova fase. Al fine di studiare questa mancanza di potenza abbiamo utilizzato diversi estimatori statistici, che includono nell'analisi sia le mappe in temperatura che quelle in polarizzazione. Estimatori specifici ed innovativi, basati sullo spettro di potenza angolare della CMB, sono stati costruiti, testati e utilizzati su simulazioni e sui dati ottenuti dal satellite Planck nel 2015. Il confronto tra le simulazioni e i dati è stato valutato fornendo la percentuale di consistenza. Sono state inoltre fornite previsioni sulla sensibilità degli estimatori proposti quando impiegati su future osservazioni di CMB. Il miglioramento trovato può arrivare a un fattore dell'ordine 30, dimostrando che le misure future di polarizzazione della CMB potranno aiutare a trasformare una anomalia, attualmente osservata solo in temperatura, in una rilevazione di un nuovo fenomeno fisico.

Contents

Chapter 1

Introduction

The discovery of the Cosmic Microwave Background (CMB) by Penzias and Wilson in 1965 [40], for which they later won the Nobel Prize, provided one of the most important pieces of evidence for the Hot Big Bang model. The CMB is a source of enormous observational and theoretical interest at the present time: the CMB originated in the early stages of the Big Bang and thus it preserves imprints of various physical processes of the early Universe.

In the past 30 years continually more sophisticated experimental techniques have been directed at the measurement of the CMB, exploiting ground-based antennae, rockets, balloons and satellites. Finally in 14 May 2009 it was launched Planck satellite (ESA) [2, 1]. The design of Planck allows it to image the whole sky twice per year, with a combination of sensitivity, angular resolution, and frequency coverage never achieved before. Fig 3.1 shows the CMB intensity map observed by Planck [1].

The CMB radiation possesses a near-perfect black-body spectrum, which is an evidence that the Big Bang model is correct: its near-perfect black-body spectrum means that when the CMB was produced matter and radiation were in thermal equilibrium. According to the standard cosmology, after the recombination of electrons and protons into neutral hydrogen, the Universe becomes transparent for CMB photons and they move along geodesics of the perturbed Friedman geometry. This corresponds to the so-called surface of last-scattering at a redshift of about $z_{ls} \simeq 1100$, when the Universe had an age of about $380000 yr$. From the epoch of last-scattering onwards, photons free-stream and reach us basically untouched. Detecting primordial photons is therefore equivalent to take a picture of the early Universe when the CMB photons was generated. A fundamental characteristic of the CMB are the fluctuations of the temperature observed in its pattern. These anisotropies are smaller than about one part in 10^5 and are usually expressed in terms of

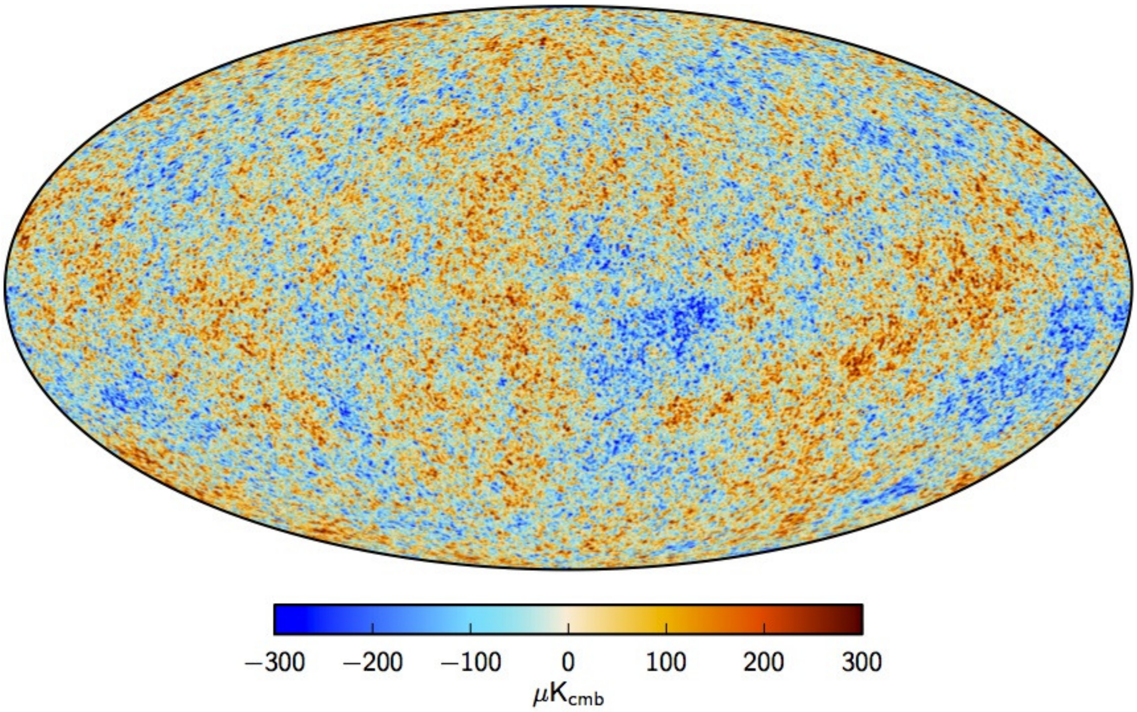

Figure 1.1: CMB maximum posterior intensity map obtained by Planck at 50 resolution derived from the joint baseline analysis of Planck, WMAP, and 408 MHz observations. A small strip of the Galactic plane, covering 1.6% of the sky, is filled in by a constrained realization that has the same statistical properties as the rest of the sky [1].

the quantity:

$$\frac{\Delta T(\theta,\varphi)}{T_0} = \frac{T(\theta,\varphi) - T_0}{T_0} \simeq 10^{-5} \tag{1.1}$$

which gives the temperature fluctuation as a fraction of the mean temperature T_0 and as a function of angular position on the sky (θ, φ). The primary anisotropies are believed to have been generated from quantum fluctuations in the very early Universe by a scale-invariant mechanism. The most prominent context is cosmological inflation. If inflation lasts long enough, the spatial geometry of the Universe is generally predicted to be indistinguishable from Euclidean, and the topology of the observable Universe is expected to be trivial (simply connected). The COBE [44, 45] discovery revealed the long-expected temperature anisotropies and confirmed that they are consistent with an almost scale-invariant power spectrum of temperature fluctuations.

The CMB observations have greatly contributed to build the ΛCDM cosmological model. However several unexpected features have been observed in the CMB anisotropy temperature maps at large angular scales, both by WMAP and by Planck. The lack of power anomaly is one of these features [43] and consists in a missing of power, at these scales, with respect to what foreseen by the cosmological ΛCDM model. This effect has been studied with the variance estimator in WMAP data [35, 18, 27] and in Planck 2013 [4] and 2015 [6] data, measuring a lower-tail-probability (henceforth LTP[1]) at the level of per cent. An early fast-roll phase of the inflaton could naturally explain such missing power: therefore this anomaly might witness a new cosmological phase before the standard inflationary era (see e.g. [24, 28, 25] and references therein). However, with only the observations based on the temperature map, this anomaly has not the statistical significance needed to be considered the imprint of new physics beyond the standard cosmological model and is conservatively interpreted as a simple statistical fluke of the ΛCDM.

The main goal of this thesis is to look for new estimators able to consider also the counterpart in polarisation of the lack of power anomaly in order to increase its significance and potentially raise this anomaly up to the level of a possible manifestation of new physics beyond the standard model.

To perform this task, I follow a frequentist approach and take into account several statistical estimators which I have implemented in the Python language. Once validated, these estimators have been applied on public Planck 2015 low-ℓ data and on realistic Monte Carlo simulations extracted from ΛCDM [10, 32, 22, 23]. As usual, the comparison between simulations and Planck data is expressed in terms of percentage of consistency.

---

[1] The LTP is the probability to obtain a value as low as the data.

Specifically, I proposed and applied two new estimators. The first one is a two-dimensional estimator based on the variance estimators defined as:

$$
\begin{aligned}
var^{TT} &= C_2^{TT}(0) = \sum_{\ell=2}^{\ell_{max}} \frac{2\ell+1}{4\pi} C_\ell^{TT}, &(1.2)\\
var^{QQ} &= C_2^{QQ}(0) = \sum_{\ell=2}^{\ell_{max}} \left[\frac{2\ell+1}{8\pi}(C_\ell^{EE}+C_\ell^{BB})\right], &(1.3)
\end{aligned}
$$

where ℓ_{max} is the highest multipole considered in the sum and C_ℓ^{TT}, C_ℓ^{EE} and C_ℓ^{BB} being the observed and simulated CMB angular power spectra. These variances are then used to build a 2D-variance which are shown in a 2D-contour plot that allows to evaluate the C.L. for the Planck data and to make forecasts for future observations.

The second estimator, which is the main element of novelty of my thesis, is a 1D-estimator:

$$P = \frac{1}{(\ell_{max}-1)} \sum_{\ell=2}^{\ell_{max}} \left(x_\ell^1 + x_\ell^2\right), \tag{1.4}$$

which could be interpreted as a dimensionless normalised mean power and jointly contains all the information present in the TT, EE and TE spectra. The objects x_ℓ^1 and x_ℓ^2, that we call Angular Power Spectrum (henceforth APS) of Random Variables, are obtained inverting the algebra typically used to simulate the temperature and E-mode polarisation CMB maps and physically are dimensionless normalised angular power spectra:

$$
\begin{aligned}
x_\ell^1 &= \frac{C_\ell^{TT}}{C_\ell^{TT,th}}, &(1.5)\\
x_\ell^2 &= \frac{C_\ell^{EE}}{a_\ell^2} C_\ell^{TT,th} - \frac{C_\ell^{TT,th}}{a_\ell^2}\left(\frac{C_\ell^{TE,th}}{C_\ell^{TT,th}}\right)^2 C_\ell^{TT} \\
&\quad -2\frac{C_\ell^{TE,th}}{a_\ell^2}\left[C_\ell^{TE} - \frac{C_\ell^{TE,th}}{C_\ell^{TT,th}} C_\ell^{TT}\right], &(1.6)
\end{aligned}
$$

where $a_\ell = \sqrt{C_\ell^{EE,th} C_\ell^{TT,th} - (C_\ell^{TE,th})^2}$ and C_ℓ^{th} being the theoretical angular power spectra. As one can see, between the APS of Random Variables and the angular power spectra C_ℓ^{TT}, C_ℓ^{EE} and C_ℓ^{TE} there is a complicated mapping. The advantage of using APS of Random Variables is that they are dimensionless and homogeneous numbers and can be easily combined to define a 1-D estimator which depends on temperature, E-mode polarisation and their cross-correlation.

The outcome of this analysis seems to confirm that the polarisation data increase the statistical significance of the considered effect: LTP decreases by a factor of ~ 6, for both the estimators.

I provide also forecasts that show how future cosmic variance limited observations at the largest angular scales both in temperature and polarisation could improve the detection level with respect to current situation. It turns out that the P estimator can be improved by a factor of 30 while the 2D-variance estimator can gain only a factor of 2.6. Therefore the new estimator P is particularly sensitive to future improvements: the inclusion of the large-scale E-mode polarisation can potentially help in transforming an anomaly in a detection of a new physical phenomenon.

The thesis is organised as follows: in Chapter 2 we provide an introduction about the Hot Big-Bang model and the Inflationary Universe; in Chapter 3 is devoted to the description of the CMB; in chapter 4 we introduce a new approach to the study of the CMB power pattern based on the APS of Random Variables, in Chapter 5 we describe the used data and the employed simulations; in Chapter 6 we report the result on Planck data whereas in Chapter 7 we estimate the improvement expected from future CMB polarised observations; conclusions are drawn in Chapter 8.

Chapter 2

Standard Cosmology

2.1 Standard Cosmological Model

The evolution of our Universe is described by the Hot Big Bang model [14, 36]. This model is based on the so-called Cosmological Principle: the Universe is, on large scales, homogeneous and isotropic. The best evidence for the isotropy is the uniformity of the temperature of the Cosmic Microwave Background (CMB) radiation: intrinsic temperature anisotropies are smaller than 10^{-5}. Other recently probes confirm that at scale larger than ($\sim 60h^{-1}$ Mpc) the Universe is well compatible with the cosmological principle [38].

The most generic metric that satisfies the condition of homogeneity and isotropy on large scales is the Friedmann-Lemaitre-Robertson-Walker (FLRW) metric:

$$\begin{aligned} ds^2 &= \sum_{\mu,\nu=0}^{3} g_{\mu\nu} dx^\mu dx^\nu \\ &= c^2 dt^2 - a^2(t) \left[\frac{dr^2}{1-kr^2} + r^2 d\theta^2 + r^2 \sin^2\theta d\phi^2 \right], \end{aligned} \tag{2.1}$$

where $g_{\mu\nu}$ is the metric tensor, (t, r, θ, ϕ) are coomoving coordinates, $a(t)$ is the cosmic scale factor and k can be chosen to be $+1$, -1, or 0 for respectively closed, open or flat spaces. The coordinate r is taken to be dimensionless and $a(t)$ has dimensions of length. The time coordinate is the proper time measured by an observer at rest in the comoving frame, i.e. $(r, \theta, \phi) = constant$. Instead of the cosmic time it is customary to use the redshift z which is the shift of spectral lines to longer wavelengths caused by the recession of Galaxies from our Galaxy in the uniform expansion of the Universe. The redshift is defined to be:

$$z \equiv \frac{\lambda_0 - \lambda_e}{\lambda_e}, \tag{2.2}$$

where λ_e is the wavelengths of the line as emitted and λ_0 the observed wavelength. It follows directly from the FLRW metric that the redshift z is directly related to the scalar factor $a(t)$ through the relation:

$$1 + z = \frac{a_0}{a(t)}, \tag{2.3}$$

where a_0 is the scale factor at the present-day. The redshift determines the scale factor $a(t)$ (or the cosmic time once the function $a(t)$ is known) of the Universe when the light was emitted from distance sources.

2.1.1 Friedmann Equations

The FLRW models are relativistic models, based on the solutions of the field equations of Einstein General Relativity[51]:

$$R_{\mu\nu} - \frac{1}{2} g_{\mu\nu} R = \frac{8\pi G}{c^4} T_{\mu\nu} - \Lambda g_{\mu\nu}, \tag{2.4}$$

where $R_{\mu\nu}$ is the Ricci tensor, R is the Ricci scalar, $T_{\mu\nu}$ is the stress-energy tensor for all the fields present in the Universe, G is the Newtonian constant of gravitation and c is the speed of light. We have included the presence of a cosmological constant Λ. In standard cosmology $T_{\mu\nu}$ is taken to be the energy-momentum tensor of a perfect fluid:

$$T_{\mu\nu} = -P g_{\mu\nu} + \left(P + \rho c^2\right) u_\mu u_\nu, \tag{2.5}$$

where P and ρ are respectively the pressure and the density of the fluid and the four-vector u_μ is the velocity field of the fluid. To solve the Einstein equations it is necessary to introduce a relationship between the pressure and the density of the cosmic fluid which, in the standard models, is liner and parameterised through the parameter w:

$$P = w \rho c^2. \tag{2.6}$$

In general for physical matter one requires $\rho > 0$, i.e. positive energy, and also $P > 0$, implying that $w > 0$. In particular, for non-relativistic particles (m), usually called dust, there is negligible pressure:

$$w_m = 0, \quad P_m = 0. \tag{2.7}$$

Relativistic particles (r), e.g. radiation, have the following equation of state:

$$w_r = \frac{1}{3}, \quad P_r = \frac{1}{3} \rho c^2. \tag{2.8}$$

A cosmological constant, instead, corresponds to a contribution with:

$$w_\Lambda = -1, \quad P_\Lambda = -\rho c^2. \tag{2.9}$$

In standard cosmology it is assumed that the expansion of the Universe is adiabatic[1]:

$$d(\rho c^2 a^3) = -P da^3. \tag{2.10}$$

From this equation we can obtain the relation:

$$\rho_w a^{3(1+w)} = \rho_{0,w} a_0^{3(1+w)} = const \tag{2.11}$$

where $\rho_{0,w}$ is the density at the present time. Under this assumption the matter, radiation and cosmological constant have different behaviour with the redshift:

$$\rho_m = \rho_{0,m} \left(\frac{a_0}{a}\right)^3 = \rho_{0,m} \left(1+z\right)^3, \tag{2.12}$$

$$\rho_r = \rho_{0,r} \left(\frac{a_0}{a}\right)^4 = \rho_{0,r} \left(1+z\right)^4, \tag{2.13}$$

$$\rho_\Lambda = \rho_{0,\Lambda}, \tag{2.14}$$

and contribute differently during the evolution of the Universe. The early Universe was radiation dominated, the "adolescent" Universe was matter dominated and the present-day Universe is dominated by the cosmological constant Fig. 2.1.

Because the isotropy and homogeneity only the 00-component and any one of the non-zero ij- components of the Einstein field equations survive. From these two equations we obtain the so-called I and the II Friedmann equations:

$$\ddot{a} = -\frac{4\pi G}{3}\left(\rho + \frac{3P}{c^2}\right) a + \frac{\Lambda c^2}{3} a, \tag{2.15}$$

$$\dot{a}^2 + kc^2 = \frac{8\pi G}{3}\rho a^2 + \frac{\Lambda c^2}{3} a^2; \tag{2.16}$$

given the equation of state $P = P(\rho)$, the equations (2.15, 2.16) can be solved for $a(t)$, which describes the evolution of the Universe.

The Friedmann equations can be recast in terms of the Hubble parameter $H(t)$ and the critical density parameter Ω:

$$H(t) \equiv \frac{\dot{a}}{a}; \tag{2.17}$$

---

[1] The adiabatic expansion is a consequence of the equation of continuity, condition satisfied by the Einstein field equations with a perfect fluid as source.

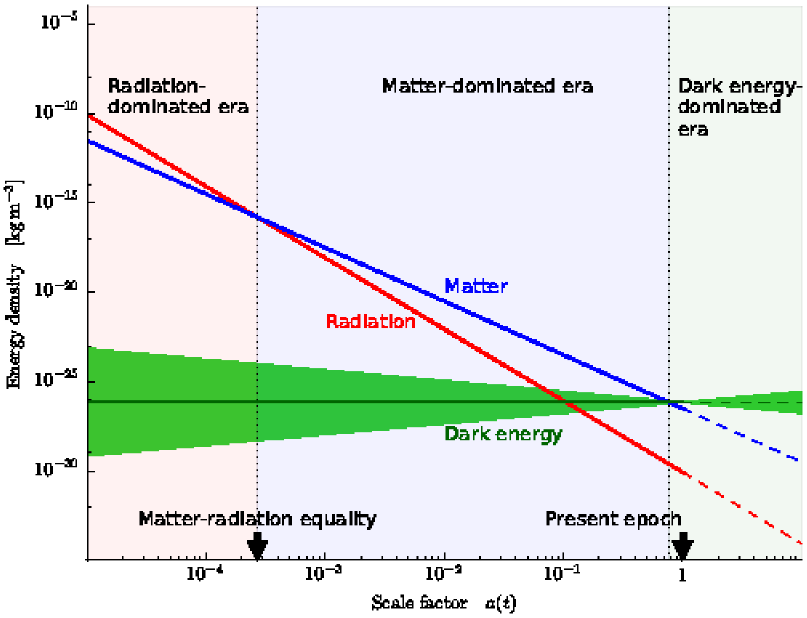

Figure 2.1: The density evolution of the main components of the Universe: the early Universe was radiation dominated, the “adolescent” universe was matter dominated and the present day Universe is dominated by the cosmological constant. Debono et al; General Relativity and Cosmology: Unsolved Questions and Future Directions.

$$\Omega \equiv \frac{\rho}{\rho_c}, \quad \rho_c \equiv \frac{3H^2}{8\pi G}. \tag{2.18}$$

The Hubble parameter is not a constant and at the present time it is called the Hubble constant:

$$H_0 = \frac{\dot{a}_0}{a_0}. \tag{2.19}$$

The geometry of the Universe can be expressed in terms of Ω, or $\Omega_k \equiv 1 - \Omega$:

- $\Omega > 1 \quad \rightarrow \quad \Omega_k > 0$: Closed Universe;
- $\Omega = 1 \quad \rightarrow \quad \Omega_k = 0$: Flat Universe;
- $\Omega < 1 \quad \rightarrow \quad \Omega_k < 0$: Open Universe.

For a multi-components fluid model Universe we have:

$$\Omega = \sum \Omega_i. \tag{2.20}$$

The II equation of Friedmann becomes:

$$H^2(t) = H_0^2 \left(\frac{a_0}{a}\right)^2 \left[1 - \sum_i \Omega_{0,i} + \sum_i \Omega_{0,i} \left(\frac{a_0}{a}\right)^{1+3\omega_i}\right]; \tag{2.21}$$

or in function of the redshift:

$$\begin{aligned} H^2(t) &= H_0^2 \left(1+z\right)^2 \left[1 - \sum_i \Omega_{0,i} + \sum_i \Omega_{0,i} \left(1+z\right)^{1+3\omega_i}\right] = \\ &= H_0^2 E^2(z). \end{aligned} \tag{2.22}$$

For the Universe at the present time the component of radiation is negligible so we can consider a Universe composed only by the components of matter and cosmological constant. The evolution of the Hubble parameter is described by:

$$H^2(z) = H_0^2 \left[\Omega_{0,m}(1+z)^3 + \Omega_{0,k}(1+z)^2 + \Omega_{0,\Lambda}\right], \tag{2.23}$$

Through independent observations, measures of luminosity distance by means SNIa, survey of Cluster of Galaxies and CMB, see Fig. 2.2, have been deduced the constraints for the cosmological parameters $\Omega_{0,m}$ and $\Omega_{0,\Lambda}$. Table 2.1 reports the values of $\Omega_{0,m}$ and $\Omega_{0,k}$ as measured by Planck and by the observations of SNIa (Supernovae Cosmology Project SCP 2011). So the Universe at the present time is compatible with a flat geometry and is composed by matter for about 30% and by dark energy for about 70%.

The Hot Big Bang Model presents some shortcomings, as the Horizon and the flatness problem that can be solve through the Inflationary Paradigm.

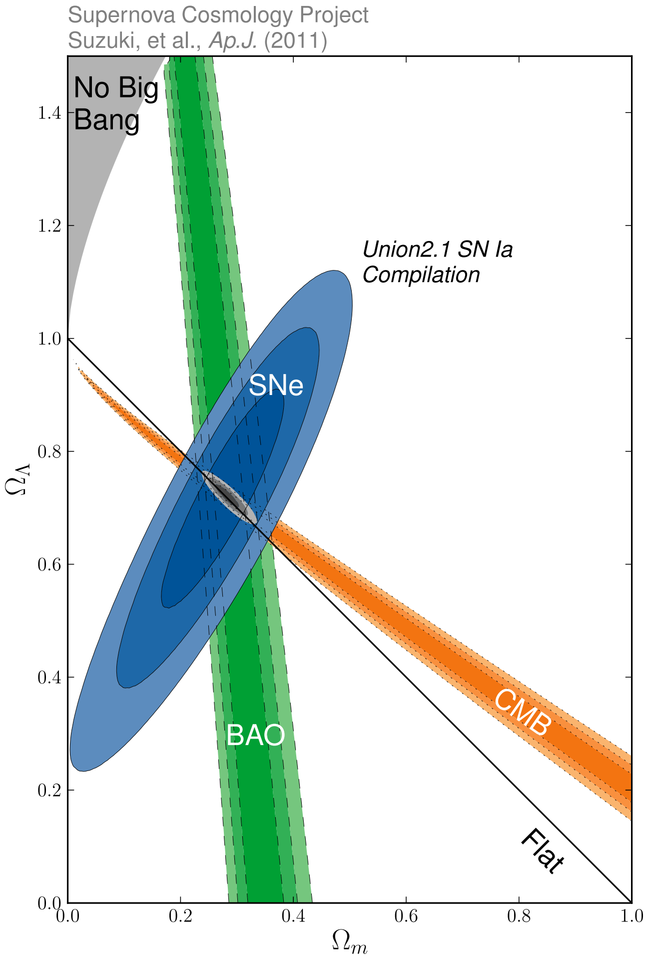

Figure 2.2: Confidence levels for the cosmological parameters, obtained from observations of SNIa (blue), CMB (orange) and BAO (green). Suzuki et al. 2011.

	$\Omega_{0,m}$	$\Omega_{0,k}$
Planck Mission	$0.3121^{+0.0087}_{-0.0087}$	$0.040^{+0.038}_{-0.041}$
SCP 2011	$0.282^{+0.015}_{-0.014}$	$-0.004^{+0.006}_{-0.006}$

Table 2.1: Cosmological parameters as measured by Planck and by the observations of SNIa

2.2 Inflationary Paradigm

The inflationary paradigm is based upon the idea that during an early era, so-called Inflation, before the era of primordial nucleosynthesis, the expansion of the Universe was accelerated. In this epoch the vacuum energy of a scalar quantum field, called the Inflaton Φ, dominates over other forms of energy, hence giving rise to a quasi-exponential expansion. This phase of rapid acceleration of the Universe can solve the flatness, the horizon and the monopole problems of the Hot Big Bang model. For more details, see e.g. [11, 41] and references therein.

2.2.1 Inflationary solution at the horizon and at the flatness problems

The Horizon Problem is a problem of causality. The Universe appears extremely smooth over very large distance scales, even though, according to the Hot Big Bang model, such distant regions had not been able to establish mutual correlation by exchanging any causal signal. A direct proof of this problem comes from the observations of the CMB maps: the surface of the last scattering, which is much larger than the Hubble radius ($r_H(t) = c/H(t)$) at the time of last scattering, is homogeneous and isotropic. To explain the Inflationary solution to this problem we introduce the comoving Hubble radius:

$$\tilde{r}_H(t) = \frac{c}{\dot{a}}, \tag{2.24}$$

which sets the effective comoving scale of causal connection. In a Universe dominated by a perfect fluid with $w > -1/3$, $\tilde{r}_H(t)$ grows with time, therefore larger and larger scales get in causal connection with increasing time as soon as they enter the horizon, i.e. cross the Hubble radius. According to the inflationary paradigm, in the early Universe $\tilde{r}_H(t)$ had decreased for some time, thus those scales which enters the horizon now may have actually been in causal contact in the past. A decrease of the Hubble radius with time:

$$\dot{\tilde{r}}_H(t) < 0, \tag{2.25}$$

corresponds to a:

$$\ddot{a} > 0 \tag{2.26}$$

i.e. an acceleration. This is the main characteristic which defines the inflationary paradigm.

Another shortcoming of the Hot Big Bang Model is the so-called flatness problem, that is a fine-tuning problem. In order to get the observed value at the present time of $(\Omega_0 - 1) \sim 0$, the value of $(\Omega - 1)$ at the early Universe has to be fine-tuned to values amazingly close to zero ($\sim 10^{-64}$). The solution of the horizon problem also solves the flatness one. Since $\tilde{r}_H$ decreases because of the accelerated expansion, at the end of the Inflation, $|\Omega - 1|$ gains such a tiny value that it can easily accommodate for the present observation of an almost flat Universe.

2.2.2 Slow-Roll dynamics of the Inflaton field

The standard model of Inflation is the so-called slow-roll scenario, associated to a single scalar field. During the Inflation one can consider a homogeneous and isotropic Universe described by the FLRW metric (see eq. 2.1). One takes the Universe dominated by the vacuum energy of a scalar field, therefore the Friedmann equations become (in this section we use units such that $c = h = k_B = G = 1$):

$$\ddot{a} = -\frac{4\pi G}{3}\left(\rho + 3P\right)a, \tag{2.27}$$

$$\dot{a}^2 + k = \frac{8\pi G}{3}\rho a^2; \tag{2.28}$$

where ρ and P are the density and pressure of the scalar field. The equation (2.27) implies that a period of accelerated expansion, $\ddot{a} > 0$, takes place only if:

$$P < -\frac{1}{3}\rho. \tag{2.29}$$

The condition (2.29) can be satisfied by a homogeneous scalar field, the inflaton Φ, which behaves like a perfect fluid with energy density and pressure given by:

$$P_\Phi = \frac{\dot{\Phi}^2}{2} - V(\Phi), \tag{2.30}$$

$$\rho_\Phi = \frac{\dot{\Phi}^2}{2} + V(\Phi), \tag{2.31}$$

where $V(\Phi)$ specifies the scalar field potential. Hence if we require the so-called slow-roll condition:

$$V(\Phi) >> \dot{\Phi}^2, \tag{2.32}$$

we obtain:

$$P_\Phi \simeq -\rho_\Phi. \tag{2.33}$$

Thus, we realize that a scalar field whose energy is dominant in the Universe and whose potential energy dominates over the kinetic term gives inflation. The equation of motion of the scalar field Φ is:

$$\ddot{\Phi} + 3H\dot{\Phi} + \frac{dV(\Phi)}{d\Phi} = 0, \tag{2.34}$$

where $3H\dot{\Phi}$ is the friction term of a scalar field rolling down its potential due to the expansion of the Universe. The condition (2.32) requires the scalar field slowly rolls down its potential. Such a slow-roll period can be achieved if the inflaton field Φ is in a region where the potential is sufficiently flat. The flatness condition of the potential could be parametrized in terms of the so-called slow-roll parameters:

$$\epsilon \equiv \frac{1}{16\pi}\left(\frac{V'}{V}\right)^2, \tag{2.35}$$

$$\eta \equiv \frac{1}{8\pi}\left(\frac{V''}{V}\right). \tag{2.36}$$

Achieving a successful period of inflation requires the slow-roll parameters to be $\epsilon, |\eta| << 1$; when this condition fails, inflation ends.

It has been proposed a really large number of inflationary models, differing for the underlying particle physics theory and for the kind of potential. These models could be classified into three broad groups as “small field”, “large field” and “hybrid” type, according to the region occupied in the space $(\epsilon - \eta)$ by a given inflationary potential. The Planck dataset allows to extract the parameters necessary for distinguishing among single-field inflation models [9].

The period of accelerated expansion of the Universe must last enough to solve the horizon and flatness problems. It is customary to measure the duration of inflation in terms of the number of e-foldings, defined as:

$$N = ln\left(\frac{a_f}{a_i}\right), \tag{2.37}$$

where a_f and a_i are respectively the scale factors at the beginning and at the end of the inflation. It is requested that:

$$N >> N_{min}, \tag{2.38}$$

where $N_{min} \sim 60$ is the number of e-foldings before the end of inflation when the present Hubble radius leaves the horizon. When the Inflaton field starts to roll fast along its potential, Inflation ends. When inflation ends, the inflaton Φ oscillates about the minimum of its potential $V(\Phi)$ and decays, thereby reheating the Universe. After this phase the Universe is repopulated by a hot radiation fluid.

2.2.3 Inflation and cosmological perturbations

The Inflation can generate the primordial fluctuations. According to the inflationary paradigm, primordial density and gravitational-waves perturbations were generated from quantum fluctuations redshifted out of the Hubble radius, were they remain “frozen”: quantum vacuum oscillations of the Inflaton give rise to classical fluctuations in the energy density, which provide the seeds for Cosmic Microwave Background (CMB) radiation temperature anisotropies and polarisation, as well as for the formation of Large Scale Structures (LSS) in the present Universe.

The generation of gravity-wave fluctuations is a generic prediction of an accelerated de Sitter expansion of the Universe whatever mechanism for the generation of cosmological perturbations is operative. Gravitational waves, whose possible observation might come from the detection of the B-mode of polarization in the CMB anisotropy (which are explained in chapter 3) may be viewed as ripples of space-time around the background metric.

Chapter 3

Cosmic Microwave Background

3.1 Introduction to CMB

The Cosmic Microwave Background (CMB), discovered by Penzias and Wilson in 1965 [40], provides one of the most important pieces of evidence for the Hot Big Bang model. Penzias and Wilson, which were radio engineers, investigating the properties of atmospheric noise in connection with the Telstar communication satellite project, found an apparently uniform background signal at microwave frequencies which could not be explained by instrumental noise or by any known radio sources. They admitted the possibility that they had discovered a thermal radiation background left as a relic of the primordial fireball phase. A group of theorists at Princeton University, including Dicke and Peebles, soon gave the interpretation of the background "hiss" as relic radiation [19].

The CMB is a source of enormous observational and theoretical interest: the CMB actually did originate in the early stages of a Big Bang, thus it conserves the imprints of various physical early Universe processes.

In the past 30 years continually more sophisticated experimental techniques have been directed at the measurement of the CMB, using ground-based antennae, rockets, balloons and satellites. The first satellite was COBE (USA) [44, 45], launched in the 1989. It had an enormous advantage over previous experiments: it was able to avoid atmospheric absorption, which is an important systematic effect for ground-based experiments at microwave and submillimetric frequencies. The CMB spectrum observed by COBE reveals just how close to an ideal black body the radiation background is, with a mean the temperature of $2.726 \pm 0.005 K$ [45]. In the 2001 was launched the satellite WMAP (USA) [12] which had a resolution really better than COBE. Finally 14 May 2009 it was launched Planck satellite (ESA) [2, 1] which had a combination of sensitivity, angular resolution, and frequency coverage never before achieved. Planck carried an array of 74 detectors sensitive to a range of frequencies between $\sim$25 and $\sim$1000 GHz, which scanned the sky simultaneously and continuously with an angular resolution varying between$\sim$5’ at the highest frequencies and $\sim$30 arcminutes at the lowest. The array was arranged into two instruments: the Low Frequency Instrument (LFI), which covered three bands (centred at 30, 44, and 70 GHz) and the High Frequency Instrument (HFI) which covered six bands (centred at 100, 143, 217, 353, 545 and 857 GHz). Fig 3.1 shows the CMB intensity map observed by Planck [1].

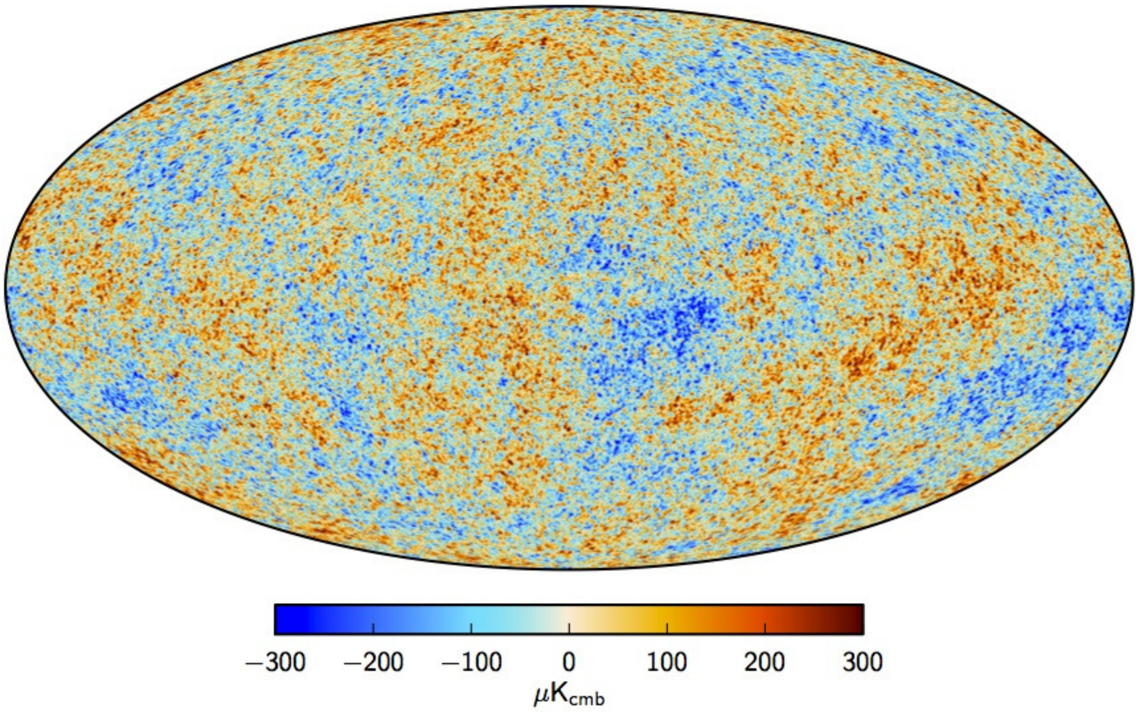

Figure 3.1: CMB maximum posterior intensity map by Planck at 50 resolution derived from the joint baseline analysis of Planck, WMAP, and 408 MHz observations. A small strip of the Galactic plane, covering 1.6% of the sky, is filled in by a constrained realization that has the same statistical properties as the rest of the sky [1].

3.2 CMB Black Body Spectrum

The CMB radiation possesses a near-perfect black-body spectrum, which is a good evidence that the Big Bang model is correct: its near-perfect black-body spectrum means that when the CMB was produced matter and radiation were at the thermal equilibrium. According to the standard cosmology, after recombination of electrons and protons into neutral hydrogen, the Universe becomes transparent for CMB photons and they move along geodesics of the perturbed Friedman geometry. This corresponds to the so-called surface of last-scattering at a redshift of about $z_{ls} \simeq 1100$ and an age of about $380000yr$. From the epoch of last-scattering onwards, photons free-stream and reach us basically untouched. Detecting primordial photons is therefore equivalent to take a picture of the early Universe when the CMB photons was generated. Assuming thermal equilibrium, the intensity of the radiation is given by a black-body spectrum:

$$I(T_i, \nu) = \frac{4\pi\hbar\nu^3}{c} \left[e^{\left(\frac{h\nu}{k_B T_i}\right)} - 1 \right]^{-1}, \tag{3.1}$$

where $\hbar$ is the Planck constant, ν is the radiation frequency, c is the speed of light, k_B is the Boltzmann constant and T_i is the temperature of the radiation. During the expansion of the Universe the form of the spectrum $I(T, \nu)$ remains the same (because both T and ν have the same dependence on the redshift) with the replacement of T_i by:

$$T = T_i \frac{a(t_i)}{a(t)}. \tag{3.2}$$

Fig. 3.2 shows the results obtained by The FIRAS instrument on the COBE satellite [34], together with results in different wavelength regions obtained from other experiments. The quality of the fit of the observed CMB spectrum to a black-body curve provides clear evidence of the Big Bang scenario.

The black-body spectrum of the CMB has the peak at the wavelength $\lambda = 0.2\ mm$, which corresponds at the temperature of [1]:

$$T_{0,CMB} = 2.726 \pm 0.005 K. \tag{3.3}$$

The observation of an isotropic CMB provides strong support for the cosmological principle , which states that the Universe is statistically isotropic and homogeneous at large scales.

---

[1] For a black-body spectrum the wavelength of the peak and the temperature of the radiation are connected by the law: $\lambda_{peak} \cdot T = b$, with $b = 2,8977685 \cdot 10^{-3} m \cdot K$.

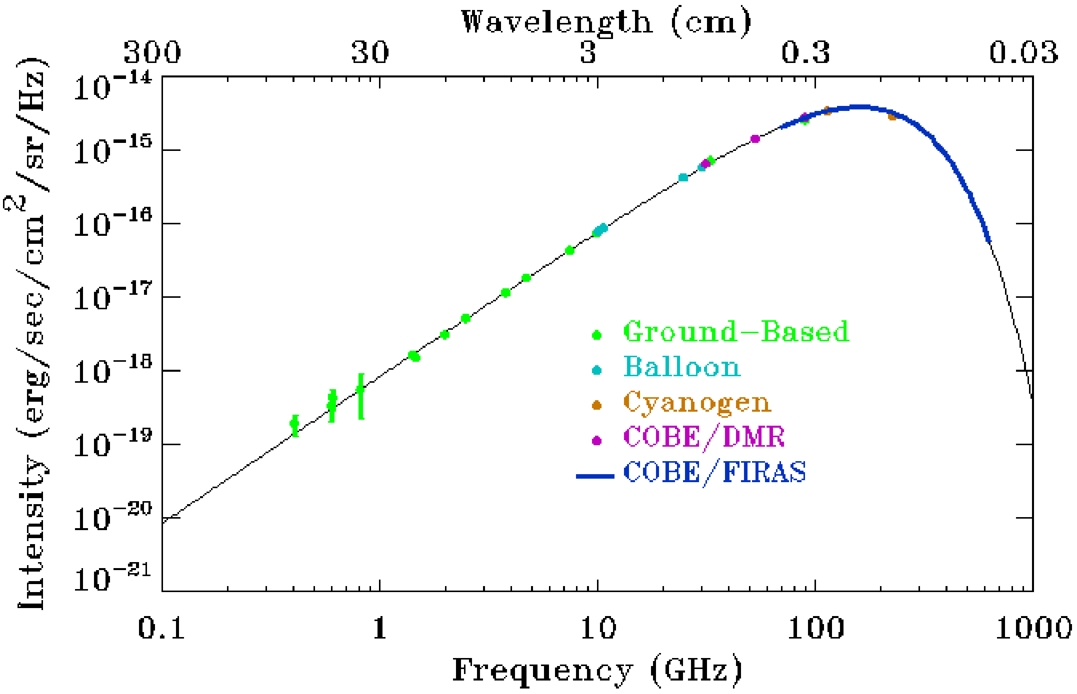

Figure 3.2: CMB spectrum as measured by the FIRAS instrument aboard COBE satellite. FIRAS determined the CMB temperature to be 2.726 ± 0.005 K, with deviations from a perfect blackbody limited to less than $5 \cdot 10^{-5}$ in intensity[34].

3.3 CMB Anisotropies

A fundamental characteristic of the CMB are the fluctuations of the temperature observed in its pattern. These anisotropies are smaller than about one part in 10^5 and are usually expressed in terms of the quantity:

$$\frac{\Delta T(\theta,\varphi)}{T_0} = \frac{T(\theta,\varphi) - T_0}{T_0} \simeq 10^{-5} \tag{3.4}$$

which gives the temperature fluctuation as a fraction of the mean temperature T_0 and as a function of angular position (θ, φ) on the sky. Since CMB anisotropies are small, they can be treated within linear cosmological perturbation theory, which allows to split them into scalar, vector and tensor contributions according to their transformation properties under rotation. Scalar and tensor perturbations contribute to CMB anisotropies whereas the initial vector perturbations rapidly decay.

These anisotropies are classified in two main categories: primary and secondary. The first ones are all those anisotropies produced at the redshift of the last-scattering (z_{LS}) and the second ones are the fluctuations generates by the interactions that the CMB made in the space-time path from z_{LS} and z_0 ($z_0 \equiv 0$).

The primary anisotropies are believed to have been produced during the Inflation by a nearly scale-invariant mechanism. The inflationary theory predicts that the CMB temperature fluctuations should be:

- statistically isotropic,
- Gaussian,
- almost scale invariant,
- phase coherence of the fluctuations,
- dominance of the so-called adiabatic mode,
- the non-existence of rotational modes at large scales,
- a detectable stochastic background of gravitational waves.

The CMB anisotropies are functions on a sphere, therefore we can express them in terms of the spherical harmonic expansion [36]: [2]

$$\frac{\Delta T}{T}(\theta,\varphi) = \sum_{\ell=0}^{\infty}\sum_{m=-\ell}^{m=+\ell} a_{\ell m} Y_{\ell m}(\theta,\varphi) \tag{3.5}$$

where $a_{\ell m}$ are the coefficients of the spherical harmonic $Y_{\ell m}$ and the index ℓ is the multipole which corresponds to the inverse of the angular distance between two point on the sky ϕ, according to the approximate relation:

$$\ell \simeq \frac{180^\circ}{\phi}. \tag{3.6}$$

From a given CMB map one can extract the harmonic coefficients $a_{\ell m}$. For statistically isotropic fluctuations the harmonic coefficients are orthogonal, therefore:

$$\langle a_{\ell m} a^*_{\ell m} \rangle = C_\ell \delta_{\ell\ell'} \delta_{mm'}, \tag{3.7}$$

the average is taken over an ensemble of realisations. The quantity C_ℓ is the angular power spectrum:

$$C_\ell \equiv \langle |a_{\ell m}|^2 \rangle = \frac{1}{2\ell+1} \sum_{m=-\ell}^{m=+\ell} |a_{\ell m}|^2. \tag{3.8}$$

The estimation of the angular power spectrum C_ℓ, for statistically isotropic and Gaussian skies, is limited by the fact that we can only observe one particular realisation of the Universe. For full sky observations, C_ℓ is unbiased ($\langle C_\ell \rangle = C_\ell$) and minimises the variance[3]:

$$var(C_\ell) = \frac{2}{2\ell+1} C_\ell^2. \tag{3.9}$$

The eq. (3.9) represent the sample variance, so-called cosmic variance. It is an irreducible lower bound, especially for low multipoles, on the error in the measurements of the angular power spectrum coming from the fact that we observe fluctuations in only one universe.

---

[2] Spherical harmonic functions are a complete orthonormal set of functions on the surface of a sphere, defined as:

$$Y_{\ell m}(\theta,\varphi) = \sqrt{\frac{(2\ell+1)}{4\pi}\frac{(\ell-m)!}{\ell+m!}} P_\ell^m(\cos\theta) e^{im\varphi},$$

where $P_\ell^m \cos(\theta)$ are the Legendre polynomials.

[3] For $\ell = 1$ cosmic variance does not apply if the CMB dipole is caused by the proper-motion of the Solar System.

Usually the angular power spectrum is written in the form of the angular band power, defined as:

$$D_\ell = \frac{\ell(\ell+1)}{2\pi} C_\ell, \tag{3.10}$$

because for almost-scale-invariant fluctuation the angular band power spectrum D_ℓ is almost-constant for small multipole. Fig. 3.3 shows the band power spectrum for temperature, as published by Planck 2015 [1].

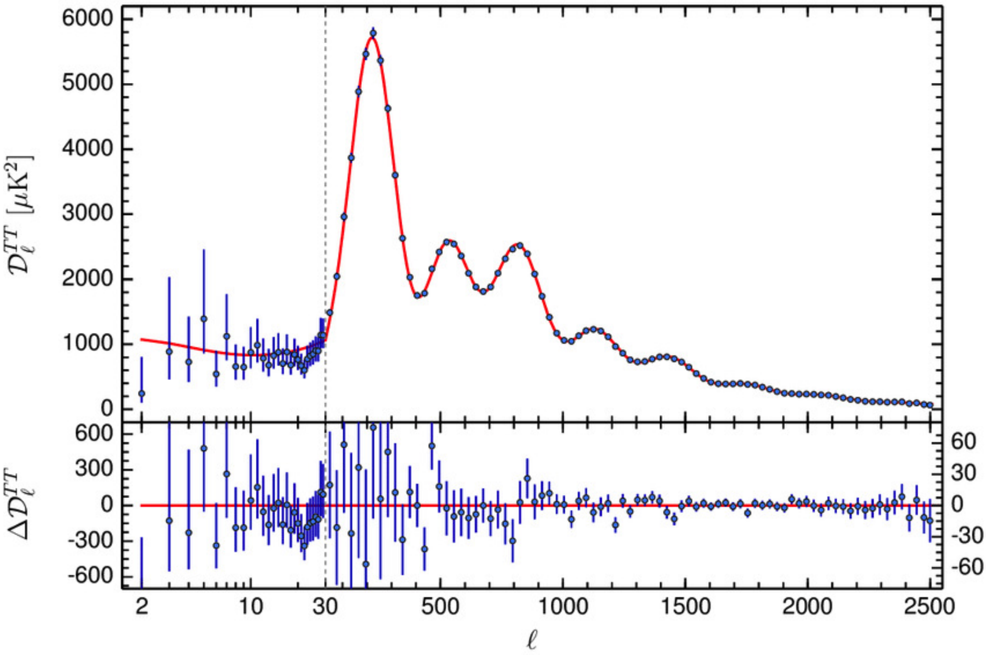

Figure 3.3: Angular band power (top) and residual angular band power (bottom) of the cosmic microwave temperature anisotropies as presented in the Planck 2015 release. The error bars show the sum of measurement error and cosmic variance, the latter being the dominant source of uncertainty at large angular scales [1].

If the power spectrum of fluctuations is Gaussian (as predicted by inflation and as current data suggest [7]) then only the even order correlation functions are non-zero and all of them can be directly expressed through the two-point correlation function $C(\phi)$, which, considering the eq.(3.7) can be write as:

$$\begin{aligned}
C(\phi) &= \langle \frac{\delta T}{T}(\theta,\varphi)\frac{\delta T}{T}(\theta',\varphi')\rangle = \\
&= \sum_{\ell m}\sum_{\ell' m'}\langle a^{T}_{\ell m}a^{*T}_{\ell' m'}\rangle Y_{\ell m}(\theta,\varphi)Y^{*}_{\ell' m'}(\theta',\varphi') = \\
&= \sum_{\ell m}\sum_{\ell' m'} C^{TT}_{\ell}\delta_{\ell\ell'}\delta_{mm'}Y_{\ell m}(\theta,\varphi)Y^{*}_{\ell' m'}(\theta',\varphi') = \\
&= \sum_{\ell m} C^{TT}_{\ell}Y_{\ell m}(\theta,\varphi)Y^{*}_{\ell m}(\theta',\varphi') = \\
&= \sum_{\ell} C^{TT}_{\ell}\sum_{\ell m}Y_{\ell m}(\theta,\varphi)Y^{*}_{\ell m}(\theta',\varphi') = \\
&= \sum_{\ell}\frac{2\ell+1}{4\pi}C^{TT}_{\ell}P_{\ell}(\cos\phi), \qquad (3.11)
\end{aligned}$$

where ($\cos\phi = \hat{n}\cdot\hat{n'}$) and the $\hat{n}$, $\hat{n}'$ are unit vectors pointing respectively in the directions identified by (θ,φ) and (θ',φ'). $P_{\ell}(\cos\phi)$ are the Legendre Polynomials:

$$P_{\ell}(\cos\phi) = \frac{4\pi}{2\ell+1}\sum_{m=-\ell}^{+\ell}Y_{\ell m}(\theta,\varphi)Y^{*}_{\ell m}(\theta',\varphi'). \qquad (3.12)$$

The three-point function, also known as the bispectrum, is a sensitive test for a non-Gaussian contribution to the fluctuation spectrum since it is precisely zero in the Gaussian limit.

If we consider $\phi = 0$ the two-point correlation function becomes the variance in the space of pixels:

$$var^{TT} = C_2(0) = \sum_{l}\frac{2l+1}{4\pi}C^{TT}_{l}. \qquad (3.13)$$

The CMB is also linearly polarized, because when the CMB was produced the photons of the CMB interacted with the matter through scattering Thompson. Thus in addition to the angular power spectra of the temperature we have also the power spectra of the polarisation.

We list now possible sources of anisotropy. First, on a scale of $\ell = 1$ there is the dipole anisotropy. The dipole, which is at the level of ∼3mK, is one of the most important calibrators in modern cosmology. In fact, it is interpreted as the effect of Doppler shift and aberration due to the proper motion of the Solar System with respect to a cosmological rest frame. The amplitude of the dipole anisotropy is around $\Delta T_D/T_0 = 10^{-3} = v/c$, where v is the velocity of the observer. After subtracting the Earth's motion around the Sun, and the

Sun's motion around the galactic centre, one can determine the velocity of our Galaxy with respect to this cosmological rest frame, which is of $v = 600$ kms^{-1} in the direction of the constellations of Hydra-Centaurus.

On smaller scales, from the quadrupole ($\ell = 2$), there are the following sources of primary anisotropies:

- Sachs-Wolfe effect [42]: inhomogeneities in the distribution of matter on the surface of last scattering can generate anisotropies by the redshift or blueshift of photons from regions of different gravitational potential;
- doppler effect: material moving on the last scattering induces temperature fluctuations by the Doppler effect;
- density contribution: the coupling between matter and radiation at last scattering means that overdense regions are intrinsically hotter than underdense regions;

and secondary ones:

- Sunyaev-Zel'dovich effect [46]: anisotropy produced by inverse Compton scattering of CMB photons by free electrons in a hot intergalactic plasma, between the observer and the last scattering surface;
- Integrated Sachs-Wolfe (ISW) effect [8]: photons passing through a time-varying gravitational potential field along the line of sight also suffer an effect similar to the Sachs-Wolfe effect.

On scales that are super-horizon at recombination the Sachs-Wolfe and the late-time Integrated Sachs-Wolfe (ISW) dominate the photon redshifting effects. On sub-horizon scales overdensities recombine later and are redshifted less and hence appear hot. At around $\ell \sim 60$ the anisotropies are dominated by Doppler signals from velocities at last-scattering because the density contribution cancels with the Sachs-Wolfe. As shown in Fig. 3.4 there is no scale on which the Sachs-Wolfe limit is accurate, and only at $\ell \ll 60$ are Doppler effects negligible. In the region $10 \leq \ell \leq 100$ the signal has contributions from Doppler, Sachs-Wolfe and density perturbations of comparable magnitudes, as well as a significant early Sachs-Wolfe contribution.

3.4 CMB Anomalies

The CMB anisotropy maps are in a very good agreement with the six-parameter ΛCDM model specified by the expansion rate (Hubble constant), the energy densities of dark matter and baryons, the reionisation optical

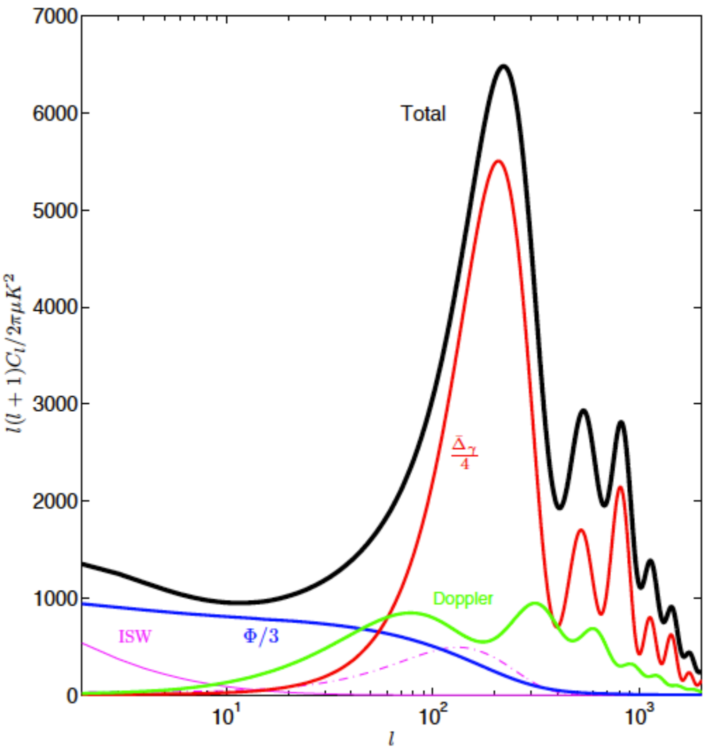

Figure 3.4: Power spectrum of the contributions to the total CMB temperature anisotropy D_ℓ^{TT}. At the small-scale, the density $\bar{\Delta}_\gamma$ (red solid line) is the main contribution from the comoving temperature perturbations at last-scattering. $\Phi/3$ (blue solid line) is the net large-scale contribution from photons climbing out of potential wells (Sachs-Wolf and ISW). $\Phi/3$ and $\bar{\Delta}_\gamma$ source terms have opposite sign, thus their total contribution to the power spectrum is nearly zero at $\ell \sim 60$, where the total is then dominated by the Doppler term (green solid line). The magenta ISW contributions come from the late-time change in the potentials when dark energy becomes important at low redshift (magenta solid line), and the early contribution (magenta dash-dotted line) from time-varying potentials soon after recombination as the Universe became fully matter rather than radiation dominated [33].

depth, and the amplitude and spectral index of primordial scalar fluctuations [5]. But several unexpected features have been observed in the microwave sky at large angular scales, both by WMAP and by Planck[6]. In particular, the maps of temperature anisotropies exhibit low variance, a lack of correlation on the largest angular scales [43], a preference for odd parity modes [31], a hemispherical power asymmetry [20], alignment between various low multipole moments [39], alignment between those low multipole moments and the motion and geometry of the Solar System [17], and an unexpectedly large cold spot in the Southern hemisphere [50]. For a review of the CMB anomalies, see Ref. [43].

Of course the explanations for these large-scale CMB features are three: they could have cosmological origins [15], they could be artifacts of astrophysical systematics or they could be statistical flukes. The possibility that they are due to instrumental systematic is quite low since two independent experiment (WMAP and Planck) agree on these features.

Better understanding of the anomalies will be driven in the future by observations of new quantities on very large spatial scales, such as lensing [52] and CMB polarization [16], as well as large-scale structure [21].

3.4.1 Lack of Power Anomaly

Historically, the first observed anomalous features, already within the COBE data, was the smallness of the quadrupole moment. It confirmed to be low when WMAP released its data [12]. However it was also shown that cosmic variance allows for such a small value. Another rediscovery in the first release of WMAP [12] was that the angular two-point correlation function, see eq. (3.11), at angular scales larger than 60 degrees is unexpectedly close to zero, where a non-zero correlation signal was expected. This feature had already been observed by COBE [29], and was rediscoveried by WMAP. Fig. 3.5 shows the two-point correlation function as observed with Planck [6]. Detailed further investigations of the lack of angular correlation have been presented in [17, 26].

Another intriguing feature, that seems to be correlated with a low quadrupole and with the lack of angular correlation, is the lack of power anomaly at the largest angular scales of the CMB anisotropy temperature pattern [43]. This anomaly consists in a missing of power, at these scales, with respect to what foreseen by the cosmological ΛCDM model and cannot be explained by a lack of quadrupole power alone. This effect has been studied with the variance estimator in WMAP data [35, 18, 27] and in Planck 2013 [4] and 2015 [6] data, measuring a lower-tail-probability (henceforth LTP) at the level of per cent.

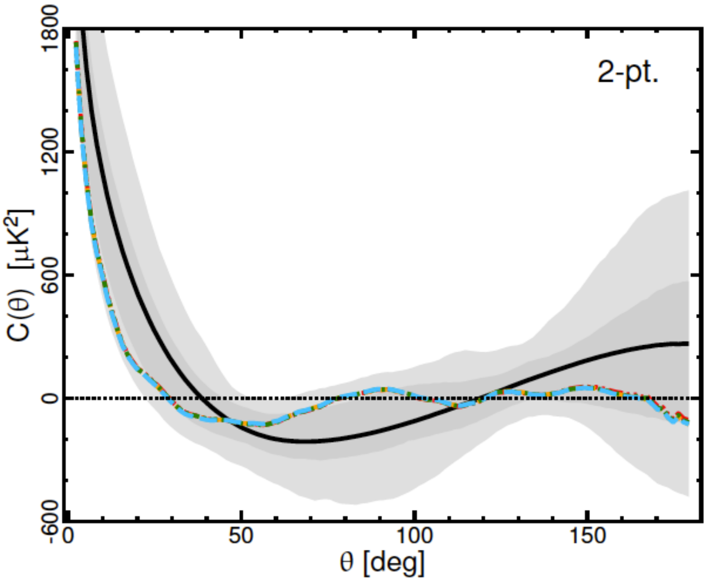

Figure 3.5: Angular two-point correlation function as observed by Planck [6]. The full black line and the shaded regions are the expectation from 1000 SMICA simulations based on the ΛCDM model and the 68% and 95% confidence regions. The plot also shows four colored lines that fall on top of each other and represent the results of the Planck analysis of the Commander, SEVEM, NILC and SMICA maps at resolution $N_{side} = 64$. While the measured two-point correlation is never outside the 95% confidence region, the surprising feature is that we observe essentially no correlations at $70° < \theta < 170°$ and a significant lack of correlations at $\theta > 60°$ [43].

This power deficit anomaly could be naturally explained by an early fast-roll phase of the inflatonary scalar field: hence this feature might witness a new cosmological phase before the standard inflationary era (see e.g. [24, 28, 25] and references therein).

3.5 CMB Polarisation

Thomson scattering of temperature anisotropies on the last scattering surface produces a linear polarisation pattern on the sky that can be simply read off from their quadrupole moments (see e.g. [30] and references therein). The gravitational instability paradigm predicts that the CMB anisotropies are polarised. According to this paradigm, small fluctuations in the early universe grow into the large scale structure we observe in the present day Universe. If the temperature anisotropies are indeed the result of primordial fluctuations, their presence at last scattering would polarise the CMB anisotropies themselves. Therefore the polarisation of the CMB represents a fundamental check on our basic assumptions about the behavior of fluctuations in the Universe. The polarisation power spectrum provides information complementary to the temperature power spectrum. This can be used in breaking parameter degeneracies and constraining cosmological parameters more accurately or in searching the counterpart of particular features observed in the temperature power spectrum.

The polarised signal is really fainter than the signal in temperature: it is at the 10^{-6} level, representing a significant experimental challenge.

3.5.1 From Anisotropies to Polarisation

The Thomson scattering cross section depends on polarisation as (see e.g. [13]):

$$\frac{d\sigma_T}{d\Omega} \propto |\hat{\epsilon} \cdot \hat{\epsilon}'|, \tag{3.14}$$

where $\hat{\epsilon}$ ($\hat{\epsilon}'$) are the incident (scattered) polarisation directions. The incident light sets up oscillations of the target electron in the direction of the electric field vector $\vec{E}$. Thus, the scattered radiation intensity peaks in the direction normal to, with polarisation parallel to, the incident polarisation. More formally, the polarisation dependence of the cross section is dictated by electromagnetic gauge invariance.

If the incoming radiation field were isotropic, orthogonal polarisation states from incident directions separated by $\pi/2$ would balance so that the outgoing radiation would remain unpolarised. Conversely, if the incident radiation field possesses a quadrupolar variation in intensity or temperature (which possess intensity peaks at $\pi/2$ separations), the result is a linear polarisation of the scattered radiation, see Fig. 3.6. If Thomson scattering is rapid, then the randomization of photon directions that results destroys any quadrupole anisotropy and polarisation. The problem of understanding the polarisation pattern of the CMB thus reduces to understanding the quadrupolar temperature fluctuations at last scattering.

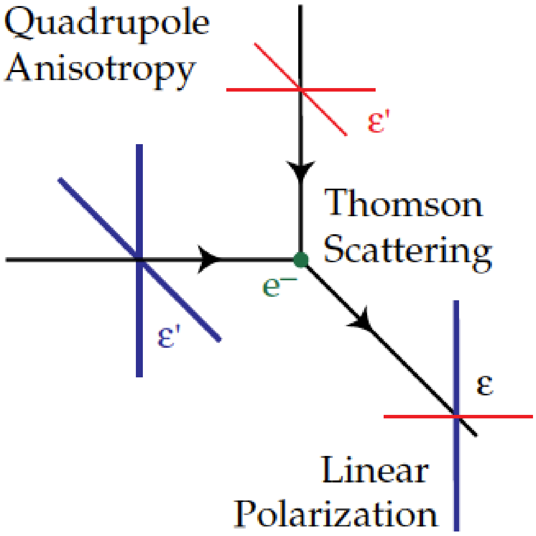

Figure 3.6: Thomson scattering of radiation with a quadrupole anisotropy generates linear polarisation. Blue colors (thick lines) represent hot and red colors (thin lines) cold radiation.

3.5.2 Polarisation E and B modes

The linear polarisation can be described using the Stokes parameters U and Q (whereas the Stokes parameter V defines the circular polarisation state). The Stokes Q and U parameters are defined with respect to a fixed coordinate system in the sky. While such a coordinate system is well defined over a small patch in the sky, it becomes ambiguous once the whole sky is considered because one cannot define a rotationally invariant orthogonal basis on a sphere. Thus, if one wants to analyze the auto-correlation function of polarization or perform directly the power spectrum analysis on the data then a more general analysis of polarization is required: one can define rotationally invariant electric and magnetic-type parity fields E and B from the usual Q and U Stokes parameters [53].

The CMB radiation field is characterized by a 2×2 intensity tensor I_{ij}. The Stokes parameters Q and U are defined as:

$$Q = \frac{(I_{11} - I_{22})}{4}, \tag{3.15}$$

$$U = \frac{I_{12}}{2}, \tag{3.16}$$

while the temperature anisotropy is given by:

$$T = \frac{(I_{11} + I_{22})}{4}. \tag{3.17}$$

While the temperature is invariant under a right handed rotation in the plane perpendicular to direction $\hat{n}$, Q and U transform under rotation by an angle ϕ as:

$$\begin{aligned} Q' &= Q\cos 2\phi + U \sin 2\phi, \\ U' &= -Q \sin 2\phi + U \cos 2\phi, \end{aligned} \tag{3.18}$$

where $\hat{e}'_1 = \hat{e}_1 \cos\phi + \hat{e}_2 \sin\phi$ and $\hat{e}'_2 = -\hat{e}_1 \sin\phi + \hat{e}_2 \cos\phi$. This means we can construct two quantities from the Stokes Q and U parameters that have spin-2:

$$(Q \pm iU)'(\hat{n}) = e^{\mp 2i\phi}(Q \pm iU)(\hat{n}). \tag{3.19}$$

We may therefore expand each of the quantities in the appropriate spin-weighted basis:

$$T(\hat{n}) = \sum_{lm} a^T_{lm} Y_{lm}((\hat{n}), \tag{3.20}$$

$$(Q + iU)(\hat{n}) = \sum_{lm} a^{(2)}_{lm}{}_2Y_{lm}(\hat{n}), \tag{3.21}$$

$$(Q - iU)(\hat{n}) = \sum_{lm} a^{(-2)}_{lm}{}_{-2}Y_{lm}(\hat{n}). \tag{3.22}$$

Q and U are defined at a given direction n with respect to the spherical coordinate system $(\hat{e}_\theta, \hat{e}_\varphi)$. The Stokes parameters are not invariant under rotations in the plane perpendicular to $(\hat{n})$. However, one can use the spin raising and lowering operators $\acute{\partial}$ and $\bar{\acute{\partial}}$ (defined in [53]) to obtain spin zero quantities, which have the advantage of being rotationally invariant like the temperature and no ambiguities connected with the rotation of coordinate system arises. Acting twice with $\acute{\partial}$, $\bar{\acute{\partial}}$ on $(Q+iU)$ in equation (3.22) leads to:

$$\begin{aligned}
\bar{\acute{\partial}}^2(Q+iU)(\hat{n}) &= \sum_{lm}\left[\frac{(\ell+2)!}{(\ell-2)!}\right]^{1/2} a_{lm}^{(2)} Y_{lm}(\hat{n}), && (3.23)\\
\acute{\partial}^2(Q-iU)(\hat{n}) &= \sum_{lm}\left[\frac{(\ell+2)!}{(\ell-2)!}\right]^{1/2} a_{lm}^{(-2)} Y_{lm}(\hat{n}), && (3.24)
\end{aligned}$$

and the expressions for the expansion coefficients are:

$$\begin{aligned}
a_{lm}^{T} &= \int d\Omega Y_{lm}^{*}((\hat{n})T(\hat{n}), && (3.25)\\
a_{lm}^{(2)} &= \int d\Omega_2 Y_{lm}^{*}(\hat{n})(Q+iU)(\hat{n}), &&\\
&= \left[\frac{(\ell+2)!}{(\ell-2)!}\right]^{-1/2} \int d\Omega Y_{lm}^{*}(\hat{n})\bar{\acute{\partial}}^2(Q+iU)(\hat{n}), && (3.26)\\
a_{lm}^{(-2)} &= \int d\Omega_{-2} Y_{lm}^{*}(\hat{n})(Q-iU)(\hat{n}), &&\\
&= \left[\frac{(\ell+2)!}{(\ell-2)!}\right]^{-1/2} \int d\Omega Y_{lm}^{*}(\hat{n})\acute{\partial}^2(Q-iU)(\hat{n}). && (3.27)
\end{aligned}$$

Instead of $a_{lm}^{(2)}$ and $a_{lm}^{(-2)}$ it is convenient to introduce their linear combinations:

$$\begin{aligned}
a_{lm}^{(E)} &= -\frac{(a_{lm}^{(2)}+a_{lm}^{(-2)})}{2} && (3.28)\\
a_{lm}^{(B)} &= i\frac{(a_{lm}^{(2)}+a_{lm}^{(-2)})}{2} && (3.29)
\end{aligned}$$

These two combinations behave differently under parity transformation: while E remains unchanged, B changes the sign, in analogy with the electric and magnetic fields. The power spectra are given by:

$$\begin{aligned}
\langle a_{\ell m}^{E} a_{\ell m}^{*E}\rangle = C_{\ell}^{EE}\delta_{\ell\ell'}\delta_{mm'}, && (3.30)\\
\langle a_{\ell m}^{B} a_{\ell m}^{*B}\rangle = C_{\ell}^{BB}\delta_{\ell\ell'}\delta_{mm'}. && (3.31)
\end{aligned}$$

The cross-correlation of E-modes with the temperature is:

$$\langle a_{\ell m}^{T} a_{\ell m}^{*E}\rangle = C_{\ell}^{TE}\delta_{\ell\ell'}\delta_{mm'}, \qquad (3.32)$$

other cross-correlations vanish if parity is conserved. Fig. 3.7 shows the spectra D_{ℓ}^{TE} and D_{ℓ}^{EE} as measured by Planck [6].

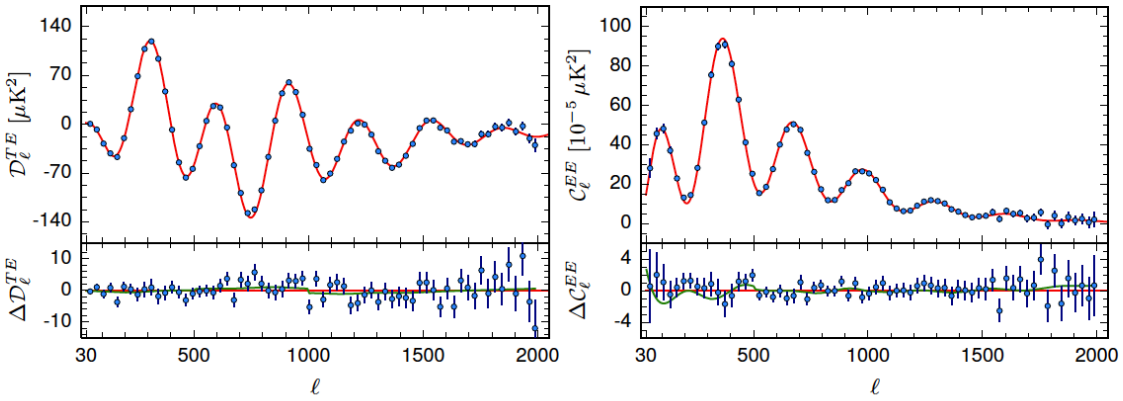

Figure 3.7: Frequency-averaged TE (left) and EE (right) spectra. The theoretical TE and EE spectra plotted in the upper panels are computed from the best-fit model of Fig 3.3. Residuals with respect to this theoretical model are shown in the lower panels. The error bars show $\pm 1\sigma$ uncertainties. The green lines in the lower panels show the best-fit temperature-to-polarization leakage model, fitted separately to the TE and EE spectra[1].

3.5.3 Observations

While the theoretical case for observing polarisation is strong, it is a difficult experimental task to observe signals of the low level of several μK and below. Given that the amplitude of the polarisation is so small the question of foregrounds is even more important than for the temperature anisotropy. Moreover, the level and structure of the various foreground polarisation in the CMB frequency bands is currently not well known. Atmospheric emission is believed to be negligibly polarised, leaving the main astrophysical foregrounds: dust, free-free [4], point source emissions and synchrotron, which is the most important polarisation foreground (see e.g. [4, 6]).

At the large angular scales the observations in temperature, as measured by Planck, are limited by the cosmic variance whereas for the polarisation the instrumental noise is several times bigger than the level of the cosmic variance. For this reason the future missions, like the satellite Litebird [47], are so important for the observation of the CMB polarisation.

---

[4] Bremsstrahlung emission is intrinsically unpolarised but can be partially polarised by Thomson scattering within the HII region. This is small effect which is expected to polarise the emission by less than 10%.

Chapter 4

Angular Power Spectrum of Random Variables

In this chapter we introduce a new set of objects, that we call the Angular Power Spectrum of Random Variables (APS of Random Variables), which as we will see are dimensionless normalised angular power spectra that allow to define a joint estimator which depends on temperature, E-mode polarisation ant their cross-correlation TE.

4.1 From C_ℓ to APS of Random Variables

The idea of APS of Random Variables starts from the usual equations employed to simulate temperature and E-mode CMB maps:

$$a^T_{\ell m} = \sqrt{C_\ell^{TT,th}}\xi^1_{\ell m}\,, \tag{4.1}$$

$$a^E_{\ell m} = \frac{C_\ell^{TE,th}}{\sqrt{C_\ell^{TT,th}}}\xi^1_{\ell m} + \sqrt{C_\ell^{EE,th} - \frac{(C_l^{TE,th})^2}{C_\ell^{TT,th}}}\xi^2_{\ell m}, \tag{4.2}$$

where $a^{T,E}_{\ell m}$ are the coefficients of the spherical harmonics, $C_\ell^{TT,th}$, $C_\ell^{EE,th}$ and $C_\ell^{TE,th}$ are the theoretical angular power spectra for TT, EE and TE and with $\xi^{1,2}_{\ell m}$ being Gaussian random variables, uncorrelated, with zero mean and unit variance:

$$\langle \xi^1_{\ell m} \rangle = 0\,, \tag{4.3}$$

$$\langle \xi^2_{\ell m} \rangle = 0\,, \tag{4.4}$$

$$\langle \xi^1_{\ell m}\xi^2_{\ell' m'} \rangle = 0\,, \tag{4.5}$$

$$\langle \xi^1_{\ell m}\xi^1_{\ell' m'} \rangle = \langle \xi^2_{\ell m}\xi^2_{\ell' m'} \rangle = \delta_{\ell\ell'}\,\delta_{mm'}\,. \tag{4.6}$$

We now introduce a vectorial notation, defining two vectors with $(2l+1)$ components:

$$\vec{\xi}_\ell^{(1)} = (\xi^1_{-\ell}, ..., \xi^1_0, ..., \xi^1_{+\ell}), \quad \vec{\xi}_\ell^{(2)} = (\xi^2_{-\ell}, ..., \xi^2_0, ..., \xi^2_{+\ell}) \tag{4.7}$$

From equation (4.1),(4.2) one can compute the corresponding angular power spectra, defined as:

$$\begin{aligned} C_\ell^{TT,sim} &= \frac{1}{2\ell+1}\sum_{m=-\ell}^{\ell} a^T_{\ell m}(a^T_{\ell m})^*\,, && (4.8)\\ C_\ell^{TE,sim} &= \frac{1}{2\ell+1}\sum_{m=-\ell}^{\ell} a^T_{\ell m}(a^E_{\ell m})^*\,, && (4.9)\\ C_\ell^{EE,sim} &= \frac{1}{2\ell+1}\sum_{m=-\ell}^{\ell} a^E_{\ell m}(a^E_{\ell m})^*\,, && (4.10)\end{aligned}$$

where the label *sim* stands for “simulated”, i.e. realised randomly from the theoretical spectra $C_\ell^{TT,th}$, $C_\ell^{EE,th}$ and $C_\ell^{TE,th}$, finding the following expressions:

$$\begin{aligned} C_\ell^{TT,sim} &= C_\ell^{TT,th}\frac{|\vec{\xi}_\ell^{(1)}|^2}{2\ell+1}\,, && (4.11)\\ C_\ell^{EE,sim} &= \frac{(C_\ell^{TE,th})^2}{C_\ell^{TT,th}}\left[\frac{|\vec{\xi}_\ell^{(1)}|^2}{2\ell+1} - \frac{|\vec{\xi}_\ell^{(2)}|^2}{2\ell+1}\right] + C_\ell^{EE,th}\frac{|\vec{\xi}_\ell^{(2)}|^2}{2\ell+1} \\ &\quad +2a_\ell\frac{C_\ell^{TE,th}}{C_\ell^{TT,th}}\frac{\vec{\xi}_\ell^{(1)}\cdot\vec{\xi}_\ell^{(2)}}{2\ell+1}\,, && (4.12)\\ C_\ell^{TE,sim} &= C_\ell^{TE,th}\frac{|\vec{\xi}_\ell^{(1)}|^2}{2\ell+1} + a_\ell\frac{\vec{\xi}_\ell^{(1)}\cdot\vec{\xi}_\ell^{(2)}}{2\ell+1}\,, && (4.13)\end{aligned}$$

where a_ℓ is defined as:

$$a_\ell = \sqrt{C_\ell^{EE,th}C_\ell^{TT,th} - (C_\ell^{TE,th})^2} \tag{4.14}$$

It is easy to show that taking the ensemble average of equations (4.11), (4.12), (4.13) yields to:

$$\begin{aligned} \langle C_\ell^{TT,sim}\rangle &= C_\ell^{TT,th}\,, && (4.15)\\ \langle C_\ell^{EE,sim}\rangle &= C_\ell^{EE,th}\,, && (4.16)\\ \langle C_\ell^{TE,sim}\rangle &= C_\ell^{TE,th}\,, && (4.17)\end{aligned}$$

since for each ℓ, as a consequence of equations (4.5),(4.6):

$$\begin{aligned} \langle \frac{|\vec{\xi}^{(1)}_\ell|^2}{2\ell+1} \rangle &= 1\,, && (4.18) \\ \langle \frac{|\vec{\xi}^{(2)}_\ell|^2}{2\ell+1} \rangle &= 1\,, && (4.19) \\ \langle \vec{\xi}^{(1)}_\ell \cdot \vec{\xi}^{(2)}_\ell \rangle &= 0\,. && (4.20) \end{aligned}$$

Equations (4.11),(4.12) and (4.13) can be inverted, giving the following set of equations:

$$\begin{aligned} \frac{|\vec{\xi}^{(1)}_\ell|^2}{2\ell+1} &= \frac{C_\ell^{TT}}{C_\ell^{TT,th}}\,, && (4.21) \\ \frac{|\vec{\xi}^{(2)}_\ell|^2}{2\ell+1} &= \frac{C_\ell^{EE}}{a_\ell^2} C_\ell^{TT,th} - \frac{C_\ell^{TT,th}}{a_\ell^2} \left(\frac{C_\ell^{TE,th}}{C_\ell^{TT,th}} \right)^2 C_\ell^{TT} \\ &\quad -2\frac{C_\ell^{TE,th}}{a_\ell^2} \left[C_\ell^{TE} - \frac{C_\ell^{TE,th}}{C_\ell^{TT,th}} C_\ell^{TT} \right]\,, && (4.22) \\ \frac{\vec{\xi}^{(1)}_\ell \cdot \vec{\xi}^{(2)}_\ell}{2\ell+1} &= \frac{1}{a_\ell} \left[C_\ell^{TE} - \frac{C_\ell^{TE,th}}{C_\ell^{TT,th}} C_\ell^{TT} \right]\,, && (4.23) \end{aligned}$$

where we have dropped out the label "sim" for sake of simplicity. Now, we can interpret C_ℓ^{TT}, C_ℓ^{EE} and C_ℓ^{TE} as the CMB angular power spectra recovered by a CMB experiment under realistic circumstances, i.e. including noise residuals, incomplete sky fraction and finite angular resolution[1].

Once the model is chosen, i.e. once the spectra $C_\ell^{TT,th}$, $C_\ell^{EE,th}$ and $C_\ell^{TE,th}$ are fixed, for example to ΛCDM, one can compute the following APS of Random Variables:

$$\begin{aligned} x_\ell^1 &\equiv \frac{|\vec{\xi}^{(1)}_\ell|^2}{2\ell+1}\,, && (4.24) \\ x_\ell^2 &\equiv \frac{|\vec{\xi}^{(2)}_\ell|^2}{2\ell+1}\,, && (4.25) \\ x_\ell^3 &\equiv \frac{\vec{\xi}^{(1)}_\ell \cdot \vec{\xi}^{(2)}_\ell}{2\ell+1}\,, && (4.26) \end{aligned}$$

for the observations or the considered simulations, which are not ideal but contain also the contributions coming from the realistic circumstances proper of a CMB experiment.

---

[1] In principle one can also include residual of systematic effects.

As one can see, between the APS of Random Variables and the angular power spectra C_ℓ^{TT}, C_ℓ^{EE} and C_ℓ^{TE} there is a complicated mapping. The advantage of using APS of Random Variables is that they are dimensionless and homogeneous numbers and can be easily combined to define a 1-D estimator which depends on temperature, E-mode polarisation and their cross-correlation. A natural definition of this 1-D estimator, called P, is the following:

$$P = \frac{1}{(\ell_{max}-1)} \sum_{\ell=2}^{\ell_{max}} \left(x_\ell^1 + x_\ell^2 \right) . \tag{4.27}$$

The estimator P could be interpreted as a dimensionless normalised mean power, which jointly combines the temperature and polarisation data. An improvement of the P estimator is represented by $\tilde{P}$, the minimun variance version of P , in which the polarised part is not weighted as the temperature one (see section 6.2.2). In the statistical analysis we use both these estimators to evaluate the lack of power anomaly.

Chapter 5

Monte Carlo Simulations and Data Set

In the analysis led in this thesis we consider only the largest angular scales, i.e. $2 \leq l \leq 30$ of the CMB power patterns since the features of lack of power is localised at these scales.

We use the latest public *Planck* satellite CMB temperature data[1], i.e. the Planck 2015 Commander map with its Standard Mask, see Fig. 5.1, whose sky fraction f_{sky} is $f^T_{sky} = 93.6$, which enters the temperature sector of the low-ℓ PLANCK likelihood. [10]. In polarisation we consider a noise weighted

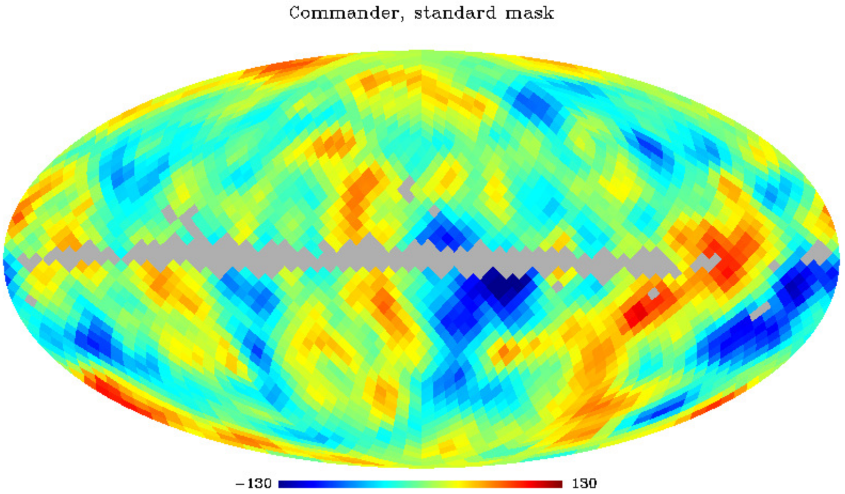

Figure 5.1: Planck 2015 COMMANDER map with its STANDARD MASK

---

[1] http://www.cosmos.esa.int/web/planck/pla.

combination of WMAP9 and PLANCK data as done in [32] (this allows to gain signal-to-ratio and to deal with a larger sky fraction in polarisation, $f_{sky}^{P} = 73.9$). Temperature and polarisation maps are sampled at HEALPix[2] [22] resolution $N_{side} = 16$. For sake of simplicity we will refer to this data set as the Planck 2015 $low - \ell$ data set, even if in the polarisation we also consider WMAP-9-years data.

We follow a frequentist approach, considering Monte Carlo simulations from the ΛCDM model, which, consistently with the Planck 2015 $low-\ell$ data set do include realistic effects from the residual instrumental noise (correlated in the polarisation), beams and incomplete sky fraction.

The six CMB angular power spectra have been estimated from 10000 CMB-plus-noise maps where their signal is extracted from the PLANCK fiducial ΛCDM angular power spectra and where their noise is simulated through Cholesky decomposition of the total noise covariance matrix in pixel space. Such estimates are obtained with the use of an optimal angular power spectrum estimator, *BolPol* [23], which implements a quadratic maximum likelihood (QML) technique ([48]). QML estimators are called optimal since they are unbiased and minimum variance (it saturates the Fisher-Cramer-Rao bound ([37]), therefore no other estimators can perform better).

5.1 Validation of the Monte Carlo

Before implementing any estimator on public Planck 2015 $low-\ell$ data and on realistic Monte Carlo simulations, we need to validate the simulations both for the CMB angular power spectra and for the APS of Random Variables. To this aim, for each multipole ℓ included in the range of $2 - 30$ we have evaluated the deviation between the average of the MC simulations in terms of uncertainties of the means [3], σ_μ, and the fiducial.

5.1.1 Angular Power Spectra

The validation of the MC simulations of angular power spectra is shown in Fig. 5.2, where the average of the band power D_ℓ^{TT}, D_ℓ^{EE}, D_ℓ^{TE} and D_ℓ^{BB} (we omit to report D_ℓ^{TB} and D_ℓ^{EB} since those spectra will not be used) are

---

[2] http://healpix.sourceforge.net/.

[3] As uncertainties of the means we consider:

$$\sigma_\mu = \frac{\sigma}{\sqrt{N}}, \tag{5.1}$$

where N is the number of simulations and σ is the half of the width of the distributions which corresponds 68.3% of probability.

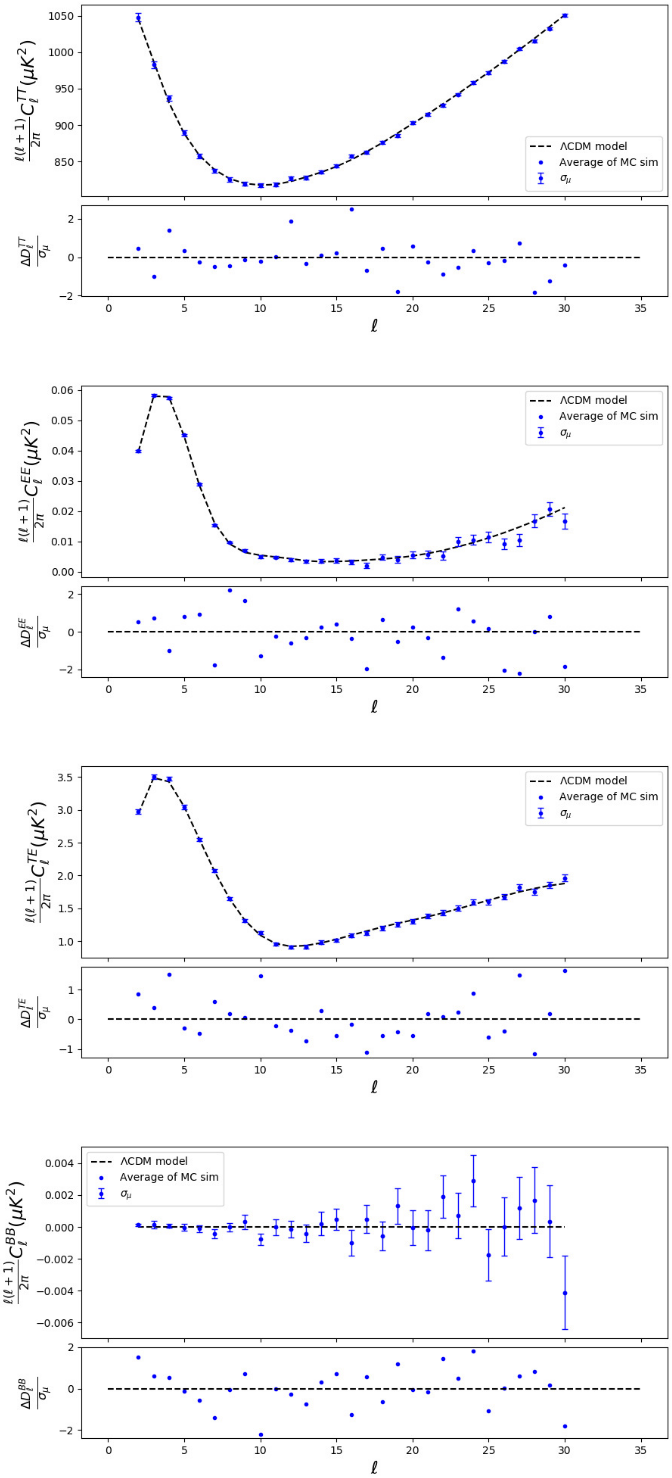

Figure 5.2: Averages of D_ℓ^{TT} (first panel), D_ℓ^{EE} (second panel), D_ℓ^{TE} (third panel) and D_ℓ^{BB} (fourth panel) as a function of ℓ obtained from MonteCarlo simulations corresponding to the Planck-WMAP low-ℓ data. Blue error bars represent the uncertainties associated to the averages. Each panel displays also a lower box where for each ℓ it is shown the distance of mean in units σ_μ. Dashed black lines represent what theoretically expected for $D_\ell^{TT,th}$, $D_\ell^{EE,th}$, $D_\ell^{TE,th}$ and $D_\ell^{BB,th}$.

displayed respectively in the upper, second, third and lower panels along with their uncertainties of the means σ_μ. Each panel presents also a lower box where for each ℓ it is shown the distance of mean in units of σ_μ.The condition:

$$D_\ell^{th} - \left(\frac{1}{N} \sum_{i=1}^{i=N} D_\ell^{sim} \right) \lesssim 3\sigma_{\mu,\ell} \tag{5.2}$$

is verified, therefore the MC simulations are considered as validated.

5.1.2 Angular Power Spectrum of Random Variables

The validation of the MC simulations of the APS of Random Variables x_ℓ^1, x_ℓ^2 and x_ℓ^3, see equations (4.24), (4.25), (4.26) is shown in Fig. 5.3, where the average of x_ℓ^1, x_ℓ^2 and x_ℓ^3 are displayed respectively in the upper, middle and lower panels along with their uncertainties of the means. Each panel presents also a lower box where for each ℓ it is shown the distance of mean in units of σ_μ. Also in this case the condition:

$$x_\ell^{j,th} - \left(\frac{1}{N} \sum_{i=1}^{i=N} x_\ell^{j,sim} \right) \lesssim 3\sigma_{\mu,\ell} \tag{5.3}$$

is satisfied. This can be seen as a validation of the algorithm used to build the APS of Random Variables since we have already validated the angular power spectra..

5.2 Planck Data

Through the statistical analysis of the MC simulations it is possible to compute the confidence regions at the levels of 68.3%, 95.5% and 99.7% (henceforth C.L.) with respect to ΛCDM model. As example, in Fig. 5.4 we show the empirical distributions of the N realisations of the band power D_l^{TT}, D_l^{EE}, D_l^{TE}, D_l^{BB}, for the multipole $\ell = 2$. with the C.L. and the value observed by Planck. Fig. 5.5 displays the comparison between simulations and Planck data for the power spectra D_ℓ^{TT} (first panel), D_ℓ^{EE} (second panel), D_ℓ^{TE} (third panel) and D_ℓ^{BB} (fourth panel) as a function of ℓ.

Another way to visualise the result is through the APS of Random variable. In the the 3D space $(x_\ell^1, x_\ell^2, x_\ell^3)$, for each ℓ, we obtain a cloud of N points, produced by the N realisations, around the model (the red star in the 3D plots), which has coordinates $(1, 1, 0)$. As example, Fig. 5.6 shows the cloud of points in the 3D space for the multipole $\ell = 3$. In Fig. 5.7 we show x_ℓ^1 (upper panel), x_ℓ^2 (middle panel) and x_ℓ^3 (lower panel) as a function

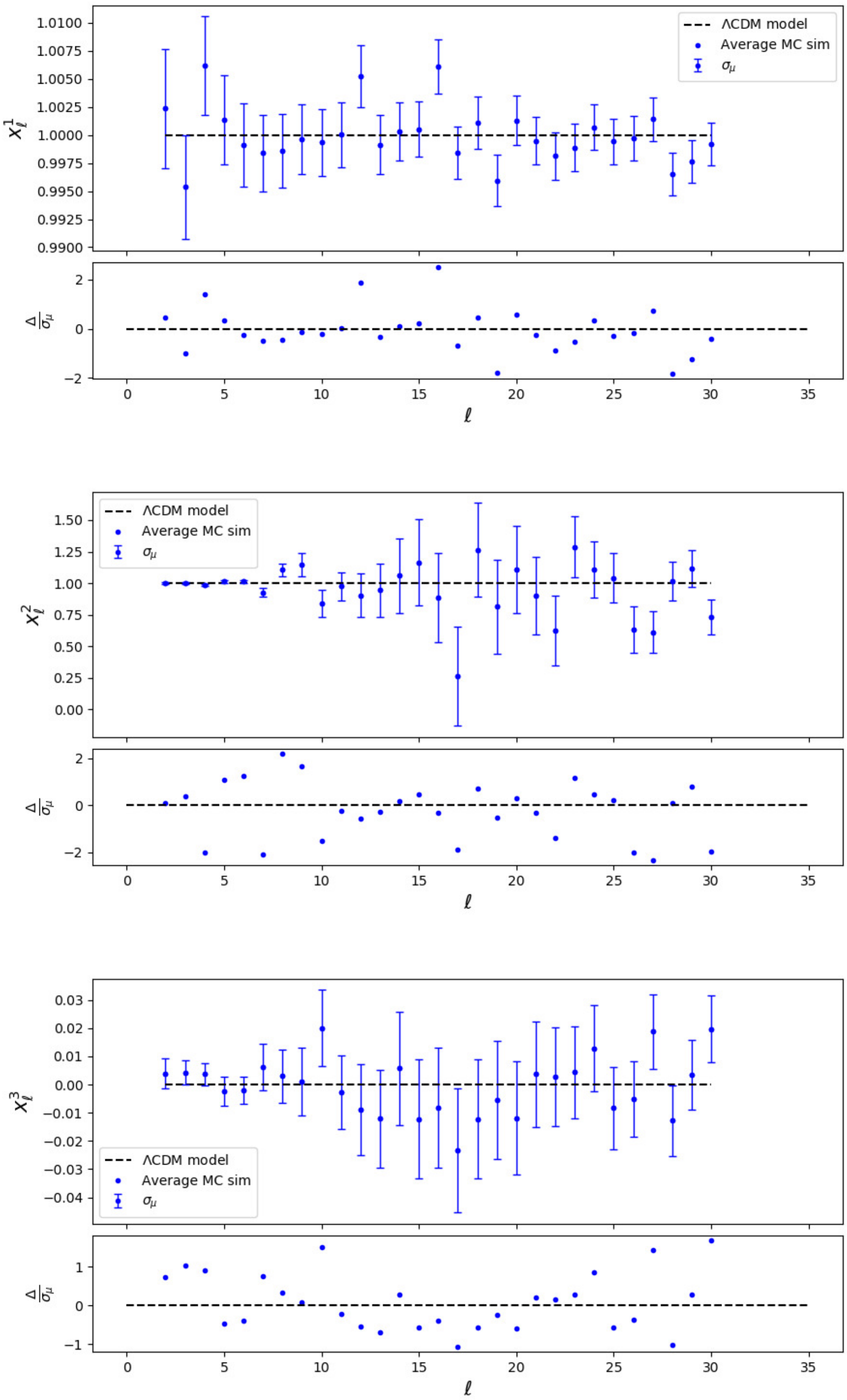

Figure 5.3: Averages of x_ℓ^1 (upper panel), x_ℓ^2 (middle panel) and x_ℓ^3 (lower panel) as a function of ℓ obtained from MonteCarlo simulations corresponding to the Planck-WMAP low-ℓ data. Error bars represent the uncertainties associated to the averages. Each panel displays also a lower box where for each ℓ it is shown the distance of mean in units of σ_μ. Dashed horizontal lines represent what theoretically expected for the averages of x_ℓ^1, x_ℓ^2 and x_ℓ^3, see equations (4.18),(4.19) and (4.20).

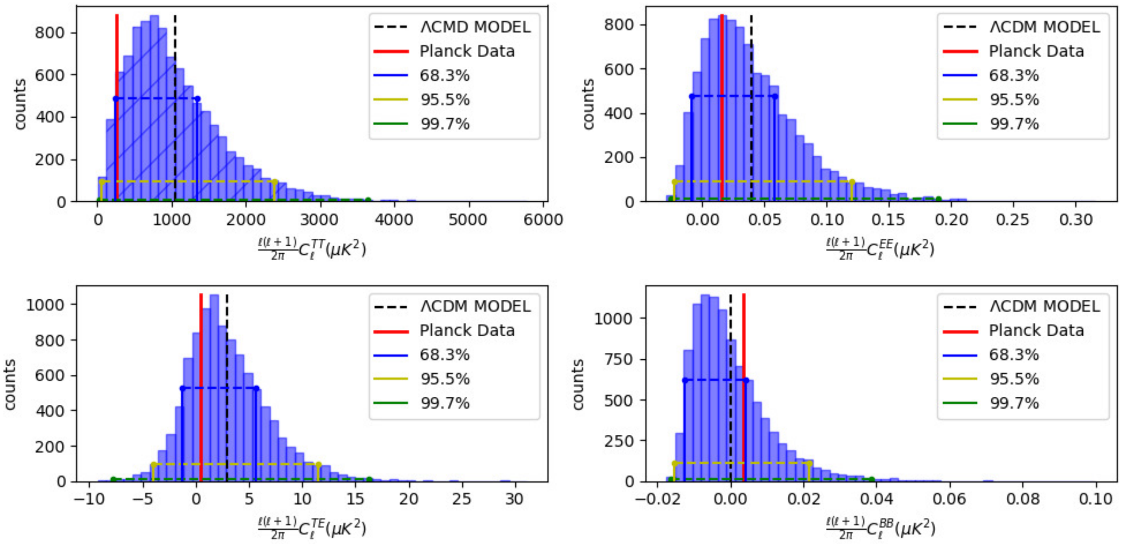

Figure 5.4: Histograms of the N realisation for the multipole $\ell = 2$ for the band power D_ℓ^{TT} (upper left panel), D_ℓ^{EE} (upper right panel), D_ℓ^{TE} (lower left panel) and D_ℓ^{BB} (lower right panel). The red line indicates the Planck Data D_l^{Planck}, whereas the dashed black line the ΛCMD Model. The blue, yellow and green lines indicate the boundaries of the 68.3%, 95.5% and 99.7% regions, respectively.

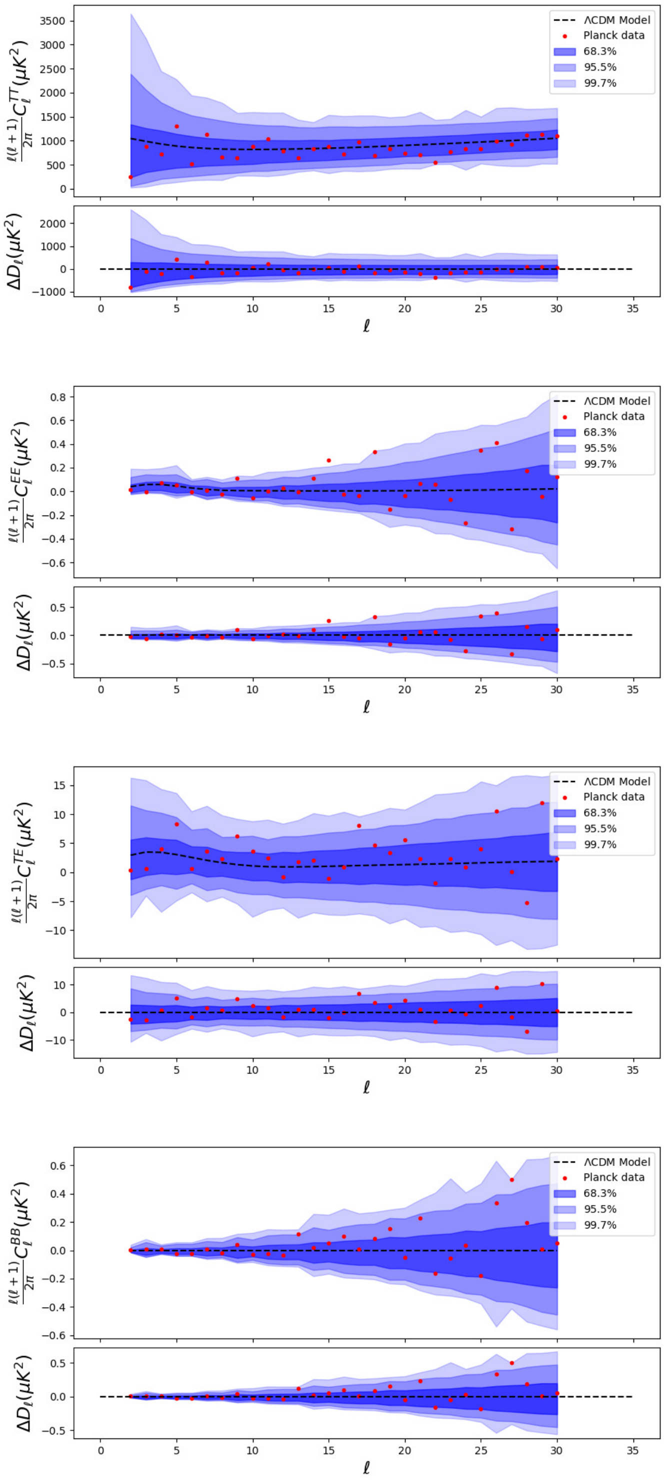

Figure 5.5: D_ℓ^{TT} (upper panel), D_ℓ^{EE} (second panel), D_ℓ^{TE} (third panel) and D_ℓ^{BB} (lower panel) as a function of ℓ obtained from the PLANCK-WMAP low-ℓ data set. The blue shaded area is for the 68.3%, 95.5% and 99.7% confidence levels with respect to ΛCDM model, represented with the dashed horizontal lines. Each panel displays also a lower box where for each ℓ it is shown the distance of the estimates from the model.

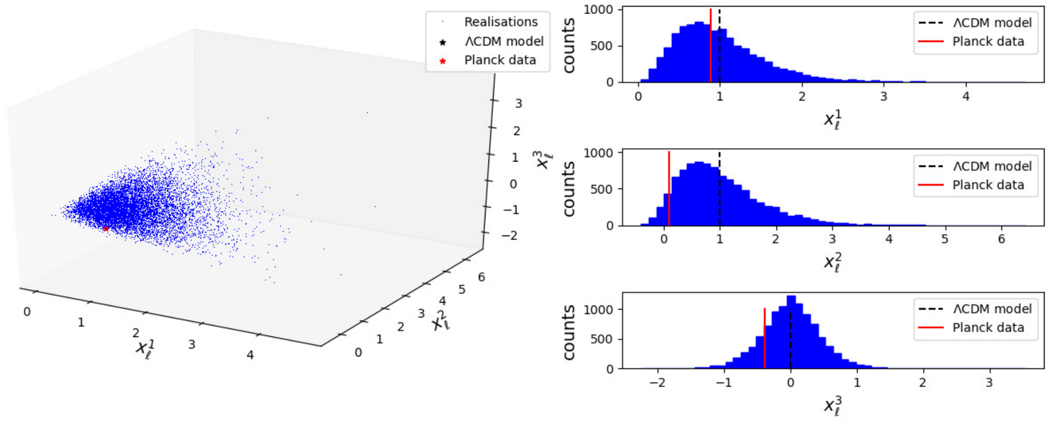

Figure 5.6: Cloud of N points, produced by the N realisations, in the 3D space $(x^1_\ell, x^2_\ell, x^3_\ell)$, for $\ell = 3$. The model is represented with a black star, the data with the red star. The three upper panels on the right side display the 1D-distribution of each random variables. The black dashed lines represent the model, and the red dashed lines represent the data.

of ℓ obtained from the PLANCK-WMAP low-ℓ data set and the C.L. w.r.t. the ΛCDM model.

Both for the spectra and for the APS of Random Variables, the data are always within the 99.7% regions.

It is important to note that both for the polarisation and the temperature at low-ℓ (in particular for $\ell \lesssim 10 - 15$) the number of data under the model are larger than the ones above. This observation calls for a quantitative and statistical assessment of this behavior both in temperature and polarisation. This feature indicates a deficit of power at large angular scale, and from this borne the importance of testing the lack of power considering in a jointly way the temperature and polarisation data.

5.3 Signal to Noise Ratio

The Signal to Noise ratio gives us information about the contribution of each multipole ℓ, in terms of signal. The S/N is defined as:

$$\left(\frac{S}{N}\right)^2 = \sum_{l=2}^{30} \left(\frac{S}{N}\right)^2_l . \tag{5.4}$$

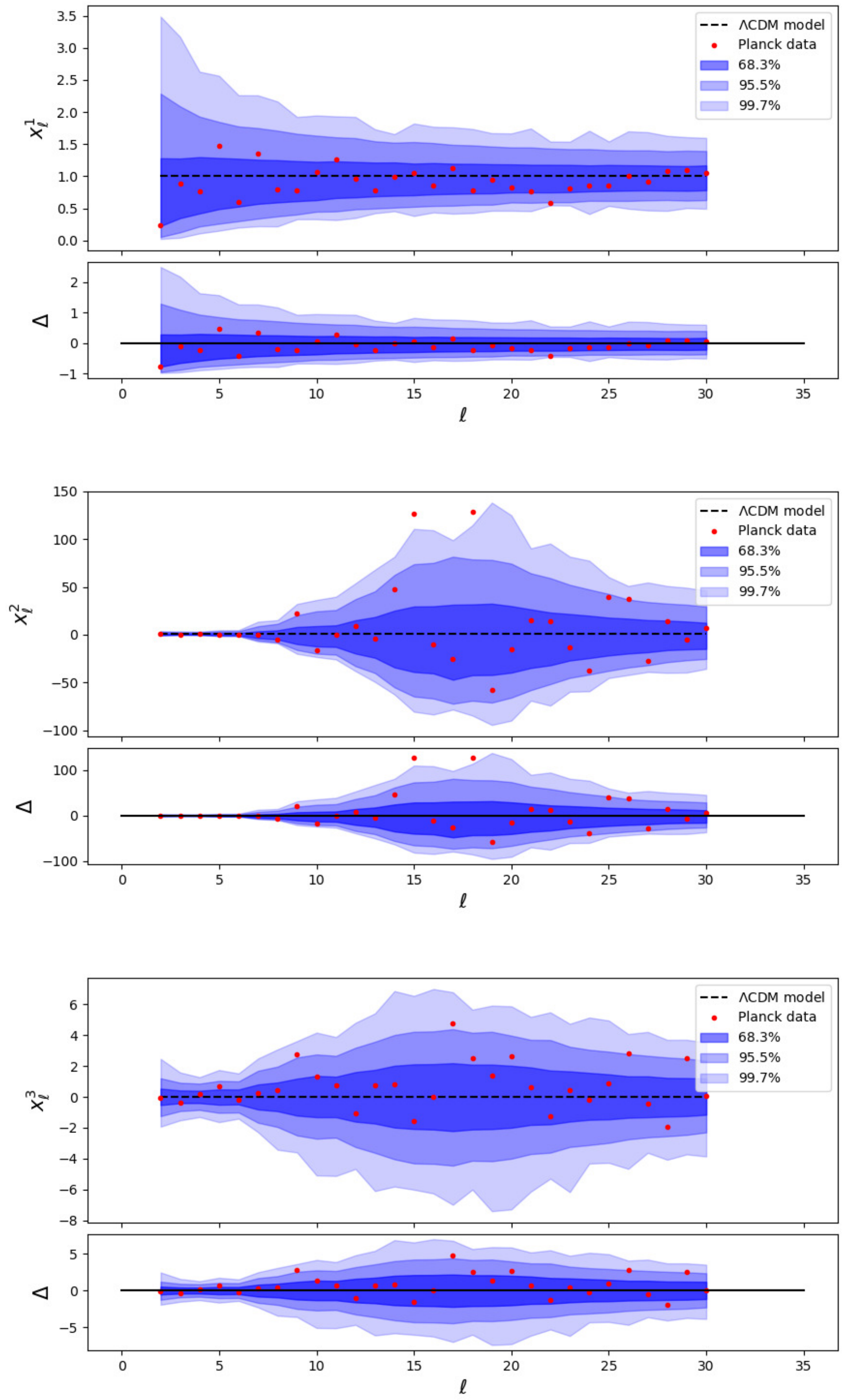

Figure 5.7: x_ℓ^1 (upper panel), x_ℓ^2 (middle panel) and x_ℓ^3 (lower panel) as a function of ℓ obtained from the PLANCK-WMAP low-ℓ data set. The blue shaded area is for the 68.3%, 95.5% and 99.7% confidence levels with respect to ΛCDM model, represented with the dashed horizontal ines. Each panel displays also a lower box where for each ℓ it is shown the distance of the estimates from the model.

As signal S can be used the expectation values A_ℓ^{th}, whereas as noise N the variance of the distribution of the realisations var_ℓ, defined as:

$$var_\ell = \frac{1}{N}\sum_{i=1}^{i=N}\left[(A_{\ell,i}^{sim} - A_\ell^{th})\right]^2 . \tag{5.5}$$

Thus the explicit form of the S/N is [4]:

$$\left(\frac{S}{N}\right)^2 = \sum_{\ell=2}^{\ell=30}\frac{\left(A_\ell^{th}\right)^2}{var_\ell}. \tag{5.6}$$

Through the statements of the S/N (eq. 5.6) we can understand if each multipole contributes to give more information or if after a while it saturates.

In Fig. 5.8 we show the S/N of D_ℓ^{TT} (upper panel), D_ℓ^{EE} (middle panel) and D_ℓ^{TE} (lower panel) as a function of ℓ. For the power band D_ℓ^{TT}, the S/N grows indefinitely for each ℓ, reaching the value of about 470 at $\ell = 30$. The S/N of D_ℓ^{EE} saturates round the multipoles $\ell = 9 - 10$, i.e. the spectrum is noise dominated after those multipoles. Extending the analysis at multipoles higher than these values would increase only the variance of the object without adding any information. Therefore, the analyses that involve, directly or indirectly, D_ℓ^{EE} are performed with $\ell_{max} = 10$. Finally, we note that the S/N of D_ℓ^{TE} does not saturate, it reachs the value of ~ 10 at $\ell = 30$; moreover its slope changes in correspondence of the multipoles where D_ℓ^{EE} saturates.

The S/N of x_ℓ^1 (upper panel) and x_ℓ^2 (lower panel) as a function of ℓ are displayed in Fig. 5.9. The S/N of x_ℓ^1 grows indefinitely for each ℓ (x_ℓ^1 depends only on the temperature). Instead the S/N of the x_ℓ^2, which is a function of the spectra C_ℓ^{TT}, C_ℓ^{EE} and C_ℓ^{TE}, saturates around the multipoles $\ell = 6 - 7$ (one could note that the values of multipole at which the S/N satures are slightly smaller than the ones corresponding to the spectra D_ℓ^{EE} and D_ℓ^{TE}). Therefore we have chosen to set $\ell_{max} = 6$ also in the analyses that involve, directly or indirectly, x_ℓ^2.

---

[4] In this way, in the noise is considered both the cosmic variance and the instrumental noise of the observations

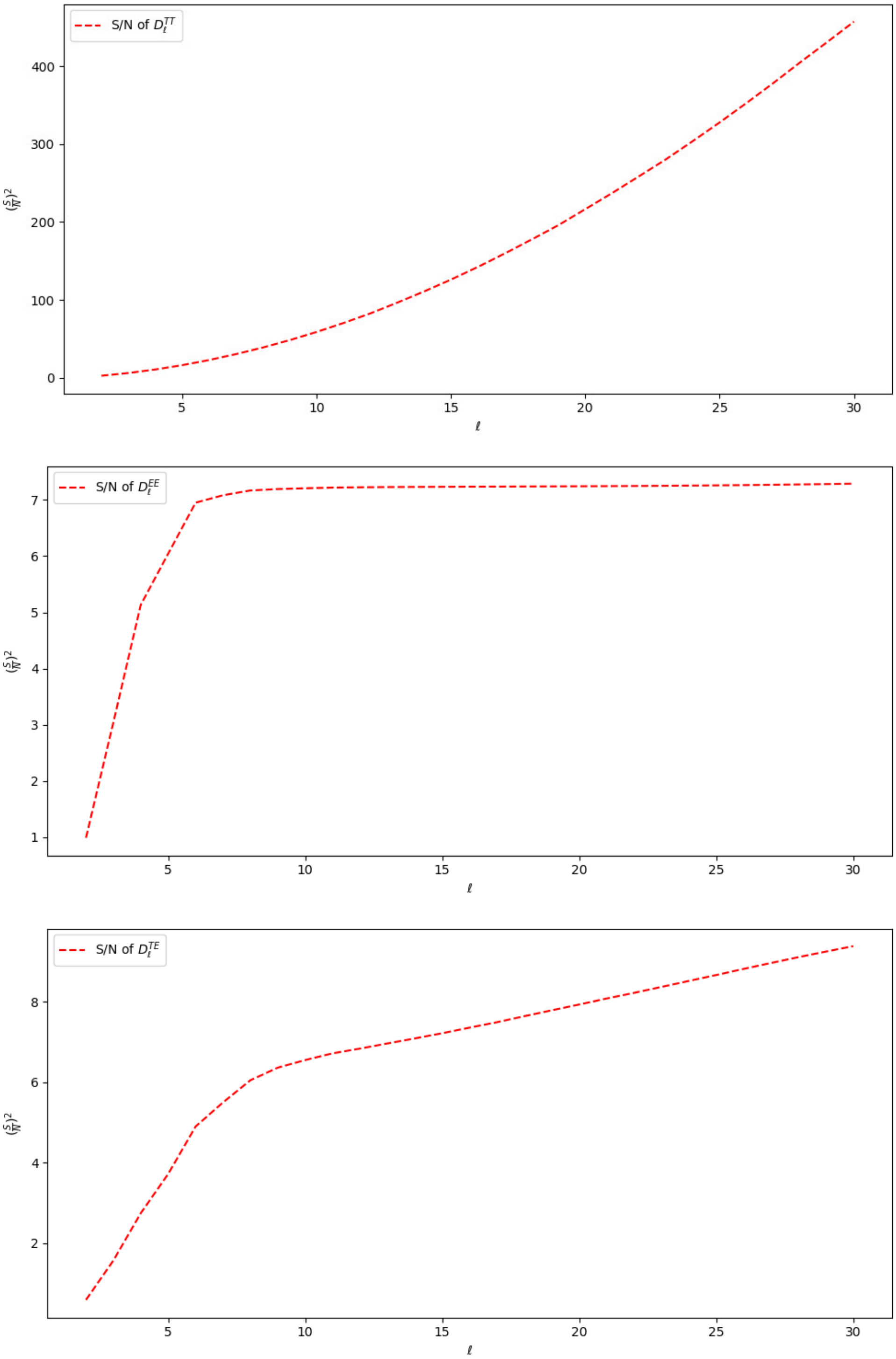

Figure 5.8: Signal-to-Noise ratio of D_ℓ^{TT} (upper panel), D_ℓ^{EE} (middle panel) and D_ℓ^{TE} (lower panel) as a function of ℓ. The S/N of D_ℓ^{TT} grows indefinitely for each ℓ. The S/N of D_ℓ^{EE} saturates around the multipoles $\ell = 8-9$, i.e. the spectrum is noise dominated after those multipoles. Instead the S/N of D_ℓ^{TE} does not saturate but changes its slope around the multipoles $\ell = 9 - 10$.

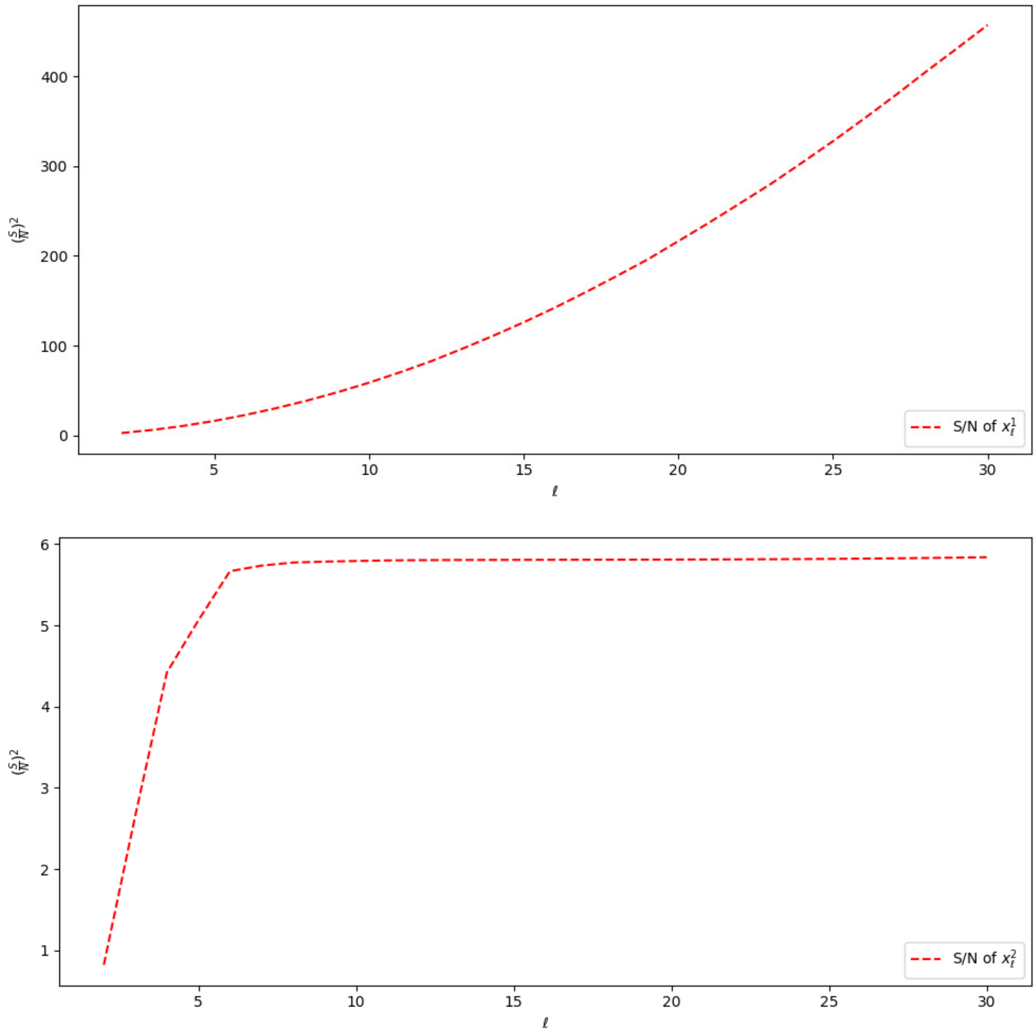

Figure 5.9: Signal-to-Noise ratio of x_ℓ^1 (upper panel) and x_ℓ^2 (lower panel) as a function of ℓ. The S/N of x_ℓ^1 grows indefinitely for each ℓ. The S/N of x_ℓ^2 saturates around the multipoles $\ell = 6 - 7$, i.e. the spectrum is noise dominated after those multipoles.

Chapter 6

Data Analysis and Results

In order to evaluate the lack of power at large angular scales considering also polarisation data, we propose two new estimators. The first one is based on the variance estimators which are then used to build a 2D-contour plot. The second estimator, which is the main novelty of this thesis, is obtained using the APS of Random Variables. This allows one to define easily a 1D-estimator which jointly contains all the information present in the TT, EE and TE spectra.

As usual, the comparison between simulations and Planck data was evaluated in terms of percentage of consistency.

6.1 2D-Variance in the space of pixels

The variances in the space of pixels in temperature and polarisation maps, for a realisation can be defined as[49]: [1]:

$$var^{TT} = C_2^{TT}(0) = \sum_{\ell=2}^{\ell_{max}} \frac{2\ell+1}{4\pi} C_\ell^{TT}, \tag{6.1}$$

$$var^{QQ} = C_2^{QQ}(0) = \sum_{\ell=2}^{\ell_{max}} \left[\frac{2\ell+1}{8\pi} (C_\ell^{EE} + C_\ell^{BB}) \right], \tag{6.2}$$

where ℓ_{max} is the highest multipole considered in the sum. Equation (6.1) describes the variance for the temperature map, while the (6.3) represents the variance of the polarisation map, including both the E-modes and B-modes.

These variances are then used to build a 2D-estimator, which, computed for all the simulations, generates a 2D-dimensional empirical distribution for each ℓ_{max}. Through a process of interpolation we can build a 2D-contour

---

[1] The analogous estimator of C_l^{TE} is null by construction[49].

plot that allows to compute the C.L. for the Planck data and forecasts for future observations.

First of all, we perform for both the variances the validation of the MC simulations which could be also consider as a “internal test” of the algorithm used to employed the variances, since the spectra C_ℓ are just been validated. Fig. 6.1, shows the average of var^{TT}, var^{QQ} as function of ℓ_{max} respectively in the upper and lower panels along with their uncertainties of the means σ_μ. Each panel displays also a lower box where for each ℓ_{max} it is shown the distance of mean in units of σ_μ. The analogous of the condition, see eq. (5.2), is satisfied.

Fig. 6.2 shows the comparison between simulations and Planck data for var^{TT} (upper panel), var^{QQ} (lower panel). Through the statistical analysis of the MC simulations it is possible to compute the confidence regions at the levels of 68.3%, 95.5% and 99.7% with respect to the ΛCDM model. Fig 6.2 shows that the data have a lack of power in temperature and polarisation respect the predictions of the ΛCDM model. It is important to note that var^{QQ} corresponding to the Planck data, after the multipole $\ell = 12 - 15$, deviates significantly from the model. These fluctuations are an effect of the noise in the spectrum C_ℓ^{BB} and in particular in the spectrum C_ℓ^{EE}, which becomes dominant after these multipoles. In fact we have seen that the S/N of the spectrum C_ℓ^{EE} saturates after about multipole $\ell = 9 - 10$. For this reason the variance of polarisation after $\ell = 10$ loses statistical importance and we have chosen to limit the analyses of the variances at $\ell_{max} = 10$.

6.1.1 1D-Variances

The panels in Fig. 6.3 display the empirical distributions of var^{TT} (upper panel) and of var^{QQ} (lower panel), for $\ell_{max} = 10$, with the Planck Data and the confidence levels at the 68.3%, 95.5% and 99.7% with respect to ΛCDM.

Both the variances corresponding to the Planck data are included in the 68% confidence level. We evaluate this behavior computing the Lower Tail Probability (LTP). In the first two rows of Table 6.1 (below) are reported the confidence level C.L. and the LTP for var^{TT}, var^{QQ}.

6.1.2 2D-Variance

We employ a 2D-variance estimator to join the informations of the temperature and the polarisation, evaluating the consistency between ΛCDM model and Planck data in terms of probability in the 2D-space of variances. The 3D-histogram in the space (var^{TT},var^{QQ}), Fig. 6.4, shows the empirical distribution of the simulations of this 2D-estimator for $\ell_{max} = 10$. The contours

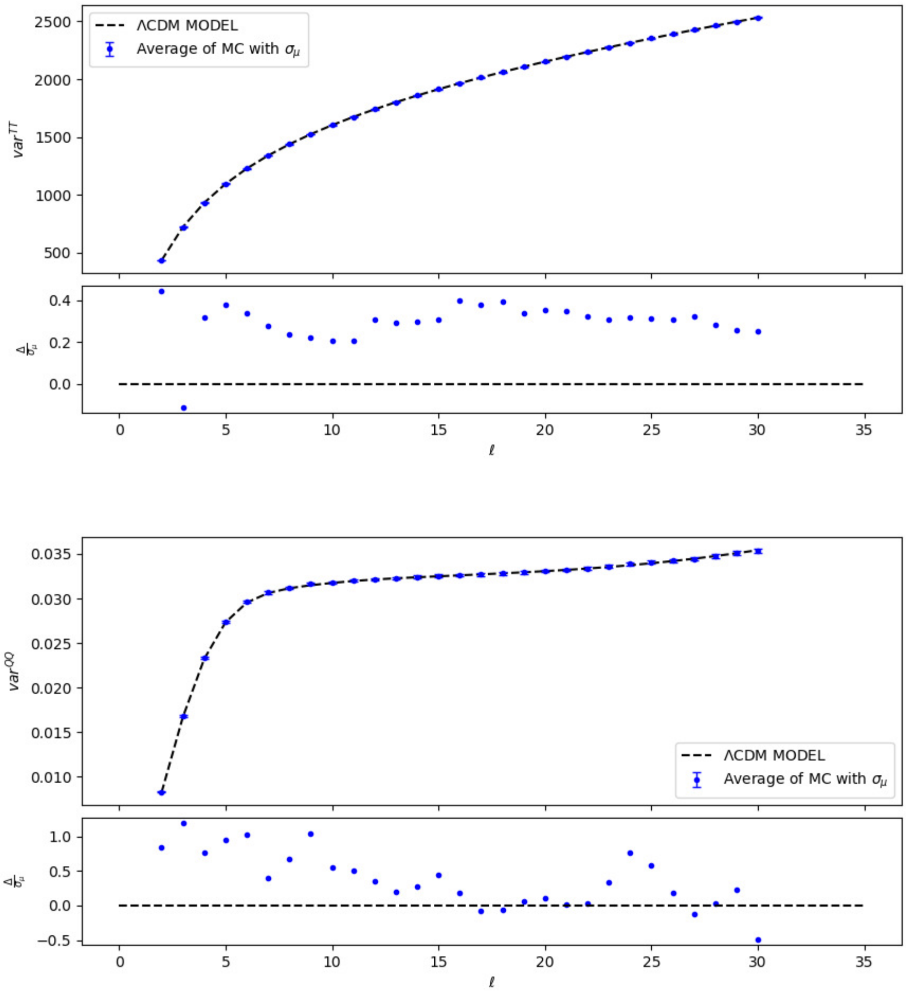

Figure 6.1: Averages of var^{TT} (upper panel), var^{QQ} (lower panel) as a function of ℓ_{max} obtained from MonteCarlo simulations corresponding to the PLANCK-WMAP low-ℓ data. Blue error bars represent the uncertainties associated to the averages. Each panel displays also a lower box where for each ℓ_{max} it is shown the distance of mean in units of σ_μ. Dashed black lines represent what theoretically expected for var^{TT} (upper panel), var^{QQ} (lower panel). We do not expected a scatter plots with mean null because these residuals are correlated

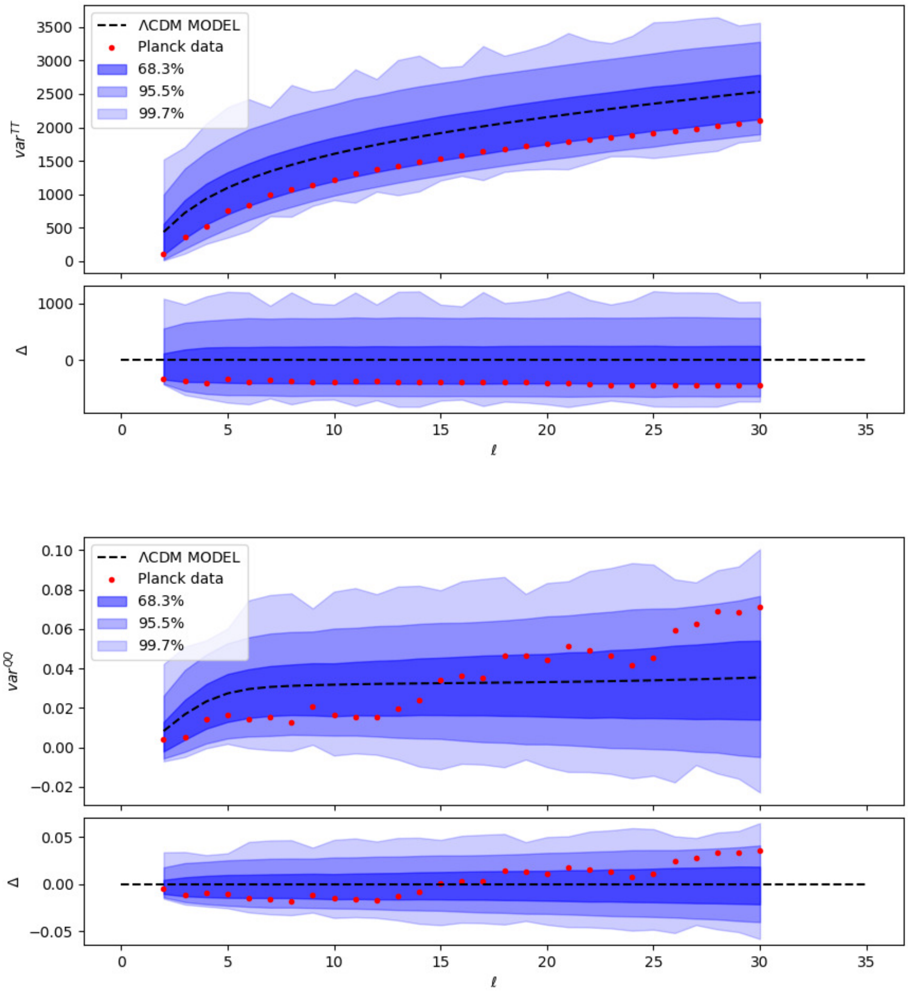

Figure 6.2: var^{TT} (upper panel), var^{QQ} (lower panel) as a function of ℓ_{max} obtained from the Planck-WMAP low-ℓ data set. The blue shaded area is for the 68.3%, 95.5% and 99.7% confidence levels with respect to ΛCDM model, represented with the dashed horizontal lines. Each panel displays also a lower box where for each ℓ it is shown the distance of the estimates from the model.

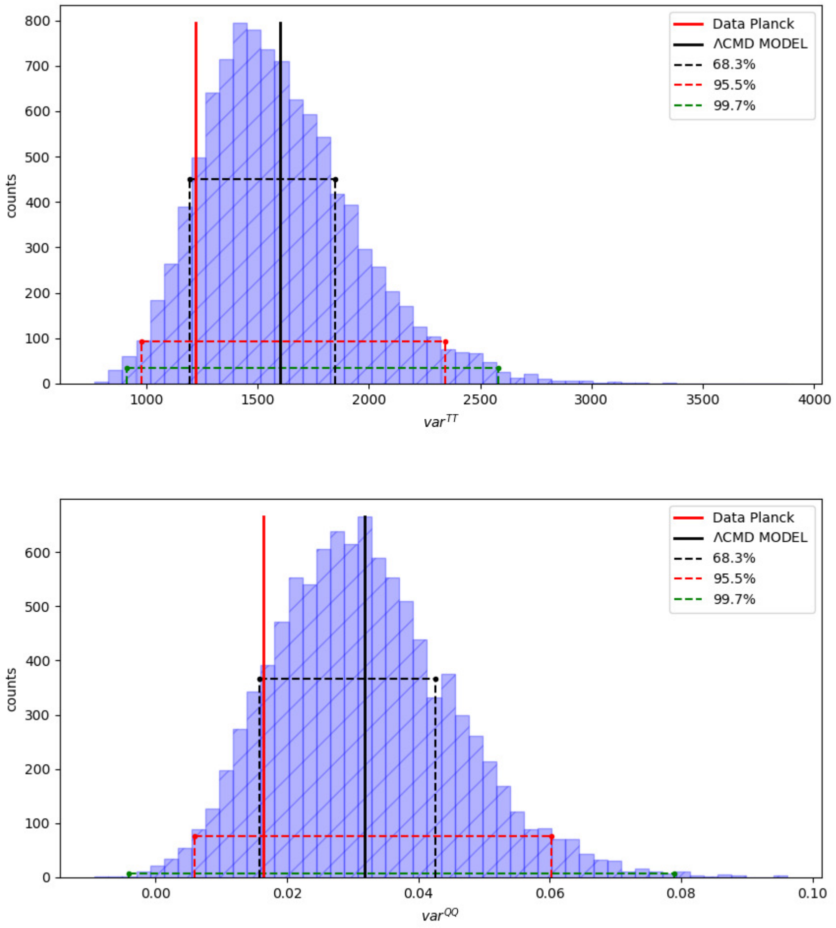

Figure 6.3: Histograms of var^{TT} (upper panel) and var^{QQ} (lower panel) with $\ell_{max} = 10$. The red line indicates the Planck Data, whereas the dashed black line the ΛCDM Model. The blue, yellow and green lines indicate respectively the boundaries of the 68.3%, 95.5% and 99.7% confidence regions.

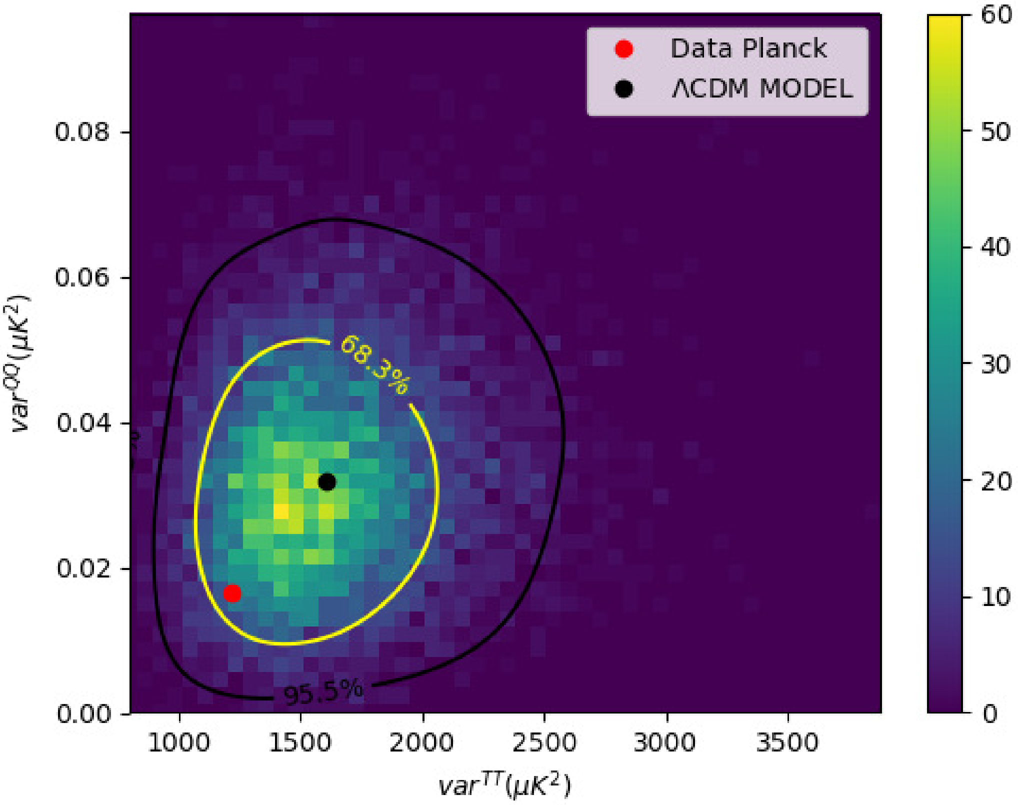

Figure 6.4: 3D-Histogram, encoded through the color map shown at the right, of the 2D variance for $\ell_{max} = 10$. The contours in the plane represent the 68.3% and 95, 5% regions. The red and the black points are the values for the Planck data and for the ΛCDM model.

in the histogram identify the 68.3% (in yellow) and the $95,5\%$ (in black) regions. [2]

The 2D-variance of the Planck data are always included in 68% but the joint LTP decreases at 2.01%. This does mean that the probability to obtain a variance as low as the data considering jointly the temperature and the polarisation is lower by a factor ~ 6 than the probability obtained by considering only the temperature or only the polarisation. The comparison between the result obtained for var^{TT}, var^{QQ} and for the 2D-variance is reported in Table 6.1. While it is interesting to note such a decrease, we wish to clear that such a percentage cannot be considered as anomalous.

Estimator	C.L.	LTP
var^{TT}	$< 68.3\%$	11.97%
var^{QQ}	$< 68.3\%$	12.26%
$2D - var$	$< 68.3\%$	2.01%

Table 6.1: Comparison in term of LTP and C.L. of the Planck data between var^{TT}, var^{QQ} and the 2D-variance.

6.1.3 2D-variance including only variance of the E-modes

Consistently with the ΛCDM model, we consider MC simulations with null B-modes. Therefore, in the variance estimator var^{QQ}, the contribution from C_ℓ^{BB} is only of instrumental noise. In order to evaluate this effect on the behavior of the 2D-variance, we consider a slightly different estimator, called 2D-var_{EE}, obtained considering, instead of var^{QQ}, a variance estimator that considers the E-modes only:

$$var^{EE} = \sum_{\ell=2}^{\ell_{max}} \left[\frac{2\ell+1}{8\pi} C_\ell^{EE} \right] . \tag{6.3}$$

Fig 6.5 shows the contour plot obtained for 2D-var_{EE} at $\ell_{max} = 10$. To evaluate quantitatively the difference with respect to the 2D-variance proposed in the previous section, we compute the areas included within the 68.3% and 95.5% C.L. for the 2D variance and for 2D-var_{EE} at $\ell_{max} = 10$

---

[2] considering only 10^4 realisations the contours of the region at 99.7% is fragmented and irregular, to compute adequately the region at 99.7% should be necessary at least 10^5 realisations.

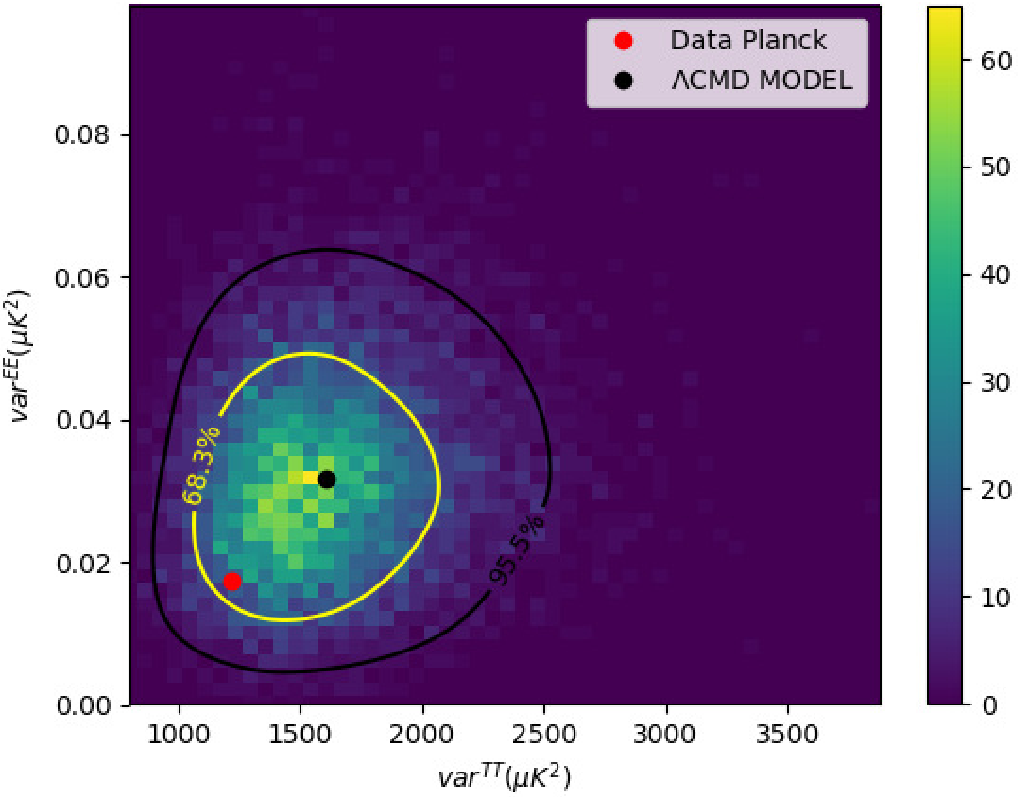

Figure 6.5: 3D-Histogram of the 2D-var_{EE} for $\ell_{max} = 10$, the color scale is given on the right. The yellow and black countours in the plane represent the 68.3% and $95,5\%$ regions, respectively. The red and the black points are the values for the Planck data and for the ΛCDM model, respectively.

and evaluate the ratios between them. We obtain a factor of ~ 1.07 for both the ratios. Hence, the impact of BB noise contribution on this estimator turns out be not very strong.

6.2 Estimator based on APS of Random Variables

6.2.1 Dimensionless Normalised Mean Power

In the chapter 4 we have shown that the APS of Random Variables x_ℓ^1, x_ℓ^2 and x_ℓ^3 can be combined to define an 1D-estimator which depends on temperature, E-mode polarisation and their cross-correlation: the dimensionless normalised mean power P:

$$P = \frac{1}{(\ell_{max}-1)} \sum_{\ell=2}^{\ell_{max}} (x_\ell^1 + x_\ell^2) \,, \tag{6.4}$$

Note that a definition of the following type:

$$S = \frac{1}{(\ell_{max}-1)} \sum_{\ell=2}^{\ell_{max}} (x_\ell^1 + x_\ell^2 + x_\ell^3) \,, \tag{6.5}$$

is expected to have less signal-to-noise ratio with respect to P because while the two estimators have the same expectation value, i.e. $\langle P \rangle = \langle S \rangle = 2$, the intrinsic variance of P is in general smaller than the one of S.

For sake of simplicity we can rewrite the estimator P as:

$$P = \bar{x}^1_{\ell_{max}} + \bar{x}^2_{\ell_{max}} \,, \tag{6.6}$$

where:

$$\bar{x}^1_{\ell_{max}} = \frac{1}{(\ell_{max}-1)} \sum_{\ell=2}^{\ell_{max}} x_\ell^1, \tag{6.7}$$

$$\bar{x}^2_{\ell_{max}} = \frac{1}{(\ell_{max}-1)} \sum_{\ell=2}^{\ell_{max}} x_\ell^2. \tag{6.8}$$

Fig. 6.6 shows the comparison between data and simulations using the estimators $\bar{x}^1_{\ell_{max}}$ (upper panel), $\bar{x}^2_{\ell_{max}}$ (middle panel) and P (lower panel) as function of the ℓ.

In the panel of the estimator $\bar{x}^2_{\ell_{max}}$ and P, one can see how the S/N of the APS of Random Variable x_ℓ^2 produces a systematic trend in the data and

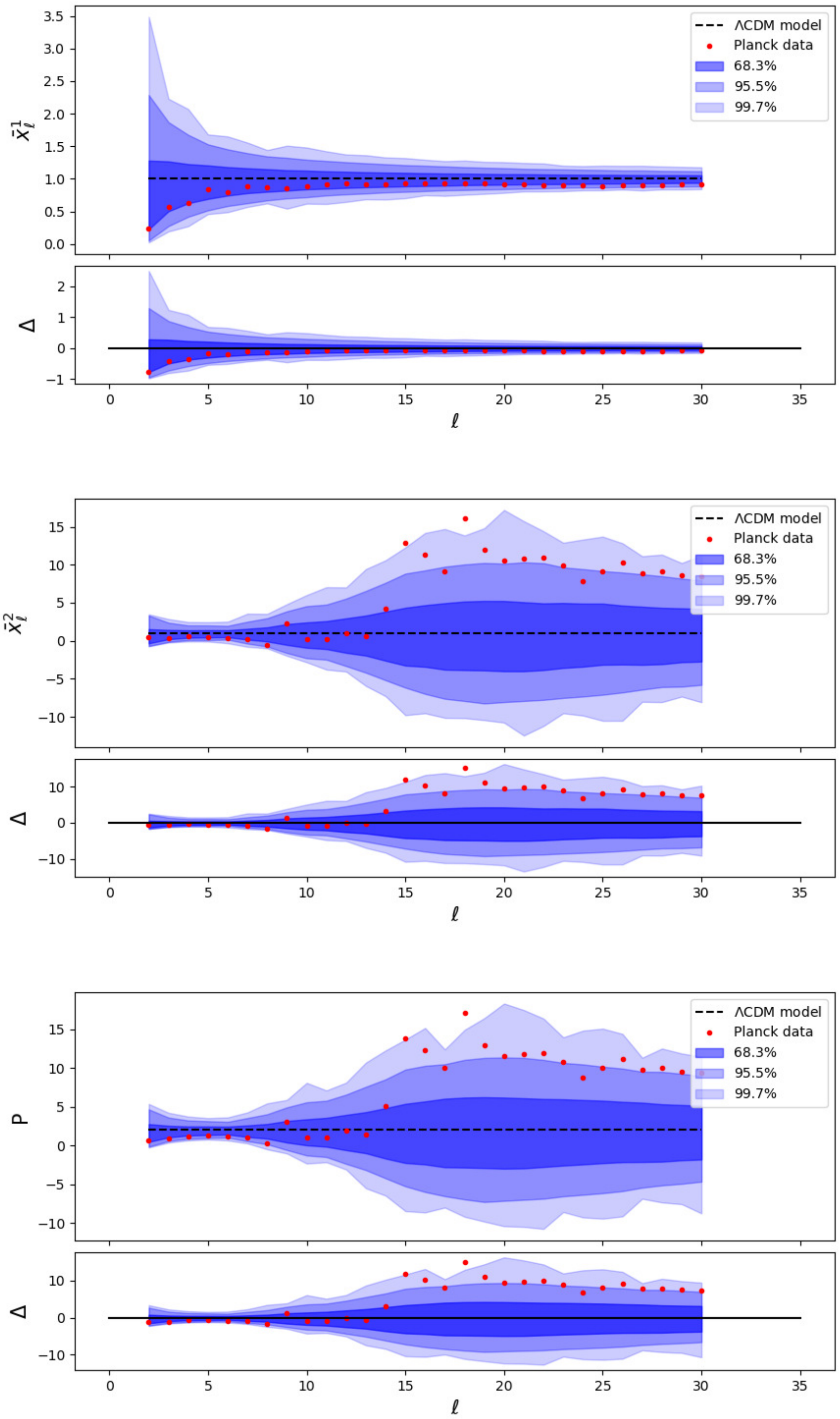

Figure 6.6: $\bar{x}^1_{\ell_{max}}$ (upper panel), $\bar{x}^2_{\ell_{max}}$ (middle panel) and P (lower panel) as a function of ℓ_{max} obtained from the PLANCK-WMAP low-ℓ data set. The blue shaded area is for the 68.3%, 95.5% and 99.7% confidence levels with respect to ΛCDM model, represented by the dashed horizontal lines. Each panel displays also a lower box where for each ℓ it is shown the distance of the estimates from the model.

a huge widening in the C.L. after the multipole $\sim 6-7$. For this reason the analysis of this estimator P is limited at the first multipoles, in particular we have chosen $\ell_{max} = 6$. The distribution of the realisations for the estimator P at $\ell_{max} = 6$ is reported in Fig. 6.7, which also shows the value corresponding to the Planck data (red solid line) and the confidence levels at 68.3%, 95.5% and 99.7% with respect to ΛCDM.

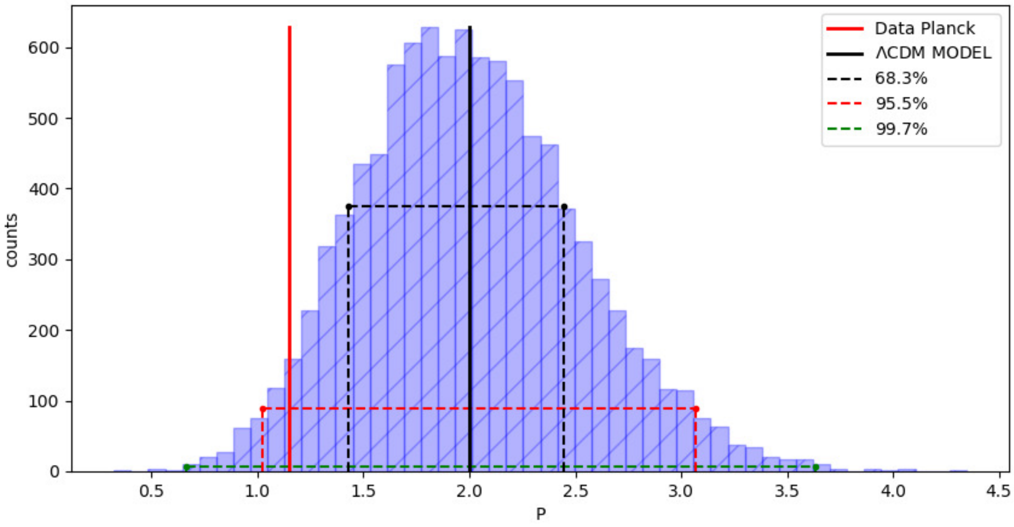

Figure 6.7: Empirical distribution of the P estimator for $\ell_{max} = 6$.The red and the black vertical lines represent the values of the Planck data and of the ΛCDM model respectively. The blue, yellow and green lines indicate the boundaries of the 68.3%, 95.5% and 99.7% confidence regions respectively.

In Table 6.2 we report the comparison of the C.L. and the LTP between the P estimator and the $\bar{x}^1_{\ell_{max}}$, $\bar{x}^2_{\ell_{max}}$ for $\ell_{max} = 6$.

Estimator	C.L.	LTP
P	$< 95.5\%$	3.63%
$\bar{x}^1_{\ell_{max}}$	$< 68.3\%$	17.63%
$\bar{x}^2_{\ell_{max}}$	$< 95.5\%$	6.71%

Table 6.2: Comparison in terms of LTP and C.L. of the Planck data between P and $\bar{x}^1_{\ell_{max}}$, $\bar{x}^2_{\ell_{max}}$ for $\ell_{max} = 6$.

We note, from the Fig. 6.7 and from the Table 6.2, an increase of the statistical significance when temperature and polarisation are jointly considered, in fact:

- using the P estimator, the value of the Planck data is included in the 95.5% C.L., whereas it is included in the 68.3% C.L. when only the temperature is taken into account ($\bar{x}^1_{\ell_{max}}$ estimator);
- the LTP provided by the P estimator is much lower than the LTP obtained by considering separately the temperature and the polarisation ($\bar{x}^1_{\ell_{max}}$ and $\bar{x}^2_{\ell_{max}}$ estimators).

Despite the improvement this behavior cannot be still considered completely anomalous.

These results are fully compatible with those obtained from the study of the 2D-variance, however the benefits of using P is that it is a 1D-estimator and so is more immediate and simple to characterise it qualitatively and quantitatively

6.2.2 Optimised Dimensionless Normalised Mean Power

The P estimator is a particular case of a more general estimator $\tilde{P}$:

$$\tilde{P} = \alpha\bar{x}^1_\ell + \beta\bar{x}^2_\ell, \tag{6.9}$$

with $\alpha = \beta = 1$, i.e. in P temperature and polarisation contribution have the same weight. The objects $\bar{x}^1_\ell$ and $\bar{x}^2_\ell$ have the same expectation value ($\langle\bar{x}^1_\ell\rangle = \langle\bar{x}^2_\ell\rangle = 1$) but a different intrinsic variance. Thus one can interpret the estimator P as the specific dimensionless normalised mean power built giving importance to the part of signal (i.e. the expectation value) of $\bar{x}^1_\ell$ and $\bar{x}^2_\ell$, ignoring the fact that the intrinsic variances of $\bar{x}^1_\ell$ ($var(\bar{x}^1_\ell)$) and $\bar{x}^2_\ell$ ($var(\bar{x}^2_\ell)$) are different.

Now we want to build an estimator $\tilde{P}$ with the best signal-to-noise ratio, i.e. the smallest intrinsic variance (since $\bar{x}^1_\ell$ and $\bar{x}^2_\ell$ have the same signal and we identify the noise with the variance). We apply the method of the Lagrange multipliers, we minimize $var(\tilde{P})$ on the constraint:

$$\langle\tilde{P}\rangle = \alpha\langle\bar{x}^1_\ell\rangle + \beta\langle\bar{x}^2_\ell\rangle = \alpha + \beta = const = 2, \tag{6.10}$$

where α and β are constant. The choice of the value for the constant is totally arbitrary, setting $const = 2$ allows to make the comparison between P and $\tilde{P}$.

The variance $var(\tilde{P})$ is defined as:

$$\begin{aligned} var(\tilde{P}) &\equiv \langle(\tilde{P} - \langle\tilde{P}\rangle)^2\rangle = \langle(\tilde{P})^2\rangle - \langle\tilde{P}\rangle^2 = \\ &= \alpha^2 var(\bar{x}^1_\ell) + \beta^2 var(\bar{x}^2_\ell) + 2\alpha\beta cov(\bar{x}^1_\ell, \bar{x}^2_\ell), \end{aligned} \tag{6.11}$$

where $var(\bar{x}^1_\ell)$ and $var(\bar{x}^2_\ell)$ are respectively the intrinsic variance of $\bar{x}^1_\ell$ and $\bar{x}^2_\ell$, and $cov(\bar{x}^1_\ell, \bar{x}^2_\ell)$ is their covariance:

$$cov(\bar{x}^1_\ell, \bar{x}^2_\ell) = \langle(\bar{x}^1_\ell - \langle\bar{x}^1_\ell\rangle)(\bar{x}^1_\ell - \langle\bar{x}^2_\ell\rangle)\rangle. \tag{6.12}$$

We introduce a new variable λ, which is the Lagrange multiplier, and minimise the function $f(\alpha, \beta, \lambda)$:

$$f(\alpha, \beta, \lambda) = var(\tilde{P}) + \lambda(\alpha + \beta - 2). \tag{6.13}$$

The minimum of the function $f(\alpha, \beta, \lambda)$ provides the values α and β for which $var(\tilde{P})$ is a minimum on the constraint $\alpha + \beta = 2$:

$$\frac{\partial f(\alpha, \beta, \lambda)}{\partial \alpha} = 2\alpha var(\bar{x}^1_\ell) + 2\beta cov(\bar{x}^1_\ell, \bar{x}^2_\ell) + \lambda = 0, \tag{6.14}$$

$$\frac{\partial f(\alpha, \beta, \lambda)}{\partial \beta} = 2\beta var(\bar{x}^2_\ell) + 2\alpha cov(\bar{x}^1_\ell, \bar{x}^2_\ell) + \lambda = 0, \tag{6.15}$$

$$\frac{\partial f(\alpha, \beta, \lambda)}{\partial \lambda} = \alpha + \beta - 2 = 0. \tag{6.16}$$

Solving this set of equations one can find the values of α and β:

$$\alpha = 2\frac{var(\bar{x}^2_\ell) - cov(\bar{x}^1_\ell, \bar{x}^2_\ell)}{var(\bar{x}^1_\ell) + var(\bar{x}^2_\ell) - 2cov(\bar{x}^1_\ell, \bar{x}^2_\ell)}, \tag{6.17}$$

$$\beta = 2\frac{var(\bar{x}^1_\ell) - cov(\bar{x}^1_\ell, \bar{x}^2_\ell)}{var(\bar{x}^1_\ell) + var(\bar{x}^2_\ell) - 2cov(\bar{x}^1_\ell, \bar{x}^2_\ell)}. \tag{6.18}$$

The analysis of the estimator $\tilde{P}$ is limited by the S/N of the APS of Random Variables in polarisation: greater is the ℓ_{max} and lesser becomes the coefficient of the polarisation β, i.e. increasing with the multipole ℓ the estimator to maintain the variance of $\tilde{P}$ as small as possible gives less importance to polarisation, see Fig. 6.8. After the multipole $\ell = 6$, the coefficient β decreased rapidly to zero. Therefore we find for $\ell_{max} = 6$:

$$\alpha = 1.64, \tag{6.19}$$

$$\beta = 0.36. \tag{6.20}$$

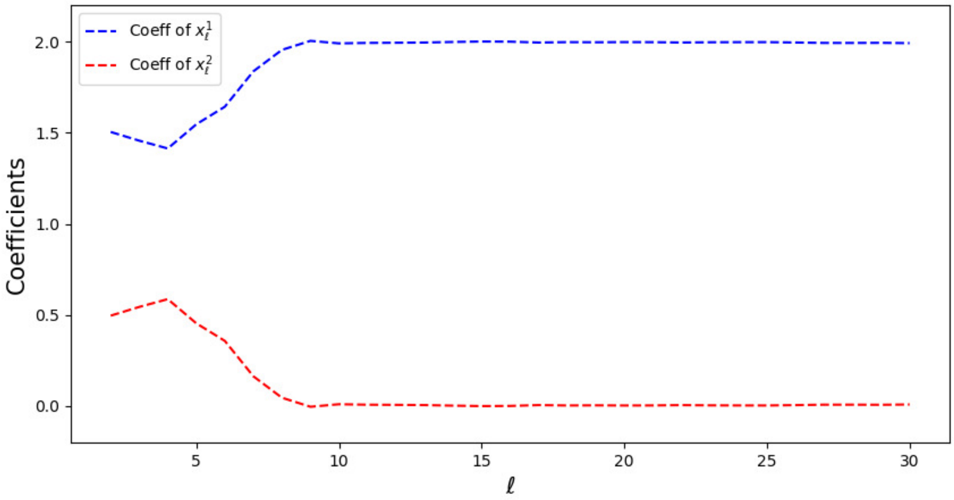

Figure 6.8: Coefficients α and β in the $\tilde{P}$ estimator as function of the ℓ_{max}. The coefficient β decreased rapidly to zero.

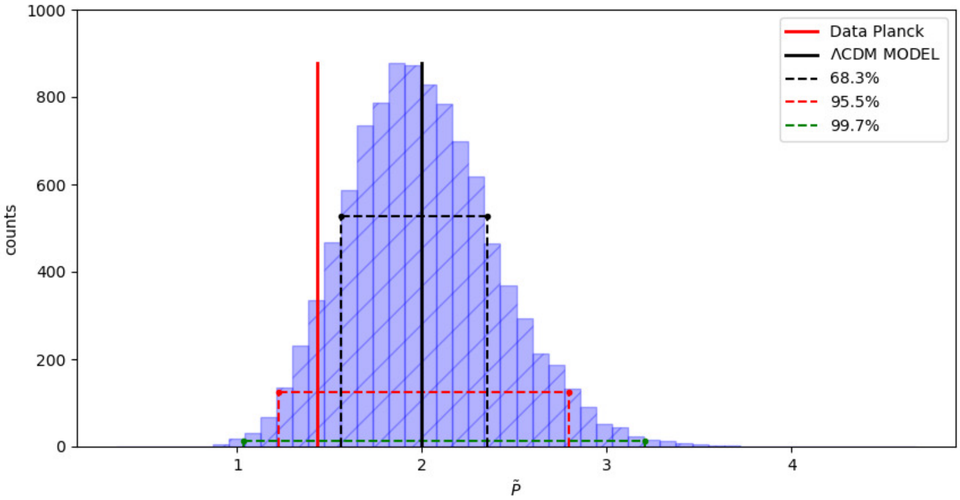

Figure 6.9: Empirical distribution of $\tilde{P}$ for $\ell_{max} = 6$.The red and the black vertical lines represent the values of the Planck data and of the ΛCDM model respectively. The blue, yellow and green lines indicate the boundaries of the 68.3%, 95.5% and 99.7% confidence regions respectively.

Fig. 6.9 shows the empirical distribution of the estimators $\tilde{P}$ for $\ell_{max} = 6$. This distribution is narrower than the distribution of P, in terms of the variance of the distribution we have an improvement by a factor of:

$$\frac{var(P)}{var(\tilde{P})} \simeq 1.69 \tag{6.21}$$

Also using the $\tilde{P}$ estimator, a lack of power of Planck data, is found with a LTP of:

$$LTP = 6.72\%. \tag{6.22}$$

The observed value is still in the left tail of the distribution, however the percentage is not completely anomalous.

Chapter 7

Forecasts

The CMB temperature anisotropies have been observed at the cosmic variance limit by Planck. Polarisation remains to be fully investigated: in particular, information in the E modes has not been fully extracted and the B modes, essential to detect the primordial gravitational waves, have not been observed (only upper limits have been provided) [5].

In this chapter we forecast the behavior of the proposed estimators (see Chapter 6, sections 6.1, 6.2), considering the instrumental noise of future CMB polarisation observations.[1] We take into account two different cases:

- LiteBird-like: this case is evaluated by scaling the polarisation noise of the Planck case by a factor 100;

- the cosmic variance limited (henceforth Ideal) case: this case is assessed making negligible the noise contribution.

As in the previous analysis, it has been followed a frequentist approach, considering 10000 realisations for each of these two cases.

7.1 Signal to Noise ratio

First of all we compare the behavior of the Signal-to-Noise ratio of D_ℓ in the Planck case with the aforementioned cases. Fig. 7.1, and Fig. 7.2 show respectively the Signal-to-Noise ratio of D_ℓ^{EE} and D_ℓ^{TE} as a function of ℓ for Planck (upper panel), LiteBird-like (middle panel) and Ideal (lower panel) CMB observations. The Signal-to-Noise ratio of D_ℓ^{EE} in the LiteBird-like

---

[1] At large angular scale the instrumental noise of Planck, for the observations in temperature, is so small that we can assume that the noise in temperature is already composed by only the cosmic variance, i.e. it is ideal.

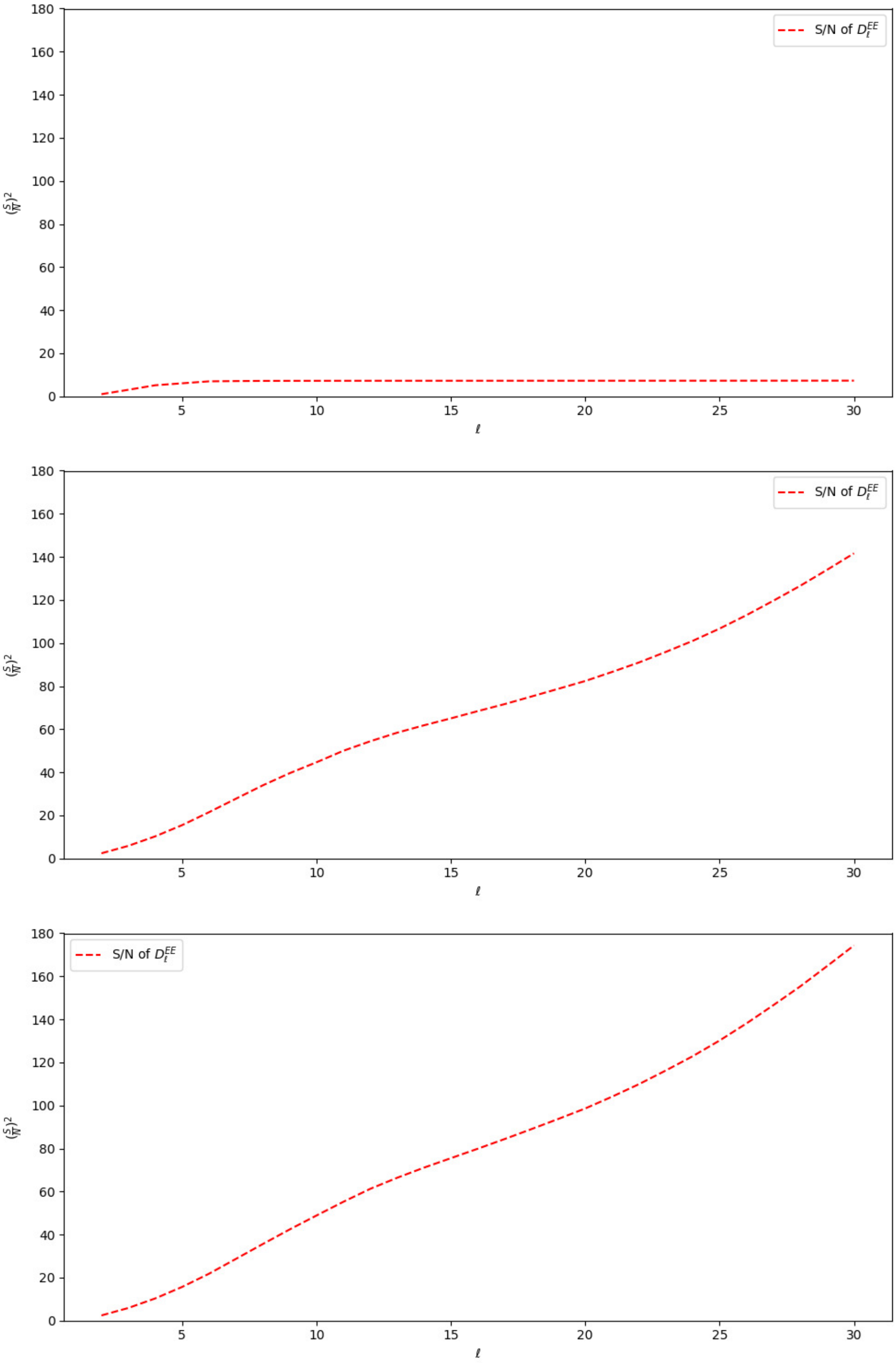

Figure 7.1: Signal-to-Noise ratio of D_ℓ^{EE} as a function of ℓ for the CMB observations with three different levels of Noise: Planck (first panel), LiteBird-like (second panel) and Ideal (third panel). For LiteBird-like and the Ideal cases the S/N grows indefinitely for each ℓ, whereas for Planck case the S/N saturates near the multipoles $\ell = 10$ reaching only a value smaller of one order of magnitude.

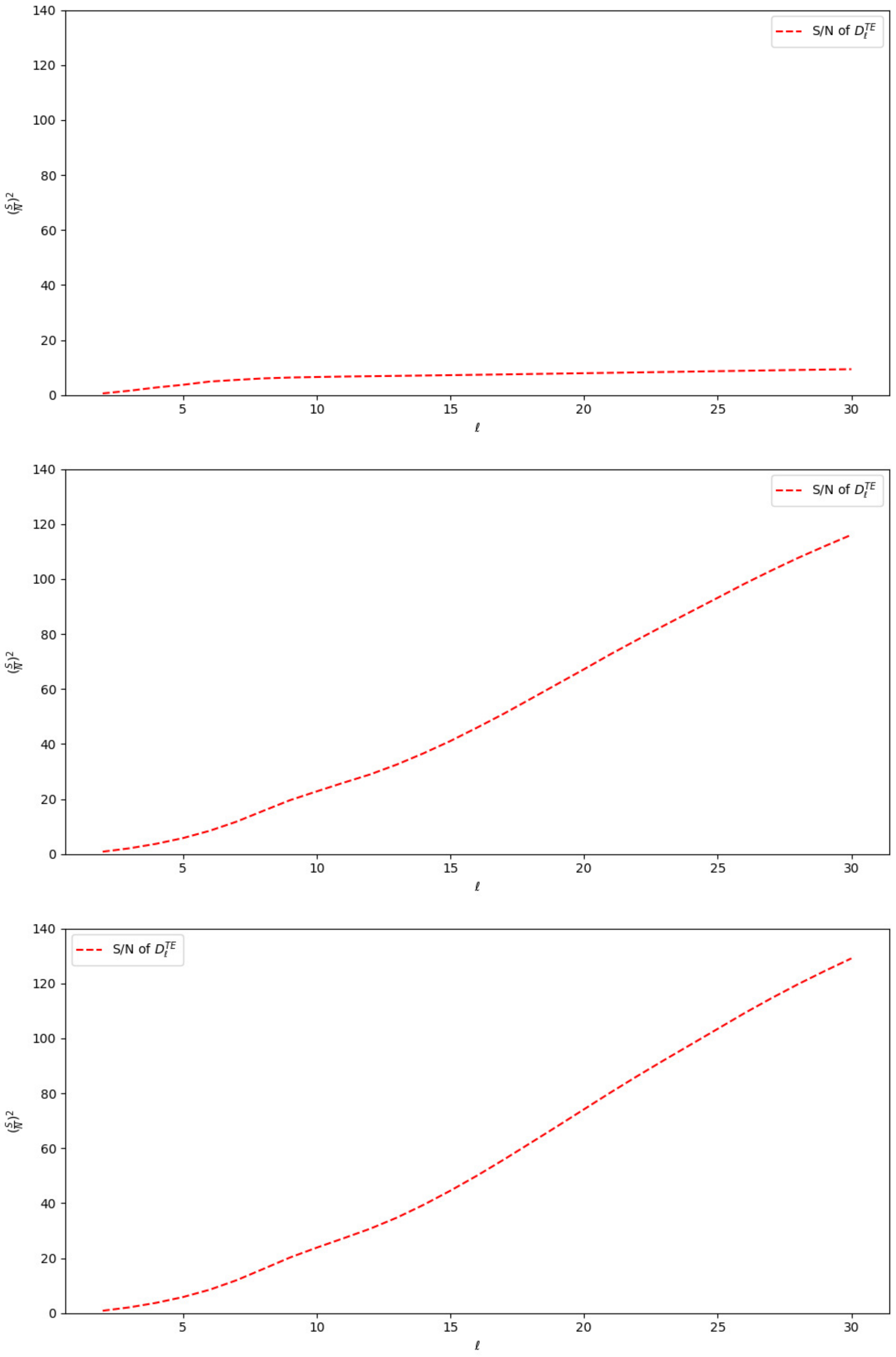

Figure 7.2: Signal-to-Noise ratio of D_ℓ^{TE} as a function of ℓ for the CMB observations with three different levels of Noise: Planck (first panel), LiteBird-like (second panel) and Ideal (third panel). For LiteBird-like and the Ideal cases the S/N grows indefinitely for each ℓ, whereas for Planck case the S/N, although does not saturate, reaches only a value smaller of one order of magnitude.

case (although smaller than the value obtained in the Ideal case) does not saturate as instead it happens in the Planck case. This allows to extend the analyses, which involve D_ℓ^{EE}, up to $\ell = 30$. Moreover the S/N of D_ℓ^{EE} and D_ℓ^{TE} reaches values that are one order of magnitude larger than what found in the Planck case.

In Table 7.1 we report some values of the S/N of D_ℓ^{EE} for the three cases at three different maximum multipoles. One can note the really large improvement between the LiteBird and Planck observations although LiteBird has not yet reached the ideal level.

ℓ	Planck Noise	LiteBird-like-Noise	Ideal-Noise
5	6.04	15.46	15.65
10	7.21	44.64	48.85
25	7.26	106.70	130.17

Table 7.1: Example of Signal-to-Noise ratio of D_ℓ^{EE} for the CMB observations with three different levels of Noise: Planck, LiteBird-like and Ideal cases.

We find an analogous behavior if we consider, see Fig. 7.3, the S/N as a function of ℓ of the APS of Random Variable x_ℓ^2 for Planck (first panel), LiteBird-like (second panel) and Ideal (third panel) CMB.

We also note that, although the improvement shown in this forecast, the S/N of the polarisation data (even in the Ideal case) does not reach the value obtained with the temperature data (see D_ℓ^{TT} and x_ℓ^1 in Fig. 7.4). This means that the information contained in E-mode, although important, will never overtake the one contained in the T-mode.

7.2 Angular Power Spectra and APS of Random Variables

The improvement of the S/N makes the distributions of the spectra D_l^{EE}, D_l^{TE}, D_l^{BB} and of the APS of Random Variables x_ℓ^2 and x_ℓ^3 for the LiteBird-Like and Ideal cases narrower than the distributions for Planck simulations. Fig. 7.5, Fig. 7.6 and Fig. 7.7 show the comparison of between the Planck (upper panel), LiteBird-Like (middle panel) and Ideal (lower panel) cases of D_l^{EE},D_l^{TE},D_l^{BB} respectively. At low multipoles we obtained a weak improvement in terms of widht of the distributions because at those scales the noise is already subdominant. At larger ℓ, where the noise contribution become more important, we observe a larger effect.

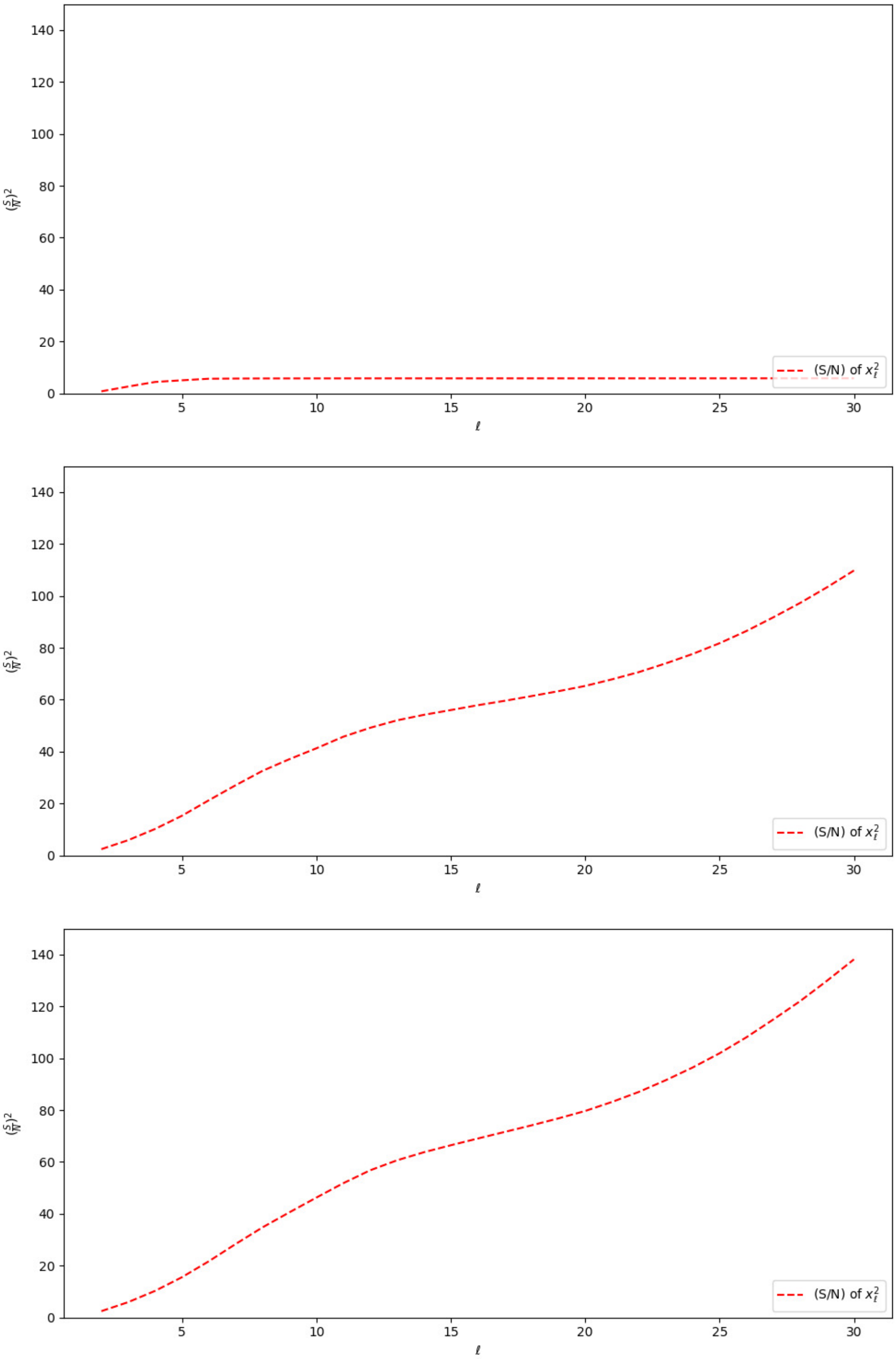

Figure 7.3: Signal-to-Noise ratio of x_ℓ^2 as a function of ℓ for the CMB observations with three different levels of Noise: Planck (first panel), LiteBird-like (second panel) and Ideal (third panel) cases. For LiteBird-like and the Ideal cases the S/N grows indefinitely for each ℓ, whereas for Planck the S/N saturates near the multipoles $\ell = 7$ reaching only a value smaller of one order of magnitude.

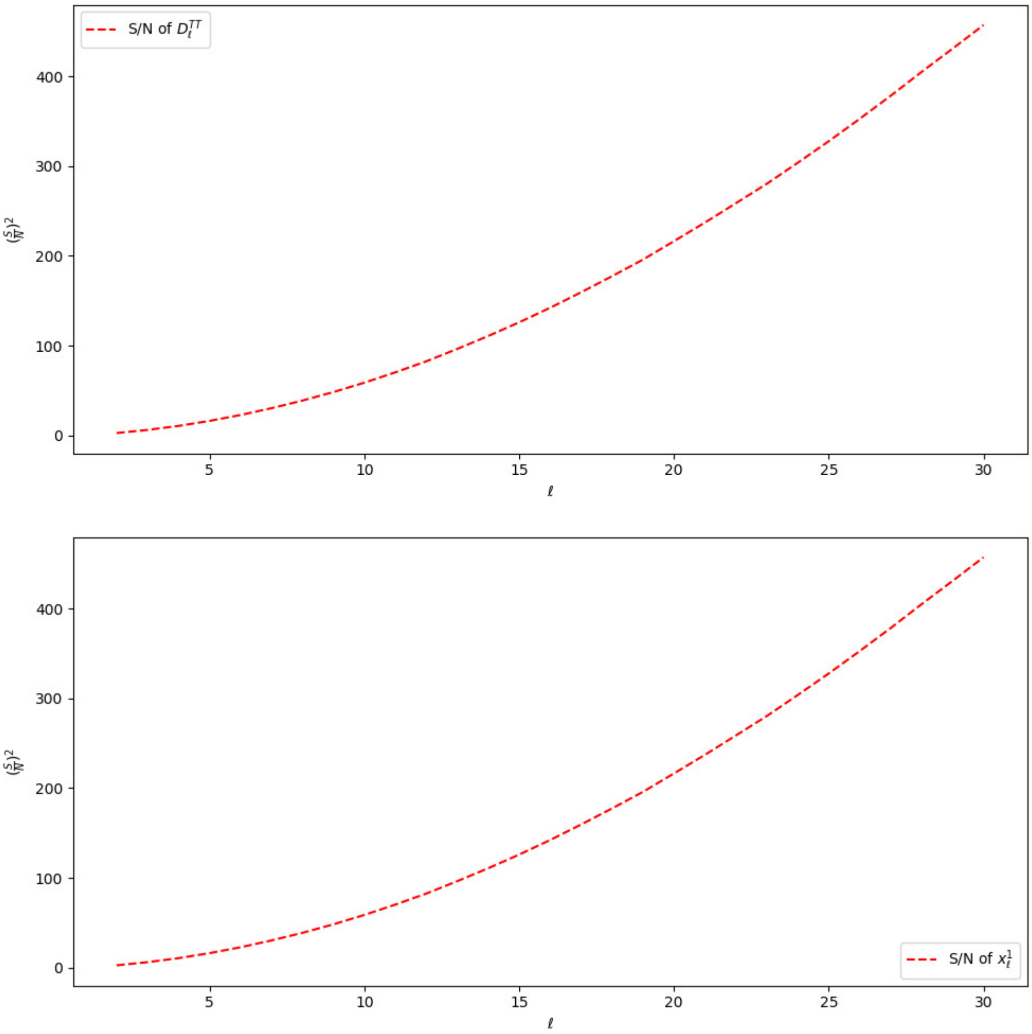

Figure 7.4: Signal-to-Noise ratio of D_ℓ^{TT} (upper panel), and x_ℓ^1 (lower panel). The S/N of D_ℓ^{TT} and x_ℓ^1 grows indefinitely for each ℓ, reaching values larger than 400.

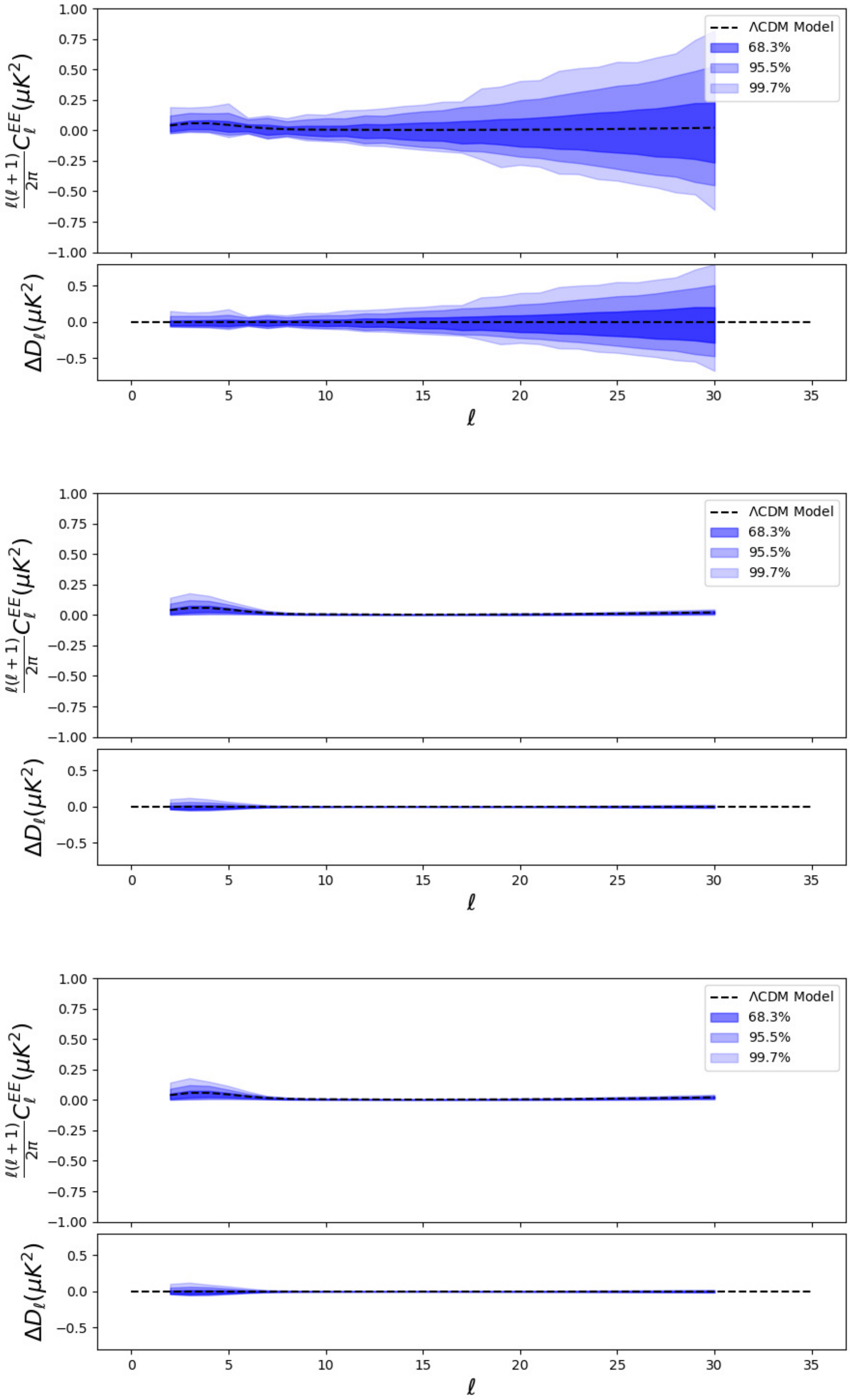

Figure 7.5: Comparison of D_ℓ^{EE} as a function of ℓ obtained for Planck (upper panel), LiteBird-Like (middle panel) and Ideal (lower panel) observations. The blue shaded area is for the 68.3%, 95.5% and 99.7% confidence levels with respect to ΛCDM model, represented by the dashed horizontal lines. Each panel displays also a lower box where for each ℓ it is shown the distance of the estimates from the model. The confidence regions of LiteBird-Like and Ideal observations are really narrower than the ones in the Planck case.

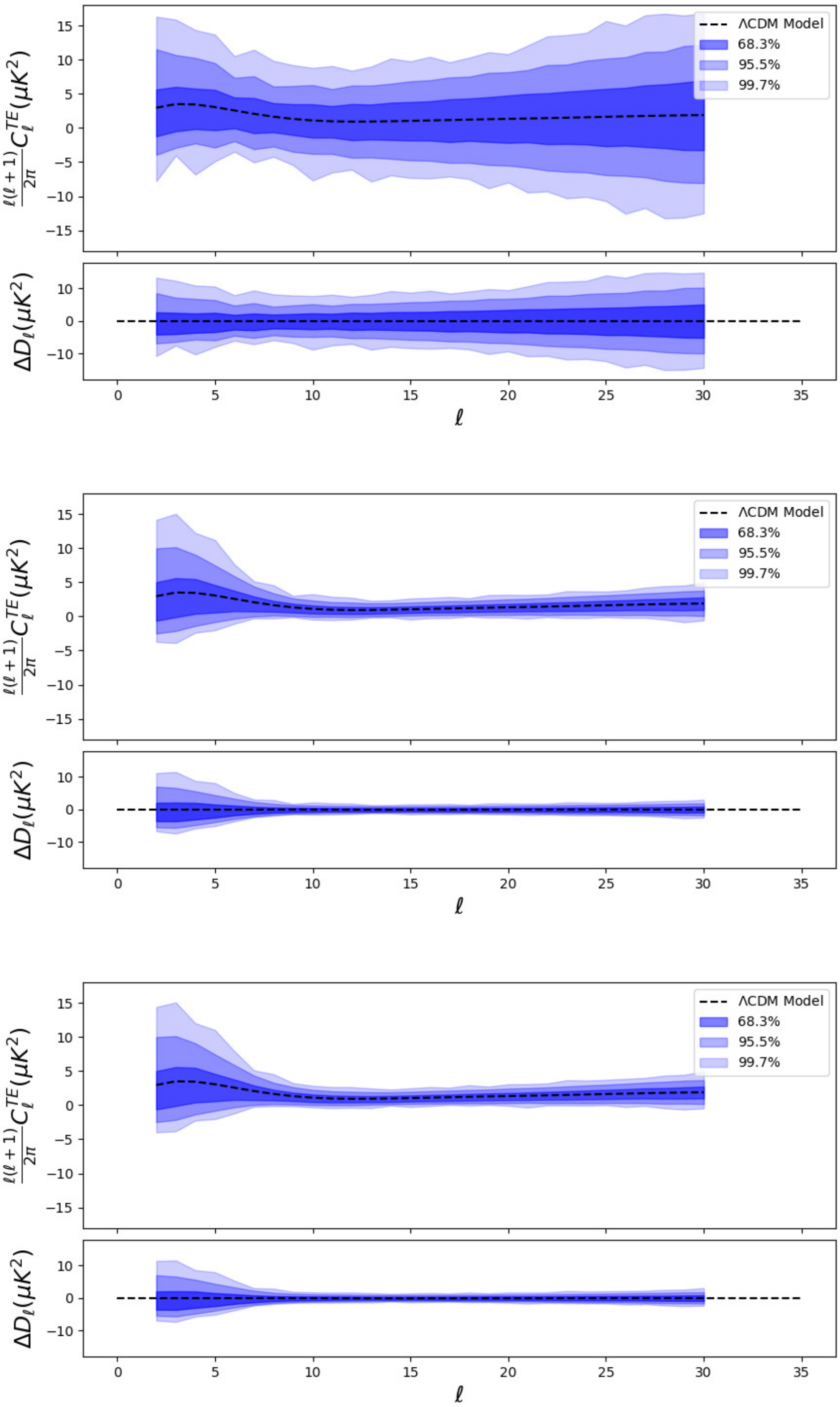

Figure 7.6: As Fig. 7.5, but for D_ℓ^{TE}.

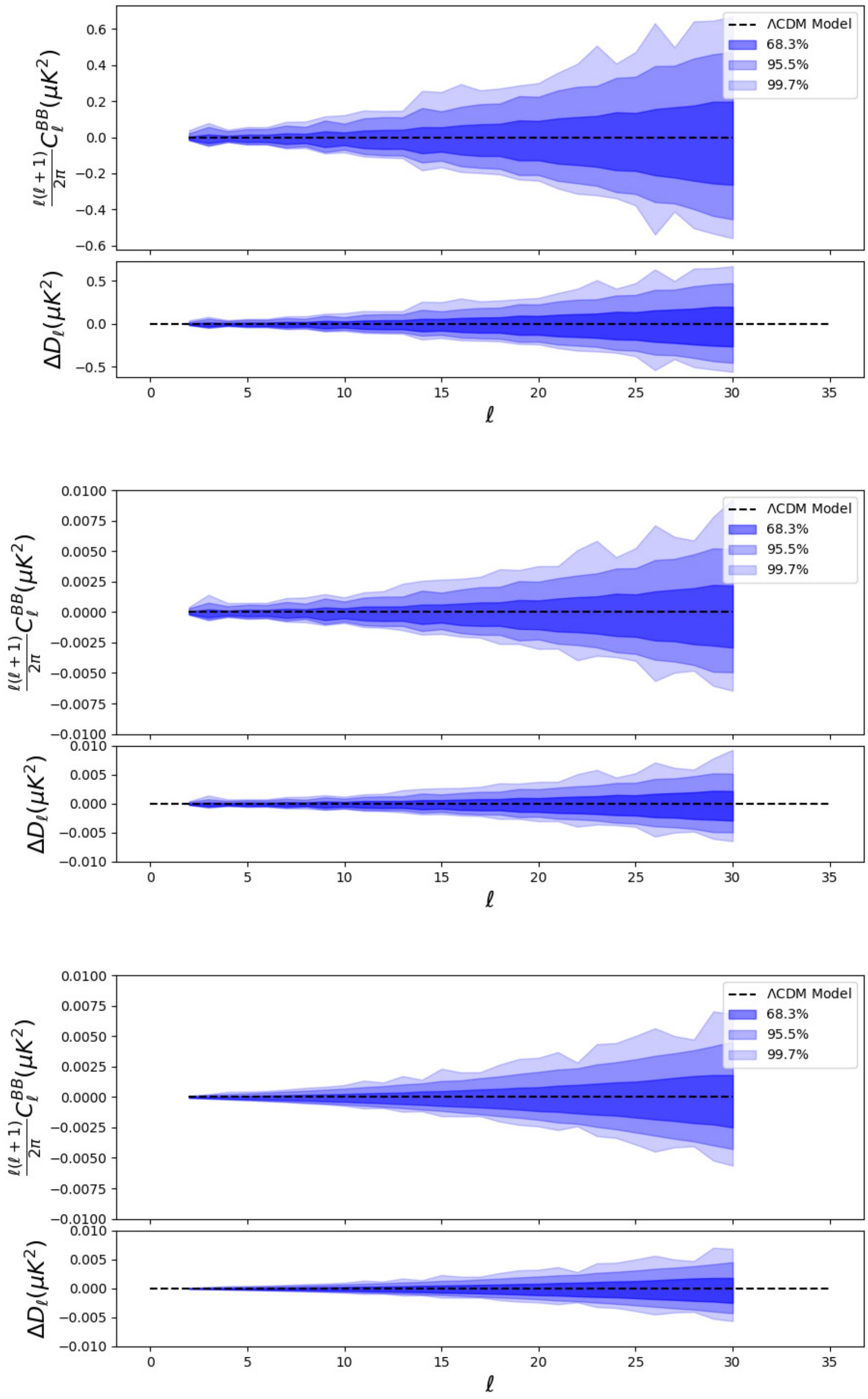

Figure 7.7: As Fig. 7.5, but for D_ℓ^{BB}. Note that the y-axes scale of the upper panel is different from the ones of the other panels. The confidence regions of LiteBird-Like and Ideal observations are narrower than the ones of Planck case by about a factor of 100.

We get the same behavior considering the APS of Random Variables.This is shown in Fig. 7.8 and Fig. 7.9 which display the Planck (upper panel), LiteBird-Like (middle panel) and Ideal (lower panel) cases of x_ℓ^2 and x_ℓ^3 respectively.

7.3 Forecasts for the Proposed Estimators

In this section we provide forecasts of the proposed estimators with respect to LiteBird-Like and Ideal CMB observations.

7.3.1 Forecasts for the 2D-variance

Fig. 7.10 displays the 2D-variance (defined in section 6.1) at $\ell_{max} = 30$ computed for Planck (upper panel), LiteBird-Like (middle panel) and Ideal (lower panel) observations. As expected, the C.L. for the LiteBird-Like and Ideal cases are narrower than the one for the Planck observations. In order to evaluate quantitatively the improvement of this 2D-estimator we compute for these three cases the area within the contour level at 68.3% in the space (var^{TT}, var^{QQ}) and then estimated the ratio between them. Fig. 7.11 shows the ratio between the areas at 68.3% level for Planck-Like (A_1) and for LiteBird-Like (A_2) observations as a function of ℓ. One can note that the improvement increases with the multipole, achieving the factor of ~ 2.6 at $\ell_{max} = 30$. The ratio between Planck and Ideal observations is basically the same as the one presented in Fig. 7.11: the ratio between LiteBird-Like and Ideal cases is almost constant with a value of 1, which means that using this estimator, also in ideal case, we can gain an improvement of ~ 2.6 at $\ell_{max} = 30$.

In the 2D-variance plot we do not see a large improvement from the forecast because the variance estimators depend on the lowest multipoles and not much on the ℓ in range where most of improvement from the forecast is present.

7.3.2 Forecasts for Dimensionless Normalised Mean Power

The Dimensionless Normalised Mean Power P (defined in section 6.2) is instead more sensitive to the decrease of the noise with respect to the variance estimators. Fig. 7.12 shows the distributions of the P estimator at $\ell_{max} = 30$ computed for Planck (upper panel), LiteBird-Like (middle panel) and Ideal (lower panel) observations. As expected, we gain a statistical improvement for the LiteBird-Like (and Ideal) with respect to Planck observations, which

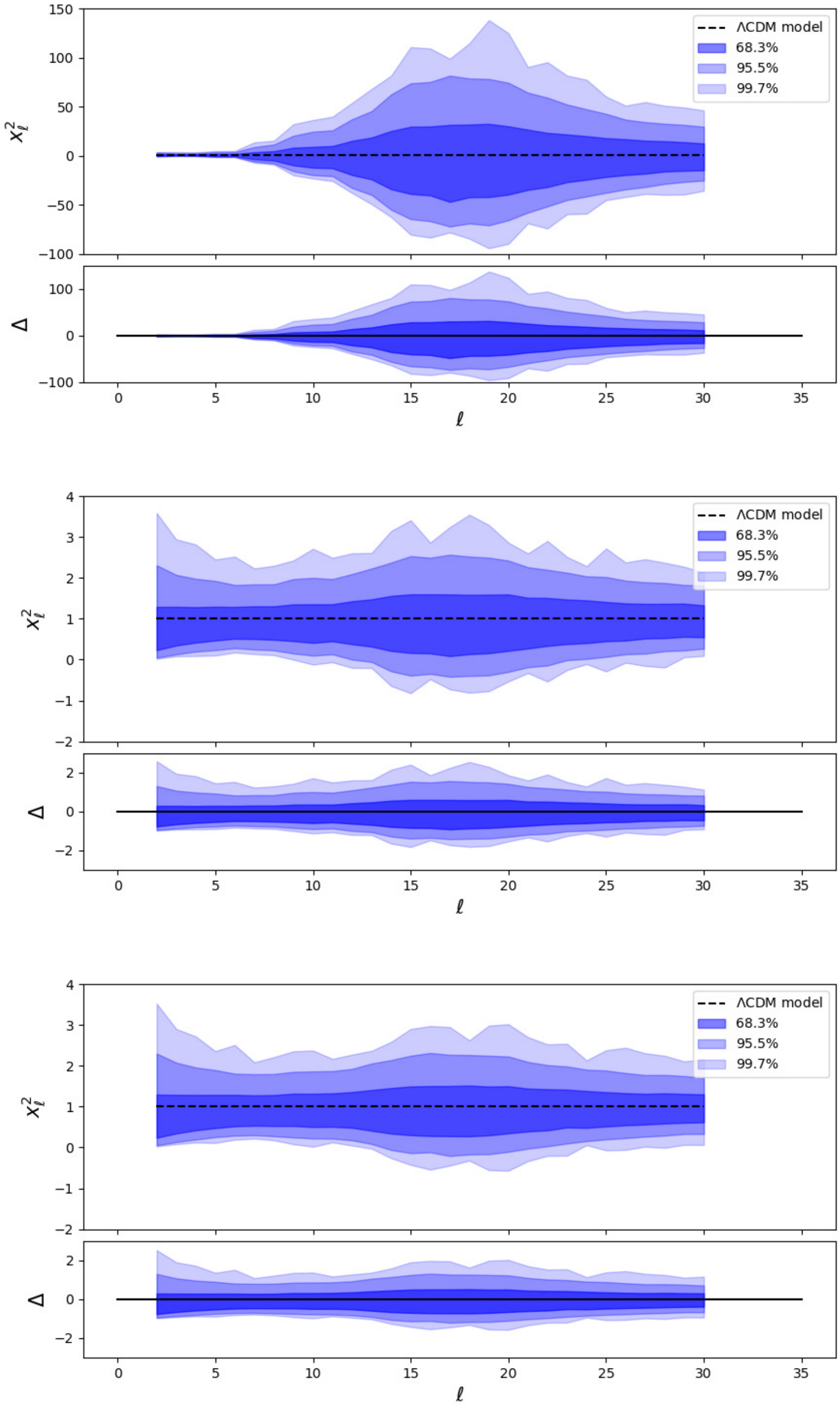

Figure 7.8: As Fig. 7.5, but for x_ℓ^2. Note that the y-axes scale of the upper panel is different from the ones of the other panels. The confidence regions of LiteBird-Like and Ideal observations are narrower than the ones of Planck case by about a factor of 50.

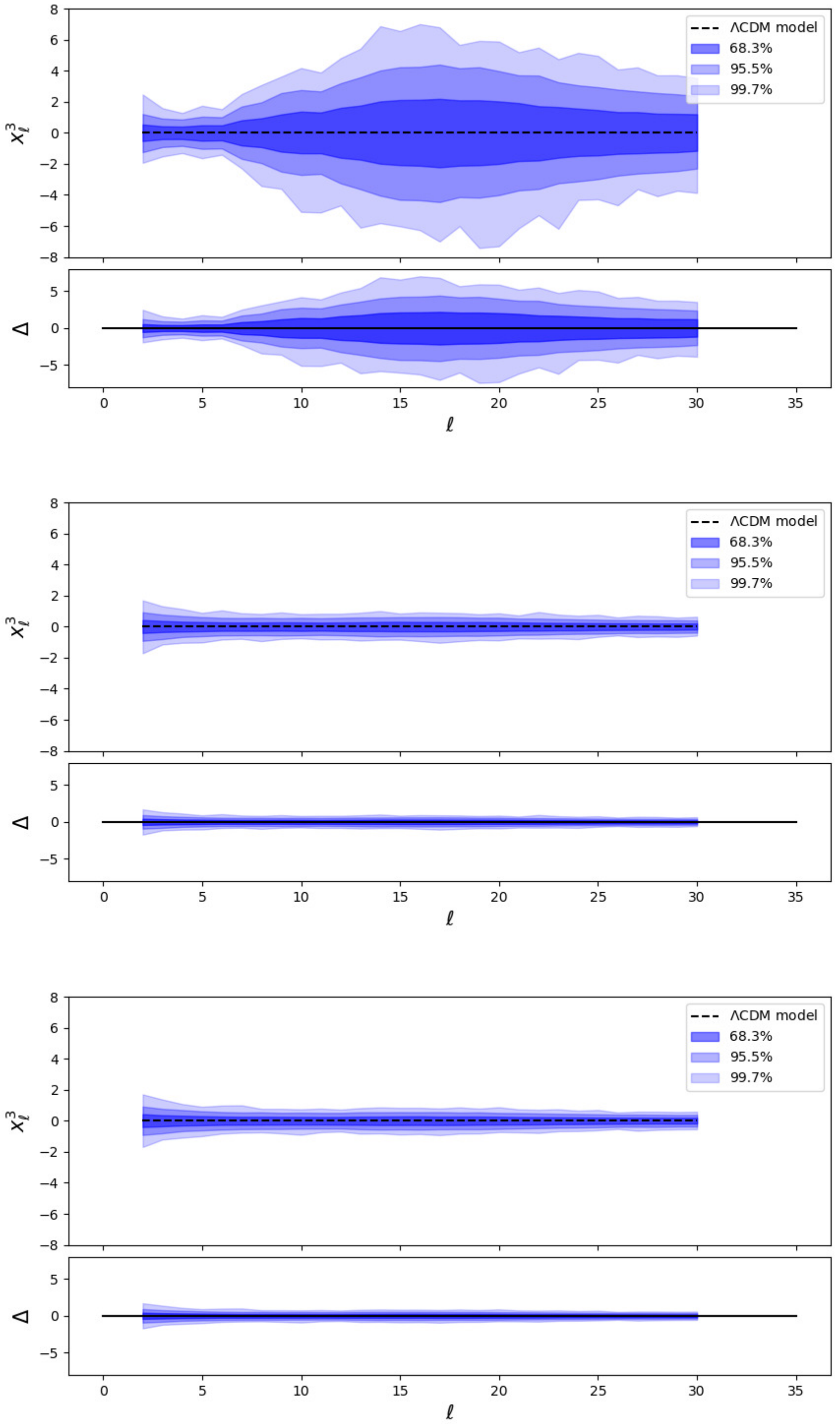

Figure 7.9: As Fig. 7.5, but for x_ℓ^3.

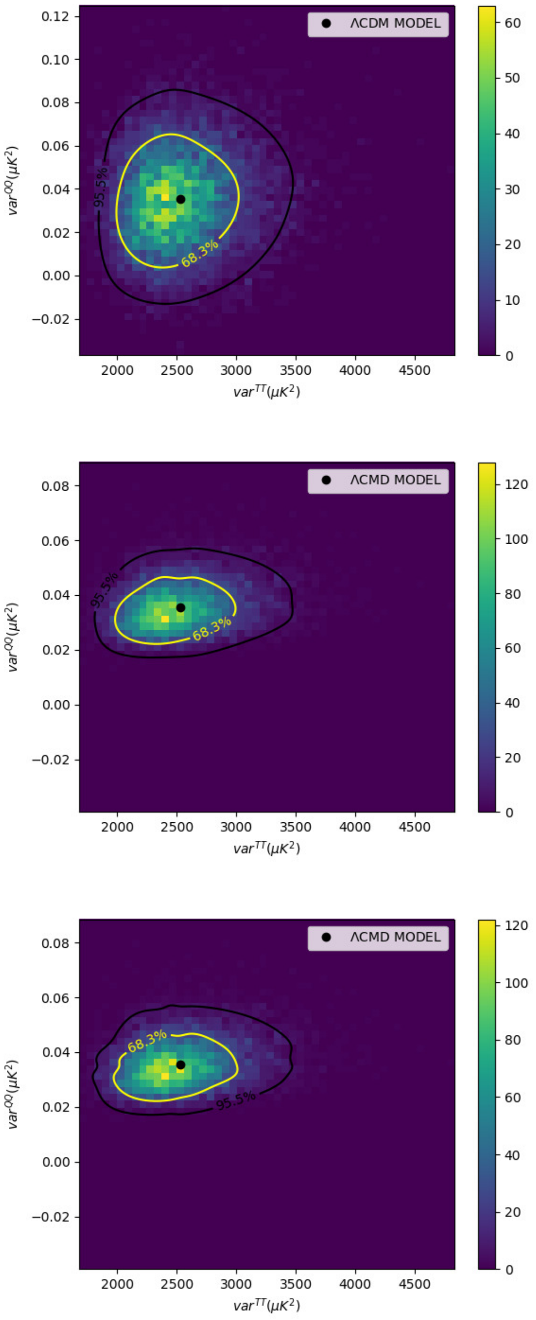

Figure 7.10: 3D-Histograms, encoded through the color map at the right, of the 2D variance for $\ell_{max} = 30$ for Planck (upper panel), LiteBird-Like (middle panel) and Ideal (lower panel) observations. The contours in the plane represent the 68.3% and 95, 5% regions. The black points are the values for the ΛCDM model. The C.L. of LiteBird-Like and Ideal observations are narrower than the ones of Planck case.

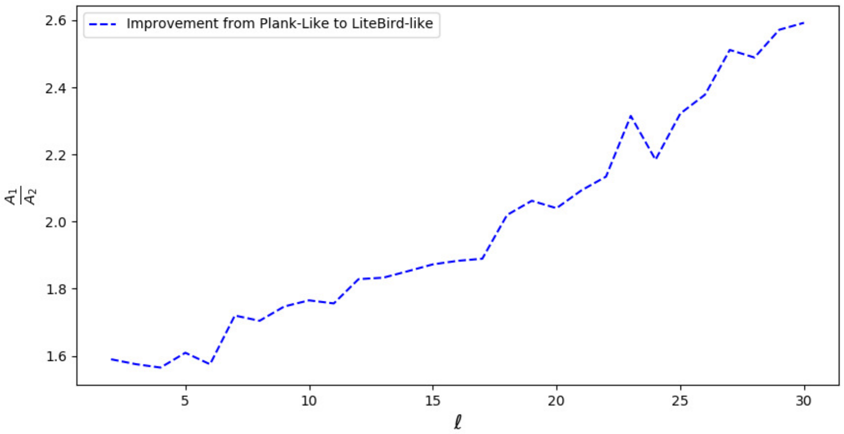

Figure 7.11: Ratio areas at 68.3% level for Planck (A_1) and for LiteBird-Like (A_2) observations as a function of ℓ: the improvement rises when increasing the multipole.

has been evaluated in terms of the ratio between the width (W) of the distributions corresponding to the 68.3% of probability. Fig 7.13 shows the ratio between the values of W: Planck to LiteBird-Like (upper panel), Planck to Ideal (middle panel) and LiteBird-Like to Ideal (lower panel). The panels show that the P estimator can be improved by a factor $\sim$ 30 already at $\ell_{max} = 20$. Moreover one can see that the LiteBird-Like observations are quite close to the limit of the Ideal case.

7.3.3 Forecasts for Optimised Dimensionless Normalised Mean Power

If we consider the estimator $\tilde{P}$ (defined in section 6.2.2) we can estimate its improvement in terms of the values of coefficients α and β. Fig. 7.14 shows α and β as a function of ℓ, for Planck-Like (upper panel), LiteBird-Like (middle panel) and Ideal (lower panel) observations. In the Planck case the coefficient β decreases rapidly to zero, because the main contribution to the variance comes from the polarisation part. In LiteBird-Like and Ideal cases instead α and β have similar values at very low multipoles, while at larger multipoles β decreases till the value of ~ 0.5 at $\ell_{max} = 30$, and α symmetrically increases reaching the value 1.5 at the same multipole $l_{max} = 30$.

This behavior is a direct consequence of the trend for S/N of the temperature and polarisation data. In short, future observations will allow to

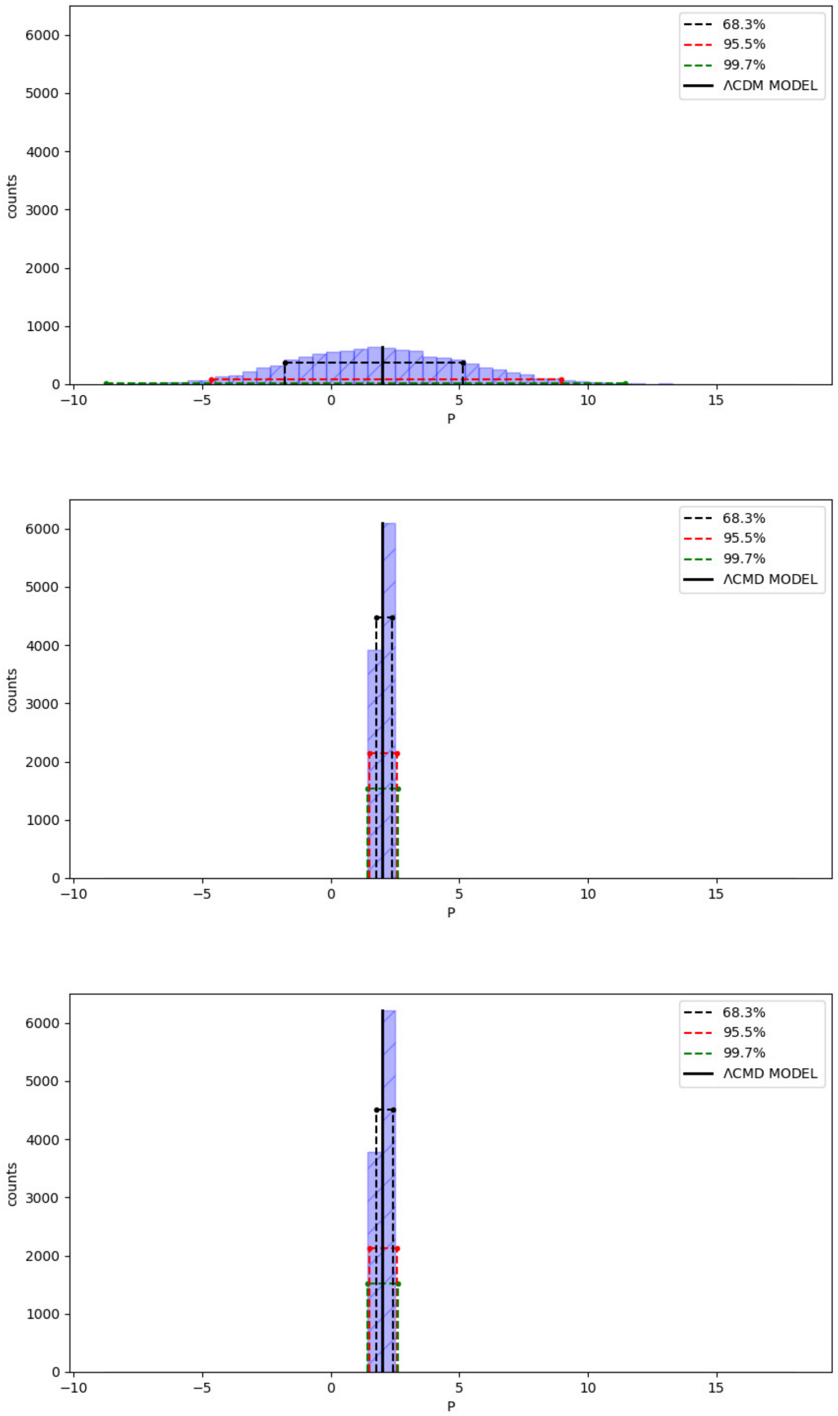

Figure 7.12: Empirical distributions of the P estimator for $\ell_{max} = 30$ for for Planck (upper panel), LiteBird-Like (middle panel) and Ideal (lower panel) observations. The black vertical line represents the values of the Planck data and of the ΛCDM model respectively. The blue, yellow and green lines indicate respectively the boundaries of the 68.3%, 95.5% and 99.7% confidence regions. The statistical improvement of the estimator gained for LiteBird-Like and Ideal observations is really significant.

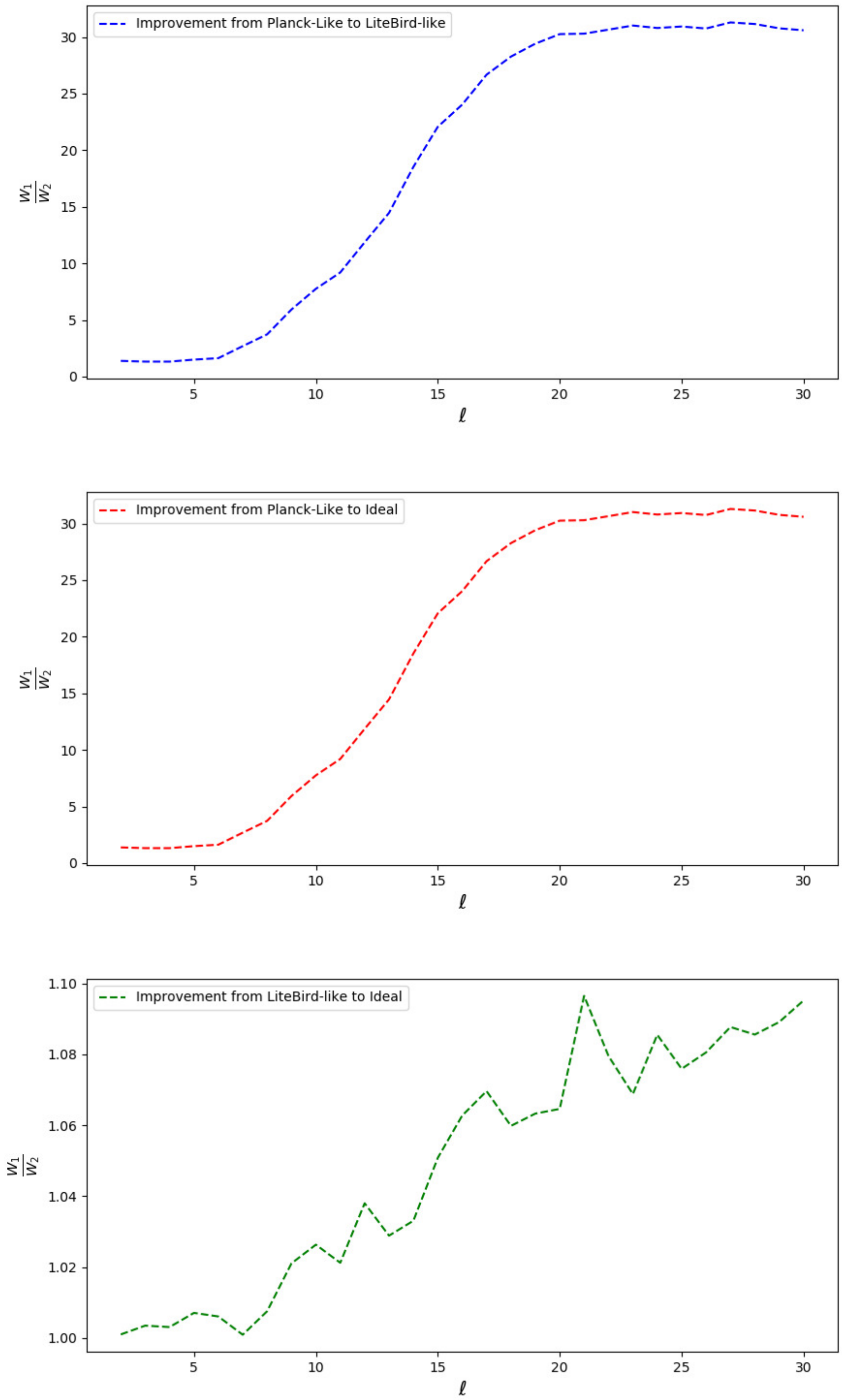

Figure 7.13: Ratio between the values of W: Planck to LiteBird-Like (upper panel), Planck-Like to Ideal (middle panel) and LiteBird-Like to Ideal (lower panel). The y-axes scale of the lower panel is different from the ones of the other panels. The estimator P can be improved by a factor ~ 30 already at $\ell_{max} = 20$ both for LiteBird-Like and Ideal Observation.

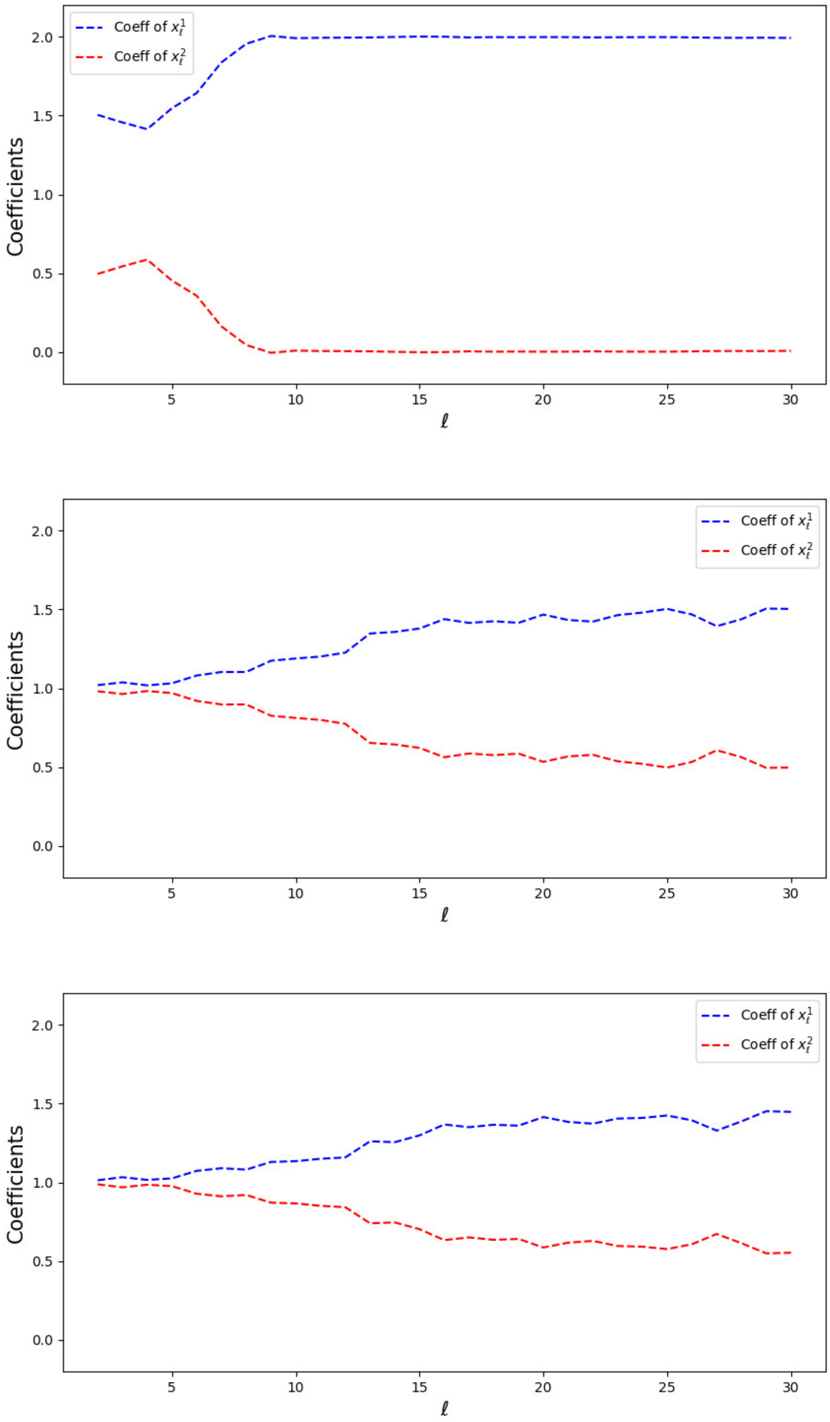

Figure 7.14: Comparison of the weight α and β in the $\tilde{P}$ estimator as a function of ℓ for Planck (upper panel), LiteBird-Like (middle panel) and Ideal (lower panel) observations. For Planck the coefficient β decreases rapidly to zero, instead in LiteBird-Like and Ideal observations β decreases only to the value of ~ 0.5

consider, for this joint estimator, about 1/4 of the information coming from the polarisation part.

Chapter 8

Conclusions

I have studied how to analise the power deficit anomaly present at large angular scale of the CMB anisotropies pattern considering both temperature and polarisation data. The main outcomes of my thesis are reported below.

- Using a two-dimensional estimator based on the variances, the probability to obtain a CMB realisation, which is smaller or equal to what observed in Planck data, turns out be $\sim 2\%$ when temperature and polarisation are considered, and $\sim 12\%$ when only T is taken into account.

- A similar behavior has been found considering the P estimator, defined in eq. (4.27). This one-dimensional estimator, which is the main element of novelty of the thesis, provides a lower tail probability of $\sim 3.6\%$ when temperature and polarisation are taken into account jointly and 17.6% when only T is considered.

Even if the new estimators increase the statistical significance, the lack of power cannot be still considered completely anomalous. This analysis is limited by the fact that the instrumental noise in polarisation is much larger than the signal and this reduces the number of multipoles that can be taken into account in the analysis.

This is not the case for future large scale polarisation observations:

- Forecast with LiteBird-like level of noise (or ideal observation) shows that the 2D variance can be improved by a factor of ~ 2.6.

- Forecast with the one-dimensional P estimator provides a much large improvement by a factor of ~ 30.

Therefore the inclusion of the large-scale E-mode polarisation can be foundamental in transforming this anomaly in a detection of a physical phenomenon beyond the standard ΛCDM cosmological model.

Bibliography

[1] R. Adam *et al.* [Planck Collaboration], Astron. Astrophys. **594** (2016) A1 doi:10.1051/0004-6361/201527101 [arXiv:1502.01582 [astro-ph.CO]].

[2] P. A. R. Ade *et al.* [Planck Collaboration], Astron. Astrophys. **571** (2014) A1 doi:10.1051/0004-6361/201321529 [arXiv:1303.5062 [astro-ph.CO]].

[3] P. A. R. Ade *et al.* [Planck Collaboration], Astron. Astrophys. **571** (2014) A16 doi:10.1051/0004-6361/201321591 [arXiv:1303.5076 [astro-ph.CO]].

[4] P. A. R. Ade *et al.* [Planck Collaboration], Astron. Astrophys. **571** (2014) A23 doi:10.1051/0004-6361/201321534 [arXiv:1303.5083 [astro-ph.CO]].

[5] P. A. R. Ade *et al.* [Planck Collaboration], Astron. Astrophys. **594** (2016) A13 doi:10.1051/0004-6361/201525830 [arXiv:1502.01589 [astro-ph.CO]].

[6] P. A. R. Ade *et al.* [Planck Collaboration], Astron. Astrophys. **594** (2016) A16 [arXiv:1506.07135 [astro-ph.CO]].

[7] P. A. R. Ade *et al.* [Planck Collaboration], Astron. Astrophys. **594** (2016) A17 doi:10.1051/0004-6361/201525836 [arXiv:1502.01592 [astro-ph.CO]].

[8] P. A. R. Ade *et al.* [Planck Collaboration], Astron. Astrophys. **571** (2014) A19 doi:10.1051/0004-6361/201321526 [arXiv:1303.5079 [astro-ph.CO]],

[9] P. A. R. Ade *et al.* [Planck Collaboration], Astron. Astrophys. **594** (2016) A20 doi:10.1051/0004-6361/201525898 [arXiv:1502.02114 [astro-ph.CO]].

[10] N. Aghanim *et al.* [Planck Collaboration], Astron. Astrophys. **594** (2016) A11 doi:10.1051/0004-6361/201526926 [arXiv:1507.02704 [astro-ph.CO]].

[11] N. Bartolo, E. Komatsu, S. Matarrese and A. Riotto, Phys. Rept. **402** (2004) 103 doi:10.1016/j.physrep.2004.08.022 [astro-ph/0406398].

[12] C. L. Bennett *et al.* [WMAP Collaboration], Astrophys. J. Suppl. **148** (2003) 1 doi:10.1086/377253 [astro-ph/0302207].

[13] S. Chandrasekhar, Radiative Transfer, (Dover, New York, 1960).

[14] P. Coles and. F. Lucchin, Cosmology, The origin and Evolution of Cosmic Structure, (John Wiley & Sons, Chichester, 1995).

[15] C. R. Contaldi, M. Peloso, L. Kofman and A. D. Linde, JCAP **0307** (2003) 002 doi:10.1088/1475-7516/2003/07/002 [astro-ph/0303636].

[16] D. Contreras, J. P. Zibin, D. Scott, A. J. Banday and K. M. Gorski, Phys. Rev. D **96** (2017) no.12, 123522 doi:10.1103/PhysRevD.96.123522 [arXiv:1704.03143 [astro-ph.CO]].

[17] C. Copi, D. Huterer, D. Schwarz and G. Starkman, Phys. Rev. D **75** (2007) 023507 doi:10.1103/PhysRevD.75.023507 [astro-ph/0605135].

[18] M. Cruz, P. Vielva, E. Martinez-Gonzalez and R. B. Barreiro, Mon. Not. Roy. Astron. Soc. **412** (2011) 2383 [arXiv:1005.1264 [astro-ph.CO]].

27

[19] R. H. Dicke, P. J. E. Peebles, P.G.Roll, D.T. Wilkinson, 1965,

[20] H. K. Eriksen, F. K. Hansen, A. J. Banday, K. M. Gorski and P. B. Lilje, Astrophys. J. **605** (2004) 14 Erratum: [Astrophys. J. **609** (2004) 1198] doi:10.1086/382267 [astro-ph/0307507].

[21] C. Gibelyou, D. Huterer and W. Fang, Phys. Rev. D **82** (2010) 123009 doi:10.1103/PhysRevD.82.123009 [arXiv:1007.0757 [astro-ph.CO]].

[22] K. M. Gorski, E. Hivon, A. J. Banday, B. D. Wandelt, F. K. Hansen, M. Reinecke and M. Bartelman, Astrophys. J. **622** (2005) 759 doi:10.1086/427976 [astro-ph/0409513]. http://sourceforge.net/projects/healpix/.

42+2

[23] A. Gruppuso, A. De Rosa, P. Cabella, F. Paci, F. Finelli, P. Natoli, G. de Gasperis and N. Mandolesi, Mon. Not. Roy. Astron. Soc. **400** (2009) 463 doi:10.1111/j.1365-2966.2009.15469.x [arXiv:0904.0789 [astro-ph.CO]].

[24] A. Gruppuso, N. Kitazawa, M. Lattanzi, N. Mandolesi, P. Natoli and A. Sagnotti, Phys. Dark Univ. **20** (2018) 49 doi:10.1016/j.dark.2018.03.002 [arXiv:1712.03288 [astro-ph.CO]].

[25] A. Gruppuso, N. Kitazawa, N. Mandolesi, P. Natoli and A. Sagnotti, Phys. Dark Univ. **11** (2016) 68 [arXiv:1508.00411 [astro-ph.CO]].

[26] A. Gruppuso, Mon. Not. Roy. Astron. Soc. **437** (2014) no.3, 2076 doi:10.1093/mnras/stt1937 [arXiv:1310.2822 [astro-ph.CO]].

[27] A. Gruppuso, P. Natoli, F. Paci, F. Finelli, D. Molinari, A. De Rosa and N. Mandolesi, JCAP **1307** (2013) 047 [arXiv:1304.5493 [astro-ph.CO]].

[28] A. Gruppuso and A. Sagnotti, Int. J. Mod. Phys. **D 24** (2015) no.12, 1544008 [arXiv:1506.08093 [astro-ph.CO]].

[29] G. Hinshaw, A. J. Banday, C. L. Bennett, K. M. Gorski, A. Kogut, C. H. Lineweaver, G. F. Smoot and E. L. Wright, Astrophys. J. **464** (1996) L25 doi:10.1086/310076 [astro-ph/9601061].

[30] W. Hu and M. J. White, New Astron. **2**, 323 (1997) doi:10.1016/S1384-1076(97)00022-5 [astro-ph/9706147].

[31] K. Land and J. Magueijo, Phys. Rev. D **72** (2005) 101302 doi:10.1103/PhysRevD.72.101302 [astro-ph/0507289].

[32] M. Lattanzi *et al.*, JCAP **1702** (2017) no.02, 041 doi:10.1088/1475-7516/2017/02/041, 10.1088/1475- [arXiv:1611.01123 [astro-ph.CO]].

[33] A. Lewis, JCAP **1206** (2012) 023 doi:10.1088/1475-7516/2012/06/023 [arXiv:1204.5018 [astro-ph.CO]].

[34] J. C. Mather et al. 1994, apj, 420, 439

[35] C. Monteserin, R. B. B. Barreiro, P. Vielva, E. Martinez-Gonzalez, M. P. Hobson and A. N. Lasenby, Mon. Not. Roy. Astron. Soc. **387** (2008) 209 [arXiv:0706.4289 [astro-ph]].

[36] V. F. Mukhanov, Physical Foundations of Cosmology (Cambridge University Press, Cambridge, 2005)

[37] Nielsen, F. 2013, arXiv:1301.3578

[38] P. Ntelis *et al.*, JCAP **1706** (2017) no.06, 019 doi:10.1088/1475-7516/2017/06/019 [arXiv:1702.02159 [astro-ph.CO]].

[39] A. de Oliveira-Costa, M. Tegmark, M. Zaldarriaga and A. Hamilton, Phys. Rev. D **69** (2004) 063516 doi:10.1103/PhysRevD.69.063516 [astro-ph/0307282].

[40] A. A. Penzias and R. W. Wilson, Astrophys. J. **142** (1965) 419. doi:10.1086/148307

[41] A. Riotto, ICTP Lect. Notes Ser. **14** (2003) 317 [hep-ph/0210162].

[42] R. K. Sachs, A. M. Wolfe, 1967, apj, 147, 73

[43] D. J. Schwarz, C. J. Copi, D. Huterer and G. D. Starkman, Class. Quant. Grav. **33** (2016) no.18, 184001 doi:10.1088/0264-9381/33/18/184001 [arXiv:1510.07929 [astro-ph.CO]].

[44] G. F. Smoot, AIP Conf. Proc. **476** (1999) no.1, 1 doi:10.1063/1.59326 [astro-ph/9902027].

[45] G.F. Smoot, C. L. Bennett, A. Kogut, et al. 1992,apj, 396, L1

[46] R. A. Sunyaev, and Y. B. Zeldovich, 1970, Comments on Astrophysics and Space Physics, 2, 66

[47] A. Suzuki *et al.*, arXiv:1801.06987 [astro-ph.IM].

[48] M. Tegmark, Phys. Rev. D **55** (1997) 5895 doi:10.1103/PhysRevD.55.5895 [astro-ph/9611174].

[49] M. Tegmark and A. de Oliveira-Costa, Phys. Rev. D **64** (2001) 063001 doi:10.1103/PhysRevD.64.063001 [astro-ph/0012120].

[50] P. Vielva, E. Martinez-Gonzalez, R. B. Barreiro, J. L. Sanz and L. Cayon, Astrophys. J. **609** (2004) 22 doi:10.1086/421007 [astro-ph/0310273].

[51] S. Weinberg, Cosmology (Oxford University Press, Oxford, 2008)

[52] A. Yoho, C. J. Copi, G. D. Starkman and A. Kosowsky, Mon. Not. Roy. Astron. Soc. **442** (2014) no.3, 2392 doi:10.1093/mnras/stu942 [arXiv:1310.7603 [astro-ph.CO]].

[53] M. Zaldarriaga and U. Seljak, Phys. Rev. D **55** (1997) 1830 doi:10.1103/PhysRevD.55.1830 [astro-ph/9609170].

Ringraziamenti

Vorrei ringraziare innanzitutto il mio relatore prof. Lauro Moscardini e i miei co-relatori dott. Alessandro Gruppuso e prof. Reno Mandolesi, per la grande disponibilità dimostrata nei miei confronti. In secondo luogo la mia famiglia, e in particolare i miei genitori, Luciano e Nadia, per avermi sostenuto, incoraggiato e creduto in me. Un ringraziamento speciale a Valentina che mi sopporta sempre e mi regala il suo amore ogni giorno. Infine, last but not least, un grazie agli amici di una vita con cui ho passato momenti indimenticabili.